Université Libre de Bruxelles
Faculté des Sciences

Contribution to the $\nu_\mu \rightarrow \nu_\tau$ oscillation search in the CHORUS experiment

Dissertation présentée par
Muriel Vander Donckt
en vue de l'obtention du grade
de Docteur en Sciences.
Promoteur: Pr. P. Vilain
Janvier 1999

Acknowledgments - Remerciements.

Je voudrais tout d'abord remercier le professeur Jean Sacton pour m'avoir accueillie dans son laboratoire et dirigée vers l'expérience CHORUS.

Je voudrais ensuite exprimer toute ma gratitude aux professeurs Pierre Vilain et Gaston Wilquet, dont les compétences, le soutien et l'amitié m'ont permis de mener à bien ce travail.

I am also indebted to the whole CHORUS team, among which its succesive spokesmen, Klaus Winter and Paolo Strolin, and contactperson Jaap Panman for introducing me to the experimental work and welcoming me within the collaboration. Within the team working at CERN, I would specially like to thank all those whose welcoming behaviour transformed into a lasting friendship : Maarten, Erhan, Fabio, Jürgen, Rui, Joelle, Gus and later - in time only - David, Aimo, Oliver, Franca, Rolf...

A special thanks to Professor K. Niwa for welcoming me, not only in his laboratory, but also into his house and family, and introducing me to emulsion scanning and many aspects of Japanese culture. I take this opportunity to thank also, all the Nagoya group members who helped during my stay, Professor H. Shibuya for his invitation to the Toho laboratory and his students for looking after me greately during my stay there.

I would also like to thank the members of the Brussels IIHE staff and the students for interesting and relaxing, userfriendly, enjoyable atmosphere in- and outside working hours. Merci à/Bedankt aan Monique, Pascal V., Othmane, Ann, Véronique, Jacqueline, Ruru, An, Barbara, Laurent, Yves, les 2 Catherine, Walter, Guy,... et la liste n'est pas exhaustive.

Je dois aussi des remerciements au professeur Jean-Marie Frère, pour son aide concernant le chapitre théorique de cette thèse ainsi que pour m'avoir offert de travailler dans son service et d'y terminer la rédaction de ce travail, et à Karin dont j'ai grand plaisir à partager le bureau.

Et je ne voudrais certainement pas oublier ni ma famille (dont Françoise et Lara) dont l'impatience m' a aidée à terminer la rédaction de ce travail, ni les nombreuses personnes qui m'ont soutenue par leur amitié tout au long de cette thèse et sans qui la vie perdrait beaucoup de sa saveur: Marc, Patrick, Pascal W., Kathy, Emmanuèle, Sandy, Biv, Wim, Sudeshna, Alex,...

Je me dois enfin de remercier les organismes suivants pour leur soutien financier: l'I.R.S.I.A., le F.R.I.A., et le Fonds D. et A. Vanbuuren.

Table of contents

Introduction

Neutrinos have been an ever growing centre of interest ever since their "invention" in 1932 by W. Pauli, to explain the continuous energy spectrum of the electrons in β decay.

In the Standard Model of electroweak interactions, they are considered to be massless. However, chapter I describes how massive neutrinos can arise naturally in the theory. If neutrinos are massive, several phenomena can occur such as a mixing between the different mass and flavour eigenstates, as it has already been observed in the quark sector. A neutrino created in a particular flavour eigenstate, could transform into another one while it propagates.

There are numerous hints that neutrinos should be massive, coming from theory, cosmology or experimental results. Indeed, many experiments have set out to look for direct neutrino mass and oscillations, which would be the direct consequence of the presence of a mass hierarchy and mixing. They are described in chapter II.

A neutrino mass of the order of a few eV/c^2 was favoured by hot dark matter cosmological models. The neutrinos are often expected to reproduce the same mass hierarchy as their charged partners or quark families, such that the ν_τ would be the heaviest: the most interesting candidate for hot dark matter. The best way to produce large quantities of neutrinos are accelerators which produce beams mainly composed of muon neutrinos or anti-neutrinos. Experiments had already excluded this interesting mass domain down to mixing angles between ν_μ and ν_τ of $\sin^2(2\theta) = 5 \ \ 10^{-3}$ [II.46]. There was a need of a new experiment, which could accumulate enough statistics with a low background to explore the very low $\sin^2(2\theta)$ region, down to about $2 \ \ 10^{-4}$.

The CHORUS detector described in chapter III was designed to cover that region of parameters: is a background-free, high statistics experiment searching for $\nu_\mu \rightarrow \nu_\tau$ oscillations. It was exposed during 4 years to the ν_μ beam produced at the SPS Wide Band Beam facility at CERN, Geneva. The average energy of the beam of 26 GeV and the location of the detector at 600 m from the neutrino source, allow to reach the cosmologically interesting mass region. The main feature of the CHORUS experiment is to insure the high rejection level of background thanks to its 1μm spatial resolution nuclear emulsion target, allowing the direct detection of the decay of the τ^- created in a ν_τ charged current interaction. Indeed, due to its very short (10^{-13} s) lifetime, the τ^- lepton only leaves a track of the order of a mm.

The electronic detector downstream of the target allows to predict the events positions in the emulsion and to discriminate between signal and background sources. One of the key ingredients in this discrimination is the hadron spectrometer, the task of which is to determine the charge of the particles coming from a neutrino interaction. The scintillating

fibre tracking system used both for the hadron spectrometer and the prediction of events in the emulsion is described in chapter IV, the track finding and momentum determination procedures are described in chapter V.

The achieved momentum resolution allows to determine the sensitivity of the CHORUS experiment in terms of $\nu_\mu \rightarrow \nu_\tau$ oscillations, as well as the background contamination it could suffer from. This analysis is described in chapter VI, where an upper limit on the oscillation probability is set using the data sample scanned in the emulsion up to July 1998.

Chapter I Theoretical background.

This chapter introduces the neutrinos as they are described in the Standard Model of electroweak interactions (SM), and some of the phenomena to which a non vanishing neutrino mass can lead [I.1].

A The standard model.

The Standard Model of electroweak interactions rests on a gauge theory: the main forces arise from symmetry principles. The forces are mediated by vector (spin 1) gauge bosons. The relevant symmetry group in the electroweak model is the SU(2)×U(1) group. The electroweak model is divided into three sectors:

- The gauge sector contains the 4 gauge bosons: the two charged $W^{\pm}$ mediate the charged current interactions while Z^0 and γ are responsible for the neutral current interactions,
- the fermion sector is organised in three families of left-handed doublets and right-handed singlets under SU(2) as shown below :
  the quarks :

$$\begin{pmatrix} d \\ u \end{pmatrix}_L \; d_R \qquad \begin{pmatrix} s \\ c \end{pmatrix}_L \; s_R \qquad \begin{pmatrix} b \\ t \end{pmatrix}_L \; b_R$$

  and the leptons:

$$\begin{pmatrix} e^- \\ \nu_e \end{pmatrix}_L \; e^-_R \qquad \begin{pmatrix} \mu^- \\ \nu_\mu \end{pmatrix}_L \; \mu^-_R \qquad \begin{pmatrix} \tau^- \\ \nu_\tau \end{pmatrix}_L \; \tau^-_R$$

  where L denotes left-handed SU(2) doublets and R right-handed SU(2) singlets. To each particle corresponds an antiparticle, with the same mass and opposite quantum numbers.
- the Higgs sector was introduced to give mass to the otherwise massless fermions and gauge bosons: a complex scalar (spin 0) doublet is introduced. New parameters enter the model in the shape of a Higgs potential and couplings of the Higgs to the fermions and the gauge bosons. The Higgs doublet acquires a non-zero vacuum expectation value which breaks the SU(2) symmetry spontaneously. After symmetry breaking, it gives rise to the masses of the bosons and fermions and leaves one new particle yet to be discovered: the Higgs boson.

In the quark sector, the fields entering the weak charged current are now expressed as a mixed form of the mass eigenstates. The mass eigenstates and the weak eigenstates are

related via a unitary matrix called the Cabibbo-Kobayashi-Maskawa matrix [I.2].

There exists no such mixing in the leptonic sector as the neutrinos are massless and thus degenerate. Indeed, the minimal version of the Standard Model does not contain right-handed neutrinos such that the neutrinos do not couple to the SM Higgs doublet. As shown below, some extensions of this model allow neutrinos to acquire mass without introducing right-handed neutrinos. However, these extensions require the addition of a complex scalar Higgs triplet.

B Number of fermion families.

The Standard Model does not predict the number of families of fermions. Experimental results can constrain within the framework of the SM the number of neutrinos coupling to the Z^0. The existence of a fourth neutrino would give strong hints for the existence of a complete fourth generation of fermions. Standard Model parameters are fitted to the data of the four LEP experiments, such as the Z^0 total width $?_Z$, and its partial widths into charged leptons $?_{ee}, ?_{\mu\mu}$ and $?_{\tau\tau}$ (or $?_{ll}$ assuming lepton universality) and into hadrons $?_{had}$. The number of light ($m_\nu < \frac{m_Z}{2}$) neutrino species N_ν is given by

$$N_\nu = \frac{\Gamma_{inv}}{\Gamma_{ll}} / (\frac{\Gamma_{\nu\nu}}{\Gamma_{ll}})_{SM} = \frac{5.960 \pm 0.022}{1.991 \pm 0.001} = 2.993 \pm 0.011 \text{ [I.3]}$$

Where $?_{inv} = ?_Z - ?_{ee} - ?_{\mu\mu} - ?_{\tau\tau} - ?_{had}$ is the invisible decay width of the Z^0 and $(\frac{\Gamma_{\nu\nu}}{\Gamma_{ll}})_{SM}$ is the ratio of the partial widths of the Z^0 into neutrinos and charged leptons predicted by the Standard Model.[I.3]

This measurement is compatible with the less stringent bounds coming from primordial nucleosynthesis and the observed ^{4}He abundances in various objects of our universe.

C The discovery of the neutrinos.

1 First observation.

The "neutrino" postulated by Pauli in the 30's to explain the continuous β-decay spectrum of nuclei and restore energy-momentum conservation in these decays was discovered by Reines and Cowan in 1956 [I.4]. Their experiment was located near the Savannah River nuclear power plant. The setup consisted of a solution of cadmium chloride as target sandwiched with scintillation counters. The "neutrinos" arising from nuclear fission and fragment decay in the nuclear reactor interacted with a proton of the target producing an e^+ and a neutron. The positron was detected via the gamma emission following its annihilation with an electron and after some flight length, the neutron was absorbed by a Cd nucleus, followed by gamma emission. The energy and time-delayed coincidence of the two gamma pulses allowed to identify neutrino events.

2 Distinction between neutrino and antineutrino

If the neutrino (ν) produced with an e^+ is identical to the "neutrino" (ν') produced with an e^- , then the ^{37}Cl $+\nu' \rightarrow$ ^{37}Ar $+e^-$ reaction should occur near nuclear reactors as the

capture reaction $^{37}\mathrm{Ar} + \mathrm{e}^- \rightarrow {}^{37}\mathrm{Cl} + \nu$ is well known to occur. R. Davis investigated this first reaction with a negative result and gave an upper limit on the reaction cross section [I.5]. The particle producing e^- in charged currents will from here on be called the neutrino (ν), the one producing e^+ and discovered by Reines and Cowan, the antineutrino ($\bar{\nu}$).

3 The difference between ν_μ and ν_e .

The absence in nature of processes of the type $\mu^- + \mathrm{p} \rightarrow \mathrm{e}^- + \mathrm{p}$ or $\mu^- \rightarrow \mathrm{e}^- + \gamma$ points to the existence of different types of neutrinos. In 1962, the interactions of neutrinos produced in $\pi^\pm \rightarrow \mu^\pm + \nu/\bar{\nu}$ decays were observed in a spark chamber of an experiment [I.6] at Brookhaven AGS*. They compared the number of long single (muon) track and short (electron) shower events and found an excess of muon events with respect to the number of electron events one would have expected if the neutrino produced in β-decay were the same as the neutrino produced in π decays. They concluded to the existence of two kinds of neutrinos, the type produced with e^+ is called ν_e , the type produced with μ^+ , ν_μ .

4 Indirect evidence of the existence of the ν_τ .

Direct identification of the ν_τ by its production via charged current of a τ^- lepton has not yet been done. The E872 experiment at Fermilab has exposed a nuclear emulsion target to a high energy neutrino flux expected to contain 5-10% ν_τ . The tau neutrinos are produced via the production and decay of D_s mesons into $\tau\nu_\tau$ followed by the decay of the τ. The interaction of the 800GeV proton beam on a tungsten dump yields a significant fraction of D_s mesons. A detailed calculation of the expected ν_τ interaction rate in the E872 target can be found in [I.7]. The analysis of the collected data sample is currently going on and no result has been published, yet.

Indirect evidence for the existence of the ν_τ neutrino forming a SU(2) doublet with the τ already exists:

- The well measured coupling of the τ_L to the W requires the τ_L to be a member of a SU(2) doublet.
- The number of light neutrinos coupling to the Z^0 is measured at LEP to be 3 (cf. section B).

If the ν_τ exists, it is different from the ν_e and ν_μ : the E531[II.46] experiment looking for ν_τ interactions in a beam of ν_e and ν_μ did not find any candidate. They put 90% C.L. upper limits on the direct coupling of these neutrinos to the τ lepton in terms of decay width of the $\tau^- \rightarrow l^- \bar{\nu}_l \nu_{e,\mu}$.

$$\begin{aligned} ?\,(\tau^- \rightarrow l^- \bar{\nu}_l \nu_\mu\ ) &< 8.3 \times 10^{-13}\ MeV \\ ?\,(\tau^- \rightarrow l^- \bar{\nu}_l \nu_\mathrm{e}\ ) &< 3.0 \times 10^{-11}\ MeV \end{aligned}$$

These upper limits have to be compared to the τ^- leptonic decay width:

$$?\,(\tau^- \rightarrow l^- \bar{\nu}_l \nu_\tau\ ) = 4.8 \times 10^{-10}\ MeV \text{[II.63]}$$

showing that the neutrino produced in the leptonic decays of the τ^- is predominantly different from ν_e and ν_μ .

*AGS stands for Alternate Gradient Synchrotron

D Weyl, Dirac and Majorana neutrinos.

In the minimal version of the Standard Model, neutrinos are massless and they are described by Weyl two components (left-handed neutrino and right-handed antineutrino) spinors. For a massless particle, the left-handed chiral field corresponds to a neutrino with negative helicity.
If neutrinos are massive, the left chirality field will describe a negative helicity state with an admixture (of order $\frac{m}{E}$) of the positive helicity state, such that neutrinos produced in a decay at rest will, in this frame, have mostly the negative helicity with a small admixture of positive helicity. Choosing a reference frame travelling in the direction of the neutrino but at higher speed than the particle, a dominance of the positive helicity will be observed.

In the specific case where a lepton number can be defined for massive neutrinos, they will be called "Dirac neutrinos", otherwise they are called "Majorana neutrinos".
A Dirac neutrino has four different possible states (left and right-handed neutrino and antineutrino states) and a Majorana neutrino only has two (left and right-handed states). In the case of the Majorana neutrino, a spin flip would change the sign of the charged lepton that would be produced in a charged current interaction. For Dirac neutrinos, the neutrino left-handed field produces the associated lepton and the antineutrino right-handed field the corresponding antilepton, the two other fields do not interact via charged current.
The spin flip experiment is not feasible in practice. Another way of settling this issue is to look for neutrinoless double β-decay of nuclei for which the single β-decay is forbidden as such a process is only possible for Majorana neutrinos (cf section II.C.1).

E Neutrino mass terms.

1 Dirac mass term.

For a Dirac spinor ν^D, the neutrino mass term in the Lagrangian for a single neutrino species can be written as:

$$L^{Dirac} = -m_D \left[\overline{(\nu_L^D)} \nu_R^D + \overline{(\nu_R^D)} \nu_L^D \right]$$

Where $\nu_L^D \equiv \frac{1-\gamma^5}{2}\nu^D$ and $\nu_R^D \equiv \frac{1+\gamma^5}{2}\nu^D$ are Weyl spinors of left and right chirality respectively. The 4×4 matrix γ^5 has eigen values $+1$ and -1, such that $\frac{1\pm\gamma^5}{2}$ are projection operators.

2 Majorana mass term.

For Majorana neutrinos, mass terms can be formed using a single Weyl spinor ν_L^M and its "charge conjugate" $(\nu_L^M)^c$.

$$L_L^{Majorana} = -\frac{m_L}{2} \left[\overline{(\nu_L^M)}^c \nu_L^M + \overline{(\nu_L^M)} (\nu_L^M)^c \right]$$
$$L_R^{Majorana} = -\frac{m_R}{2} \left[\overline{(\nu_R^M)}^c \nu_R^M + \overline{(\nu_R^M)} (\nu_R^M)^c \right]$$

3 General mass term.

A general mass term can be written by combining the Dirac and Majorana mass terms :

$$L^{mass} = -\tfrac{1}{2}\left[m_D\left(\overline{(\nu_R)}\nu_L + \overline{(\nu_L)}^c(\nu_R)^c\right) - m_L\overline{(\nu_L)}^c\nu_L - m_R\overline{(\nu_R)}(\nu_R)^c\right] + \text{h.c.}^\dagger$$

which can be rewritten as

$$L^{mass} = -\tfrac{1}{2}\overline{(n_L)}^c M n_L + h.c.$$

where :

$$n_L = \begin{pmatrix} \nu_L \\ (\nu_R)^c \end{pmatrix} \qquad and \qquad M = \begin{pmatrix} m_L & m_D \\ m_D & m_R \end{pmatrix}$$

The M matrix can be diagonalised to obtain the mass eigenstates and eigenvalues. Assuming CP invariance, the parameters m_D, m_R and m_L can be chosen real and M=$O^T\tilde{m}$O where O is an orthogonal matrix. The matrix O=$\begin{pmatrix} \cos\alpha & -\sin\alpha \\ \sin\alpha & \cos\alpha \end{pmatrix}$ needed to diagonalise a symmetric matrix A=$\begin{pmatrix} a & c \\ c & b \end{pmatrix}$ is such that $\tan 2\alpha = \frac{2c}{a-b}$. Here, $\tan 2\alpha = \frac{2m_D}{m_L - m_R}$ and $\tilde{m}$ is a diagonal matrix with eigenvalues :

$$\tilde{m}_{1,2} = \tfrac{1}{2}\left(m_L + m_R \mp \sqrt{(m_L - m_R)^2 + 4m_D^2}\right)$$

The eigenvalue $\tilde{m}_1$ is negative such that it cannot be interpreted as the mass of a physical field. We can rewrite $\tilde{m}$ as $\begin{pmatrix} -\tilde{m}_1 & 0 \\ 0 & \tilde{m}_2 \end{pmatrix}\begin{pmatrix} -1 & 0 \\ 0 & 1 \end{pmatrix} \equiv mK$, where K is the diagonal matrix with the signs, such that M=OmKO^T and $m_{1,2} = |\tilde{m}_{1,2}|$. If we define the column vectors:

$$\begin{pmatrix} \chi_{1L} \\ \chi_{2L} \end{pmatrix} \equiv O\begin{pmatrix} \nu_L \\ (\nu_R)^c \end{pmatrix} = \begin{pmatrix} \cos\alpha & -\sin\alpha \\ \sin\alpha & \cos\alpha \end{pmatrix}\begin{pmatrix} \nu_L \\ (\nu_R)^c \end{pmatrix} \tag{I.1}$$

$$\begin{pmatrix} \chi_{1R} \\ \chi_{2R} \end{pmatrix} \equiv KO\begin{pmatrix} (\nu_L)^c \\ \nu_R \end{pmatrix} = \begin{pmatrix} -\cos\alpha & \sin\alpha \\ \sin\alpha & \cos\alpha \end{pmatrix}\begin{pmatrix} (\nu_L)^c \\ \nu_R \end{pmatrix} \tag{I.2}$$

The mass term reduces to :

$$L^{mass} = -\tfrac{1}{2}\left(m_1\bar{\chi}_1\chi_1 + m_2\bar{\chi}_2\chi_2\right)$$

Where

$$\begin{aligned} \chi_1 = \chi_{1L} + \chi_{1R} &= \cos\alpha(\nu_L - (\nu_L)^c) + \sin\alpha(\nu_R - (\nu_R)^c) \\ \chi_2 = \chi_{2L} + \chi_{2R} &= \sin\alpha(\nu_L + (\nu_L)^c) + \cos\alpha(\nu_R + (\nu_R)^c) \end{aligned} \tag{I.3}$$

We can see that in the presence of Dirac and Majorana terms, the mass eigenstates χ are Majorana particles.

†h.c. stands for hermitian conjugate

4 The see-saw mechanism.

In the limiting case where $m_R \gg m_D \gg m_L$, such that m_L is negligible with respect to the other masses, the diagonalisation yields two eigenstates $\chi_1 \approx \nu_L$ and $\chi_2 \approx (\nu_R)^c$ with eigenvalues $m_1 \approx \frac{m_D^2}{m_R}$ and $m_2 \approx m_R$.

The assumption of a vanishing m_L is reasonable : the introduction of a left-handed Majorana mass coupling of the neutrino to its charge conjugate partner implies the introduction of a Higgs triplet

$$\Delta = \begin{pmatrix} \Delta^0 \\ \Delta^- \\ \Delta^{--} \end{pmatrix}$$

Δ^0 couples to the Z^0 and W bosons, and its expectation value, necessary to yield m_L modifies the value of $\rho_0 \equiv \frac{M_Z^2}{M_W^2 cos^2\theta_w}$. In the Standard Model $\rho_0 = 1$. Standard Model fits to the experimental data give $\rho_0 = 1.0012 \pm 0.0012 \pm 0.0018$ at M_{Higgs}=300 GeV[II.63] where the first error is the combination of theoretical and experimental uncertainties and the second comes from varying the Higgs mass from 60 to 1000 GeV. This excellent agreement puts upper limits on the ratio of the vacuum expectation values of extra Higgs multiplets to the vacuum expectation of the Higgs doublet(s) of the order of a few percent. This limit does not, however, rule out at all the possibility of such a Higgs triplet.

The assumption of this mass hierarchy produces a very light left handed neutrino and a very heavy right-handed neutrino, this process is called the see-saw mechanism.

While no theoretical argument can be given for a neutrino hierarchy, common prejudice often takes $m_D \sim m_{lD}$ and assumes a universal m_R when generalising this effect to the three known families of neutrinos, thus predicting a mass hierachy of the light neutrinos: the m_{lD} (l=e,μ,τ) are taken similar to the masses of the quarks or charged leptons of the same generation and m_R ranges in order of magnitude from 1 TeV to 10^{16} GeV in Grand Unification theories.

$$\frac{m_{\nu_e}}{m_{u,e}^2} \approx \frac{m_{\nu_\mu}}{m_{c,\mu}^2} \approx \frac{m_{\nu_\tau}}{m_{i,\tau}^2}$$

F Neutrino oscillations.

Generalising the mass terms to the case of three families, m_D, m_L and m_R become three 3×3 matrices. In the case of Dirac (Majorana) mass terms, if the mass matrix m_D (m_L,m_R) is non diagonal, neutrinos mix and can therefore oscillate between the different flavours. Let us consider a beam of neutrinos of flavour l (l=e,μ,τ) and fixed momentum **p**, much larger than any of the low mass eigenvalues.

$$|\nu_l> = \sum_\alpha U_{l\alpha}^* |\alpha, L> \quad \text{and} \quad |\bar{\nu}_l> = \sum_\alpha U_{l\alpha} |\alpha, R>$$

where U is a unitary matrix, $|\alpha, L>$ ($|\alpha, R>$) is the state vector of the left-(right-)handed (anti)neutrino of mass m_α, α runs from 1 to 3. (In the case of Dirac-Majorana mass terms, α would run from 1 to 6 and the $|\nu_l>$ would also be composed of sterile left-handed antineutrino state vectors.)

1 Neutrino oscillations in vacuum.

In vacuum, the evolution in time of $|\nu_l>$ is described by :

$$|\nu_l>_t = e^{-iH_0 t}|\nu_l>$$

where H_0 is the free Hamiltonian with eigenstates :

$$\begin{aligned} H_0|\alpha, L> &= E_\alpha|\alpha, L> \\ E_\alpha &= \sqrt{m_\alpha^2 + \mathbf{p}^2} \end{aligned} \tag{I.4}$$

such that :

$$|\nu_l>_t = \sum_\alpha |\alpha, L> e^{-iE_\alpha t} U_{l\alpha}^*$$

The probability that a neutrino of type l emitted at t=0 will behave as a neutrino of type l' at time t is given by the amplitude:

$$A_{l,l'}(t) = \sum_\alpha U_{l'\alpha} e^{-iE_\alpha t} U_{l\alpha}^* \tag{I.5}$$

The general form for the transition probability between 2 states $\nu_l, \nu_{l'}$ is therefore :

$$P_{\nu_l \to \nu_{l'}} = \sum_{\beta,\alpha} U_{l'\alpha} U_{l\alpha}^* U_{l\beta} U_{l'\beta}^* e^{-i(E_\alpha - E_\beta)t}$$

or, using the unitarity of the U matrix :

$$P_{\nu_l \to \nu_{l'}} = \delta_{ll'} - 2Re \sum_{\beta>\alpha} U_{l'\alpha} U_{l\alpha}^* U_{l\beta} U_{l'\beta}^* (1 - e^{\frac{-i(m_\alpha^2 - m_\beta^2)L}{2E}}) \tag{I.6}$$

where the following approximations were made: $E_i \approx \mathrm{p} + \frac{m_i^2}{2\mathrm{p}}$, p≈E and L≈t[‡] (c=1). Formula I.6 shows that the oscillation probability is a periodic function of the ratio $\frac{L}{E}$ and depends both on the mixing matrix and on the differences $m_\alpha^2 - m_\beta^2$. Neutrino oscillations can only be observed if the ratio $\frac{E}{L}$ is smaller or of the order of at least one of the differences of masses squared. Figure I.1 illustrates neutrino propagation in the presence or not of neutrino oscillations.

[‡]L represents the distance from the neutrino source

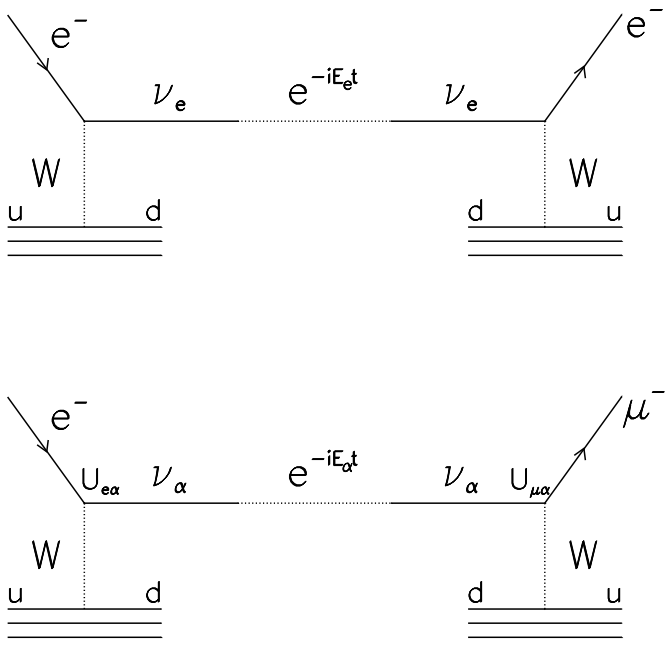

Figure I.1: *Examples of neutrino propagation in the absence (presence) of oscillations : top (bottom) figure.*

2 Simple case: two families oscillations

For the case of two families, it can be shown that in the framework of the Standard Model the elements of the matrix U can be chosen real; U is orthogonal. For two families l and l', it can thus be taken to be a simple rotation matrix :

$$U = \begin{pmatrix} \cos\theta & -\sin\theta \\ \sin\theta & \cos\theta \end{pmatrix} \tag{I.7}$$

θ is called the mixing angle and

$$\begin{aligned} \nu_l &= \cos\theta\nu_1 - \sin\theta\nu_2 \\ \nu_{l'} &= \sin\theta\nu_1 + \cos\theta\nu_2 \end{aligned} \tag{I.8}$$

where ν_1 and ν_2 are the mass eigenstates with masses m_1 and m_2.
Writing $\Delta m^2 = |m_1^2 - m_2^2|$, the transition probability becomes :

$$P_{\nu_1 \to \nu_2} = \sin^2 2\theta \sin^2 \frac{\Delta m^2 L}{4E} \tag{I.9}$$

The oscillation length in vacuum is $L_v = \frac{4\pi E}{\Delta m^2} \approx 2.47 \frac{E(GeV)}{\Delta m^2(eV^2)}\ km$. For neutrino oscillations to be observable, the distance between the source and the detector has to be at least

of order L_v. The sensitivity of experiments to small Δm^2 will be greater the smaller the $\frac{E}{L}$ ratio. Table 1.1 shows the sensitivities in Δm^2 for typical neutrino sources and values of L.

Source	Energy	Distance	$\Delta m^2(eV^2)$ sensitivity
Sun	100 keV-10 MeV	10^8 km	10^{-11}
Atmosphere	100 MeV-10 GeV	10 - 10000 km	10^{-3}
High Energy Accelerators	1-100 GeV	1 km	1
Low energy Accelerators	10 MeV	100 m	10^{-1}
Nuclear Reactors	1 MeV	100 m-1 km	10^{-2} 10^{-3}

Table 1.1: *Experimental Δm^2 sensitivities for typical source energies and source-detector distances.*

3 Neutrino oscillations in matter.

Neutrino oscillations will be affected by the passage of neutrinos through matter [I.8]. The presence of matter can be taken into account by adding a potential V to the free Hamiltonian H_0. Since normal matter contains electrons but no muons or taus, V will act differently on ν_e for which the elastic scattering on electrons happens via both neutral and charged current and on ν_μ or ν_τ for which only neutral current is possible (cf figure I.2).

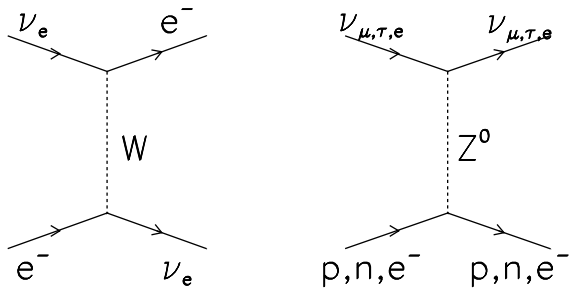

Figure I.2: *Possible neutrino scattering diagrams in matter.*

Considering the two ν_e and ν_μ families, V is of the form :

$$\begin{aligned} V|\nu_e> &= (C+\sqrt{2}G_F\rho_e)|\nu_e> \\ V|\nu_\mu> &= C|\nu_\mu> \end{aligned} \qquad \text{(I.10)}$$

where C is a constant representing the neutral current interactions of ν_e and ν_μ with electrons, protons and neutrons in the matter and G_F is the Fermi coupling constant. These interactions are the same at first order for ν_e and ν_μ and introduce a common phase shift which does not matter for oscillation studies. ρ_e is the density of electrons in the

traversed medium. The new Hamiltonian H_m for the weak eigenstates propagating in matter can be expressed using equations I.4,I.8 and I.10.

$$H_m = \begin{pmatrix} E_1 \cos^2\theta + E_2 \sin^2\theta + C + \sqrt{2}G_F\rho_e & -(E_2 - E_1)\sin\theta\cos\theta \\ -(E_2 - E_1)\sin\theta\cos\theta & E_2\cos^2\theta + E_1\sin^2\theta + C \end{pmatrix} \quad \text{(I.11)}$$

or

$$H_m = (E_1\cos^2\theta + E_2\sin^2\theta + C)\cdot\mathbf{I} + \begin{pmatrix} \sqrt{2}G_F\rho_e & -\frac{1}{2}(E_2 - E_1)\sin 2\theta \\ -\frac{1}{2}(E_2 - E_1)\sin 2\theta & (E_2 - E_1)\cos 2\theta \end{pmatrix} \quad \text{(I.12)}$$

The angle θ_m needed to diagonalise H_m can be expressed as a function of the local density:

$$\tan 2\theta_m = \frac{-(E_2 - E_1)\sin 2\theta}{\sqrt{2}G_F\rho_e - (E_2 - E_1)\cos 2\theta} \quad \text{(I.13)}$$

such that:

$$\sin^2 2\theta_m = \frac{\sin^2 2\theta}{1 - 2\cdot\frac{2\sqrt{2}\rho_e G_F E}{\Delta m^2}\cos 2\theta + (\frac{2\sqrt{2}\rho_e G_F E}{\Delta m^2})^2} \quad \text{(I.14)}$$

where $\Delta m^2 = m_2^2 - m_1^2$ and the same approximations were made as for equation I.6. The weak eigenstates are now expressed in terms of the matter propagation eigenstates.

$$\begin{aligned} |\nu_e> &= \cos\theta_m|\nu_1>_m - \sin\theta_m|\nu_2>_m \\ |\nu_\mu> &= \sin\theta_m|\nu_1>_m + \cos\theta_m|\nu_2>_m \end{aligned} \quad \text{(I.15)}$$

For low electron density, θ_m is the vacuum mixing angle and the matter propagation eigenstates are equal to the vacuum mass eigenstates. However small the mixing angle in vacuum, the oscillations can be enhanced by the presence of matter. The enhancement is the largest for

$$\rho_e = \rho_R = \frac{\Delta m^2\cos 2\theta}{2\sqrt{2}G_F E} \quad \text{(I.16)}$$

when $\theta_m = \frac{\pi}{4}$ so that the mixing between ν_e and ν_μ is maximal. Equation I.16 is called the resonance condition. For neutrinos, resonance can only be reached if $m_2 > m_1$. The same condition can be obtained for antineutrinos, with the opposite sign, such that resonant oscillations can only happen for antineutrinos if $m_1 > m_2$. Figure I.3 shows the effective mass of the propagation eigenstates and the weak eigenstates as a function of the electron density in the case of a small vacuum mixing angle.

Equation I.14 can be reformulated in terms of the oscillation length in vacuum L_v and of a parameter L_0 characterising the medium traversed: $L_0 = \frac{2\pi}{\sqrt{2}\rho_e G_F}$:

$$\sin^2 2\theta_m = \frac{\sin^2 2\theta}{1 - 2\cdot\frac{L_v}{L_0}\cos 2\theta + (\frac{L_v}{L_0})^2} \quad \text{(I.17)}$$

and the oscillation length in matter L_m is given by

$$L_m = \frac{L_v}{\sqrt{1 - 2\frac{L_v}{L_0}\cos 2\theta + (\frac{L_v}{L_0})^2}} \quad \text{(I.18)}$$

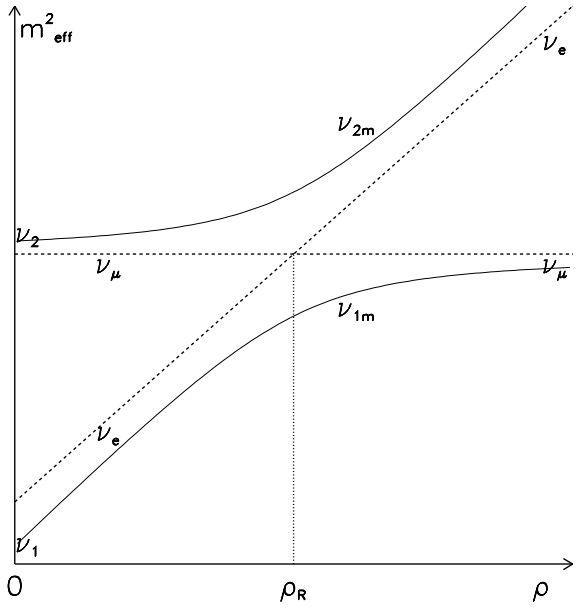

Figure I.3: *Effective mass of neutrinos in matter for $m_2 > m_1$ and a small vacuum mixing angle. The dashed lines are the expectation value for the weak eigenstates, the solid lines represent the propagation eigenstates.*

At resonance ($\sin^2 2\theta_m$=1), $\frac{L_\nu}{L_0} = \cos 2\theta$ and $L_m = \frac{L_\nu}{|\sin 2\theta|}$. The half width at half maximum of the resonance is $\Delta\rho_R = \rho_R \tan 2\theta$.

Several experiments (cf. chapter II) measure the flux of neutrinos produced in the sun. They observe a deficit which could be explained by matter enhanced oscillations. In the sun, if the core density is larger than the resonance density of the ν_e 's produced, they will go through a region where the electron density is ρ_R. The resonance enhancement will be sizeable only if the thickness of the layer of density close to the resonance density is at least of the order of the oscillation length in matter. Another important issue is the fact that, if the matter density of the medium changes, the propagation eigenstates have to be reevaluated at each point. If the density varies slowly enough, however, the propagation states will remain eigenstates of H_m, their composition in ν_e and ν_μ varying according to ρ_e, this is called the adiabatic regime.

The adiabatic condition can be expressed at resonance as:

$$(\frac{d\rho}{dr})^{-1}\Delta\rho_R > L_m \tag{I.19}$$

or :

$$\frac{d\rho}{dr} < \frac{(\Delta m^2)^2 \sin^2 2\theta}{8\pi\sqrt{2}G_F E^2} \tag{I.20}$$

When a ν_e is created in the core of the sun, the density is such that it is composed of ν_{2m}. If the adiabatic condition is fulfilled, ν_{2m} remains an eigenstate through to the sun's surface where $\rho_e \approx 0$ such that $\nu_{2m} \simeq \nu_2$ is essentially composed of ν_μ . This effect is called the Mikheev-Smirnov-Wolfenstein (MSW) effect and for the values considered leads to an almost complete disappearance of ν_e . The process being energy dependent, for ν_e energies

much below resonance, no conversion occurs, for higher energies for which the adiabatic condition ceases to be fulfilled only partial conversion occurs.

Note that, as ν_e are created in the sun and not $\bar{\nu}_e$, the MSW effect can only occur if $m_2 > m_1$, and this could be used in favour of a mass hierarchy of the neutrinos as discussed in section D.4, if experimentally proven.

References

[I.1] C. Jarlskog, *Neutrino, a theoretical introduction*,Ecole de Gif-sur-Yvette 24^{th} session 13-18 September 1992, Volume 1, p 91, 1992.
J. Bouchez, *La physique du neutrino auprès des réacteurs nucléaires*,Ecole de Gif-sur-Yvette 24^{th} session 13-18 September 1992, Volume 1, p 93, 1992.
S. Bilenky, *Lepton Mixing*, Neutrino physics, p 177, Cambridge University Press, 1991.
R.N. Mohapatra and P.B. Pal,*Massive neutrino physics and astrophysics*, World Scientific Publishing,1991.

[I.2] M. Kobayashi, T. Maskawa, Prog. Theor. Phys. **49**, 652 (1973)

[I.3] LEP Collaborations *et al.*, CERN-PPE/97-154, 1997.

[I.4] C.L. Cowan *et al.*,*Detection of the free neutrino*,Neutrino physics, p41, Cambridge University Press, 1991.

[I.5] W. Pauli,*On the earlier and more recent history of the neutrino*,Neutrino physics, p1, Cambridge University Press, 1991.

[I.6] G. Danby *et al.*,*Phys. Rev. Lett.* **9**, 36 (1962).

[I.7] V. Paolone, E872 note, http://fn872.fnal.gov/pn/e872_inter_rate.ps, 1997.

[I.8] S.P. Mikheev amd A.Y. Smirnov,Yad.Fiz **42**, 1441 (1985).
L. Wolfenstein,*Phys. Rev.* D **17**, 2369 (1978).

Chapter II Physics Motivation

Massive neutrinos of a few eV make a good candidate for dark matter in the universe as described in section A. If they also oscillate, this could be the solution to the experimental puzzles described in section B. The current results of dedicated neutrino oscillation experiments are also reviewed in that section. Several ways to probe the neutrino mass in a direct fashion are presented in section C.

A Cosmological constraints.

The Hot Big Bang model has become the standard cosmological model of the universe. It predicted among other things a relic cosmic microwave background (CMB) radiation. This background has been observed and its spectrum measured to fit a black body radiation at 2.7 K. This section introduces the problem of dark matter in cosmological models of the universe and how the neutrino could partially solve it. It also shows how cosmology can constrain the mass and the lifetime of neutrinos. [II.1, II.2, II.3, II.4]

1 Constraint on the mass of light neutrinos.

Initially, when the temperature of the universe is very high, all particles are in thermal equilibrium. As the universe expands, the temperature diminishes. Particles remain in equilibrium with the radiation as long as the temperature of the radiation is high enough for its energy kT to be as large as their mass. The time at which these two energies are equal, is called the decoupling time for these particles. The requirement that the total energy density in the universe is lower or equal than the critical density (ρ_c) needed to close the universe (i.e.: prevent it from reaching its present age) allows to put a limit on the neutrino mass.

$$\rho_c = \frac{3H^2}{8\pi G}$$

where G is Newton's constant and H is the Hubble "constant" characterising the expansion rate of the universe. H_0 (the subscript 0 denotes present day values) is usually expressed in terms of the normalised Hubble constant as H_0=100$\cdot h_0$ $km\cdot s^{-1}Mpc^{-1}$. Current observations based on the most reliable methods show that $0.6 \leq h_0 \leq 0.8$ [II.5]. So:

$$\rho_c \simeq 10.5 h_0^2 \; keV \; cm^{-3} \qquad \text{(II.1)}$$

If neutrinos are stable and light ($m_\nu \leq 1$ MeV), they are relativistic when they decouple from the photons (at $\simeq$ 1.5-2 MeV). Let us call the temperature of the universe at that time T_ν. The ratio of their number density n_ν to the number density of photons n_γ would remain unchanged if no later process destroyed or created photons or neutrinos in numbers of the order of n_γ. At 0.5 MeV, e^+ e^- annihilation is not compensated by pair creation anymore and the microwave photon background heats up.

The entropy density s of a relativistic gas is given as a function of the pressure p, the energy density ρ and the temperature T by:

$$\mathrm{s} = \frac{p+\rho}{T} \quad = \quad \frac{4\rho}{3T} \quad \text{as } p = \frac{\rho}{3} \text{ for relativistic particles.}$$

If the universe expands adiabatically, one can show that the temperature of relativistic particles falls as R^{-1}. The fact that the energy density $\rho = \frac{\pi^2}{30} g T^4$ (bosons) or $\rho = \frac{7}{8}\frac{\pi^2}{30} g T^4$ (fermions) is proportional to T^4 then implies that the entropy per comoving volume R^3 is conserved where g is the number of degrees of freedom (i.e: spin polarisation states). The new temperature T_γ is given by entropy conservation. Replacing ρ in the expression of entropy before (for γ,e^- and e^+) and after annihilation (only γ) :

$$(2 + \tfrac{7}{8} \times 2 \times 2) T_\nu^3 = 2 \times T_\gamma^3$$

where there are 2 degrees of freedom for the photons, the electron and positron.

$$T_\nu^3 = \frac{4}{11} T_\gamma^3 \tag{II.2}$$

Since no later process will heat up the background radiation, the relationship II.2 between the photon and the neutrino gas stays valid as the universe goes on expanding. Fermi-Dirac statistics yield the following relationship between the number density of neutrinos n_ν and their temperature : $n_\nu = \frac{3}{4}\frac{\zeta(3)}{\pi^2} g T_\nu^3$ where $\zeta(3)$=1.202 is a Riemann zeta function and g is the number of degrees of freedom. Equation II.2 and the measured CMB temperature (2.726 K [II.8]) then yield the present neutrino number density :

$$\begin{aligned} n_{\nu 0} &= \tfrac{3}{4}\tfrac{\zeta(3)}{\pi^2} \times 2 \times \tfrac{4}{11} T_{\gamma 0}^3 \\ &= 113 \text{ cm}^{-3} \end{aligned}$$

As if neutrinos are massive, they are nowadays non relativistic and their energy density can be expressed as $\rho = m \cdot n$. Equation II.1 then yields the constraint :

$$m_\nu = \frac{\rho_\nu}{n_\nu} \leq \frac{\rho_c}{n_\nu} \leq 92 h^2 \text{ eV}$$

This argument is valid for any neutrino species, so that the constraint can be put on the sum of the neutrino masses:

$$\sum m_{\nu,i} \leq 92 h^2 \text{ eV}$$

If one considers the neutrino to be unstable, two-dimensional bounds can be set on their lifetime versus their mass, by the same argument that their energy density must be small enough not to close the universe.

2 Dark matter

Astronomical observations such as the following example point to the fact there must be matter in our universe which we cannot detect by effects other than gravitational because it does not radiate. This matter is called *dark matter* (DM).
The velocity of stars as a function of their distance to the centre of a galaxy can be expressed as :

$$\begin{aligned} \frac{GM(r)m}{r^2} &= \frac{mv^2}{r} \\ v &= \sqrt{\frac{GM(r)}{r}} \end{aligned}$$

where G is Newton's constant, v is the velocity of the star, r the distance of the star to the centre of the galaxy, M(r) is the mass of the galaxy contained within the distance r. For stars far away (> 10 Mpc) from the centre of the galaxy, the visible mass does not increase with the distance anymore. One would expect the velocity of stars in that region to drop as $r^{-\frac{1}{2}}$. However, the observed velocity distribution flattens out at large radii as shown in figure II.1. Such behaviour can be explained if M(r) increases undetected via dark matter

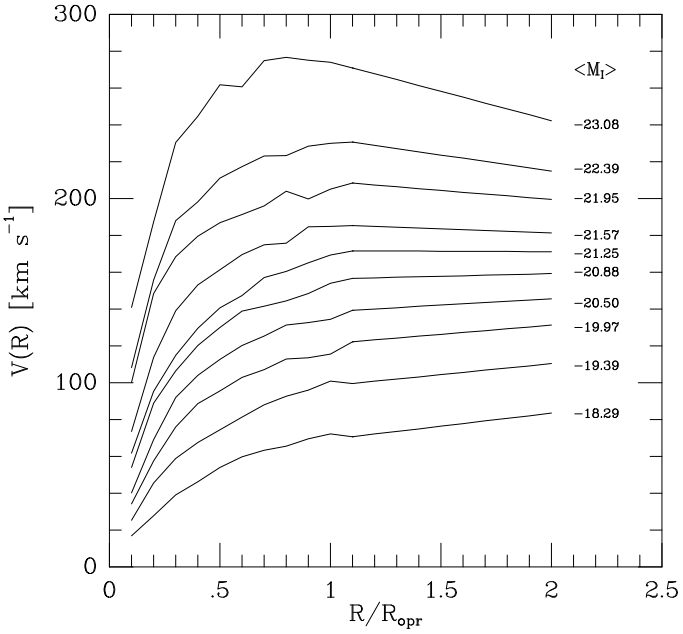

Figure II.1: *Velocities of stars in function of their distance R to the centre of galaxies for galaxies of different magnitudes M. R_{opt} is called the optical radius and is a measurement of the visible radius of the galaxy.[II.6]*

present in the galaxy. A principle of cosmology is that the universe is homogeneous and isotropic, at least on large scales. However, this is not observed on "small" scales as we see stars, galaxies, clusters, etc... separated by large empty spaces. Primordial fluctuations in the energy density can be introduced at a very early stage in cosmological models. These perturbations would later form the observed structures. They can grow or get damped depending on which type of matter is present and interacts in the universe. The measurement of the age, the number and distances of galaxies, clusters, and superclusters of galaxies allows to determine what contributes to the DM.

There are several candidates for DM. They are classified as hot, warm and cold depending on whether they were relativistic, just relativistic or already non-relativistic when they decoupled from the photons during the first seconds after the big bang.

The COBE satellite measurement [II.7] of the angular fluctuation of the microwave background radiation gives a handle on the primordial fluctuations. Its data allows to test the

prediction of cosmological models with different DM contents and values of parameters such as the cosmological constant Λ, the Hubble constant, the fraction of energy density compared to the critical density.

- Light neutrinos are the standard form of Hot Dark Matter (HDM). Cosmological models containing HDM only are disfavoured as the constraint on the mass of such a light relativistic weakly interacting particle (cf. section A.1) is such that, if they constitute the entire dark matter, they would have washed out all structures smaller than 15 $M_{\odot}$, hardly leading to any structure formation at all.

- Right-handed neutrinos or gravitinos could form Warm Dark Matter. Although these particles are heavier and less abundant by about an order of magnitude, WDM models encounter the same lack of structure formation as HDM models.

- Cold DM could be composed of Massive Astrophysical Halo Objects (MACHO's: brown dwarfs, neutron stars...) or Weakly Interacting Massive Particles (WIMP's: supersymmetric particles, axions...). The two detectors MACHO [II.9] and EROS [II.10] have detected 8 and 2 events of microlensing of stars in Large Magellanic Cloud in 2.3 and 3 years of datataking, respectively. This number of events is in excess with respect to the expected number of events from the known stars. These events suggest as origin of this phenomenon objects of $\sim 0.1 - 0.8 M_{\odot}$ with a density of 20-50% of the mass of the Milky Way halo in a 20 kpc radius). The CDM models reproduce rather well the observed universe, but when normalised to the COBE data, they seem to overproduce clusters. Adding a non zero cosmological constant (ΛCDM) yields a better agreement with the data.

- Another promising range of cosmological models are made out of mixed dark matter: HCDM, with a hot fraction of ~ 0.2 which damps the fluctuations on small scales. A neutrino with a mass of a few eV would be a perfect candidate for the HDM admixture.

B Neutrino Oscillations.

1 The solar neutrino problem.

Electron neutrinos ν_e are produced in the core of the sun essentially via the processes of the pp cycle described in table 2.1 [II.11]. One full cycle of reactions is equivalent to the following reaction :

$$4\mathrm{H} \rightarrow {}^4\mathrm{He} + 2\mathrm{e}^+ + 2\nu_e + 26.73\ \mathrm{MeV} \qquad <\mathrm{E}(2\nu_e)> = .59\ \mathrm{MeV}$$

Various versions of the Standard Solar Model (SSM) [II.14, II.15, II.18] predict the ν_e fluxes which should reach the Earth for the different neutrino energies. The versions differ mainly by chosen values of poorly known or unknown parameters and by the introduction or not of complex physical effects. Experiments were designed to measure the neutrino spectrum and flux coming from the sun, to test the sun models. Figure II.2 shows the solar neutrino spectrum and the energy threshold of several experiments [II.22]. The first experiment to give results was the Homestake experiment [II.21], it measured a neutrino flux lower

than the SSM predictions by more than a factor two [II.12]. These controversial results triggered the development of new experiments sensitive to different parts of the spectrum:

Reaction	Neutrino Energy (MeV)		Sensitive Experiments
$p + p \rightarrow {}^2H + e^+ + \nu_e$	0.0 to 0.4	(*pp*)	SAGE, GALLEX
or $p + e^- + p \rightarrow {}^2H + \nu_e$	1.4	(*pep*)	SAGE, GALLEX
${}^2H + p \rightarrow {}^3He + \gamma$			
${}^3He + {}^3He \rightarrow {}^4He + 2p$			
or ${}^3He + {}^4He \rightarrow {}^7Be + \gamma$			
$e^- + {}^7Be \rightarrow {}^7Li + \nu_e$	0.86 (90%), 0.38 (10%)	(*Be*)	SAGE, GALLEX,
${}^7Li + p \rightarrow {}^4He + {}^4He$			HOMESTAKE
or			
$p + {}^7Be \rightarrow {}^8B + \gamma$			SAGE, GALLEX,
${}^8B \rightarrow {}^8Be + e^+ + \nu_e$	0. to 14.	(*B*)	HOMESTAKE,
${}^8Be \rightarrow {}^4He + {}^4He$			(SUPER)KAMIOKANDE

Table 2.1: *The principal neutrino producing reactions of the pp cycle. The reactions which do not involve neutrinos are included for coherence of the cycle.*

- The Homestake experiment captures ν_e via the reaction ${}^{37}Cl + \nu_e \rightarrow {}^{37}Ar + e^-$, with an energy threshold of 814 keV. It is sensitive to the *B*,*Be* and *pep* neutrinos. The ${}^{37}Ar$ is extracted chemically from the sample after a few weeks and analysed, and the nuclei are counted by detecting the ${}^{37}Ar$ radioactive decay. Its latest results [II.20] show a clear deficit in the observed flux ($2.56\pm.25$ SNU*) compared to the predicted flux (7.7 ± 1.2 SNU [II.14]).

- The Gallex and Sage experiments capture ν_e via the reaction ${}^{71}Ga + \nu_e \rightarrow {}^{71}Ge + e^-$. This reaction has a threshold of 233 keV. The ${}^{71}Ge$ is extracted chemically from the sample every few weeks and analysed, and the ${}^{71}Ge$ nuclei are counted by detecting their radioactive decay. They are sensitive to all four reactions considered in table 2.1, but their signal comes mainly from the *pp* neutrinos. They observe $77.5\pm6.2(\text{stat})^{+4.3}_{-4.7}(\text{syst})$ SNU in GALLEX [II.19] and 72 ± 12 SNU in SAGE [II.23] compared to a predicted flux of 129 ± 8 SNU [II.14].

- The (Super-)Kamiokande detector detects the ν_e -e^- scattering in a water tank instrumented with photo-multipliers. Their threshold is (5) 7.6 MeV. It is sensitive only to the *B* neutrinos. The final result of the Kamiokande experiment yields a flux of $2.80\pm0.40 \times 10^6$ cm^{-2} s^{-1} [II.24] confirmed by the results from the Super-Kamiokande experiment, which after 504 days of datataking yields a flux of $2.44\pm0.05(\text{stat})^{+0.09}_{-0.07}(\text{syst})$ 10^6 cm^{-2} s^{-1}[II.25]. This last result corresponds to a Data/SSM of $0.474^{+0.010+0.017}_{-0.009-0.014}$ using the latest calculation by Bahcall [II.14].

*The SNU is the solar neutrino unit, 1 SNU $\equiv 10^{-36}$ captures per target atom per second.

The current experimental results and the predictions of Bahcall and Pinsonneault [II.14] are shown in figure II.2.

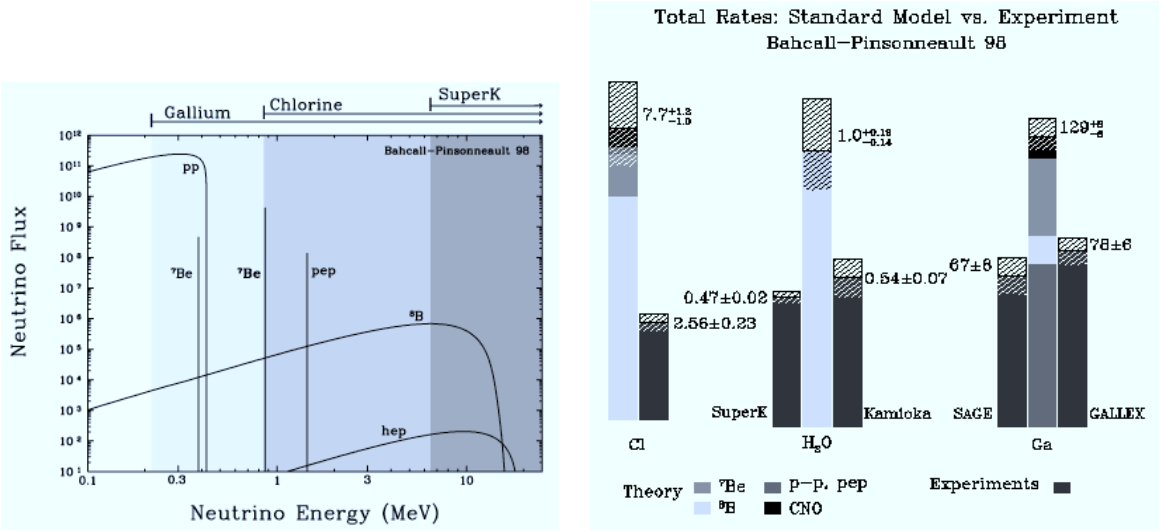

Figure II.2: *Expected solar neutrino fluxes and energy thresholds of the current experiments* (Left) *and the present experimental results (in SNU)* (Right), *beside the theoretical predictions from Bahcall and Pinsonneault [II.14].*

All four experiments show a deficit in the solar neutrino flux compared with that predicted by the SSM. To address this problem, the sun models have been improved over 30 years including more and more complex effects [II.15]. More precise measurements of important parameters are included as they became available, such as the cross sections of the nuclear reactions, which are poorly known. Various models are available using different possible values of the parameters.
Table 2.2 summarises the predictions of different solar models and the experimental results.

ν flux	BP98 [II.14]	DS96 [II.15]	T-CL93 [II.18]	Observed
$\phi_\nu(^8\mathrm{B})$ $[10^6 cm^{-2} s^{-1}]$	5.15	2.49	4.4±1.1	2.44±0.09 (SK)
$\sum(\phi\sigma)_{Cl}$ [SNU]	$7.7^{+1.2}_{-1.0}$	4.1±1.2	6.4±1.4	2.56±0.25 (Hom.)
$\sum(\phi\sigma)_{Ga}$ [SNU]	129^{+8}_{-6}	115±6	122±7	77±8 (Gall.)
				72±12 (Sage)

Table 2.2: *Prediction of various SSM and the results of the experiments. The models from Bahcall and Pinsonneault (BP98) and from Dar and Shaviv (DS96) include diffusion of the heavy elements towards the core, the model from Turck-Chièze and Lopes (T-CL93) does not and is not compatible with helioseismological observations.*

The comparison between the prediction of the ^{8}B ν_e flux to be observed in the other experiments from the results of the Kamiokande experiment and the measurements of

these experiments implies that the flux of ^{7}Be neutrinos reaching the Earth must vanish, if all experiments are correct.
Solutions to this problem can come from various sides :

- Many astrophysical effects can still be included in the SSM which might help decrease the expected ^{7}Be ν_e flux and solve the problem: e.g. the differential rotation of the sun, its magnetic field, its mass and angular momentum losses since the beginning of its evolution.

- The nuclear ν_e absorption cross sections at threshold in the ^{37}Cl and ^{71}Ga for ν_e might also be overestimated. Lower absorption cross sections at threshold would provide room for ^{7}Be ν_e in the ^{71}Ga experiments by reducing the absorption of *pp* neutrinos, and reduce the expected contribution of ^{7}Be neutrinos in the ^{37}Cl experiment [II.15].

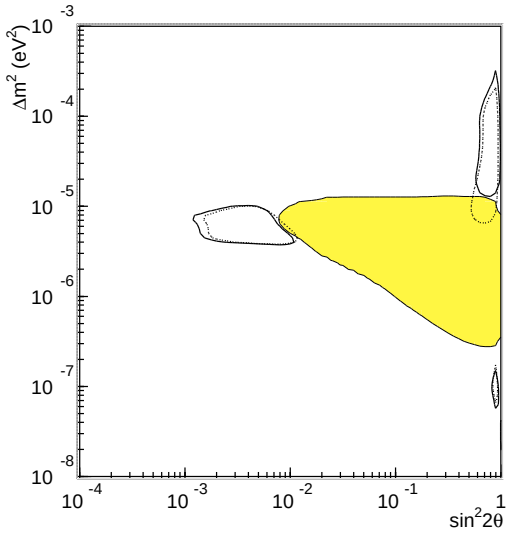

Figure II.3: *Results of the four solar neutrino experiments, in terms of possible neutrino oscillations solutions. The shaded area is the region excluded at 99%C.L.by Super-Kamiokande non observation of day-night effects. The regions in the dotted lines are allowed at 99%C.L. by the rate comparison between BP98 and the Ga, Cl, and Super-Kamiokande, the solid lines is the region allowed at 99%C.L. by the rate comparison analysis and the day-night effect analysis.*

- Neutrinos could oscillate in vaccuum between the Sun and the Earth and explain the observed deficit with a $\Delta m^2 \simeq 10^{-10}$ and $\sin^2(2\theta) \simeq 1$.

- Another interesting solution is resonant neutrino flavour conversion in the sun (the MSW effect described in section I.F.3) which also requires the neutrinos to have mass and to mix. This effect has the interesting feature that the reduction of flux varies with the neutrino energy and can accommodate the disappearance of the ^{7}Be neutrinos. Figure II.3 [II.26] shows the regions of parameter space Δm^2 - $\sin^2(2\theta)$ which are allowed by the present experimental results.

The present data do not allow to make definitive statements on whether the observed deficit is due to neutrino oscillations, to astrophysical effects or to both. However, Super-Kamiokande and future results from experiments such as SNO or Borexino will be able to answer this question. SNO will be able to measure and differentiate neutral from charged current neutrino interactions and to infer if the flux observed in neutral current mode is consistent with the SSM predictions, and if the ratio of neutral to charged current interaction points to neutrino oscillations. Borexino will be sensitive to the *Be* neutrino flux. The Super-Kamiokande experiment also measures the recoil spectrum of the electrons, allowing a direct comparison of the energy spectrum with that expected from ^{8}B as shown in figure II.4 The spectra agree with a probability of 4.6%, the poorness of the agreement being

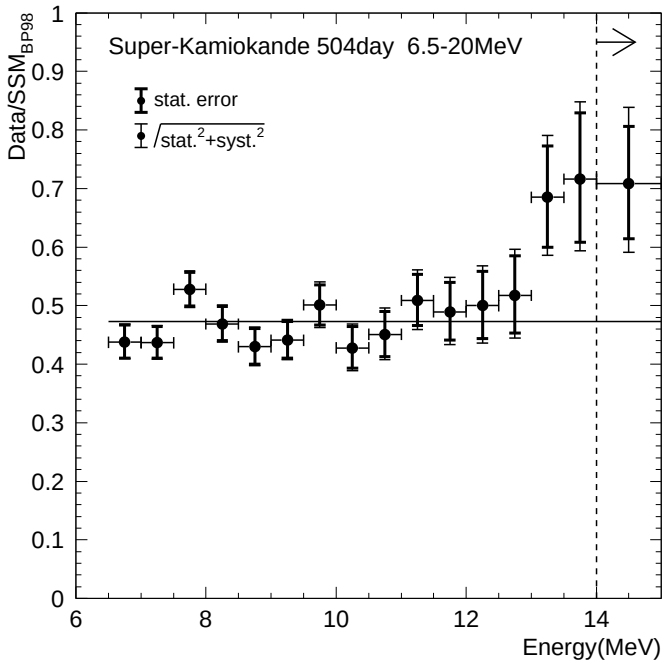

Figure II.4: *Ratio of the observed electron energy spectrum and the expectation from SSM, from [II.25].*

due to the excess of events in the high energy bins. This excess could be interpreted in terms of neutrino oscillations (in vaccum or matter enhanced), or alternatively be due to Hep neutrinos [II.27], the flux of which has a large uncertainty. SuperKamiokande also observes no day-night dependence of the neutrino flux [II.26].

2 The atmospheric neutrino problem.

Neutrinos are produced in atmospheric cosmic ray showers from the decays of mesons and muons, the main source being the decay chains :

$$\begin{aligned} \pi^+ &\rightarrow \mu^+ \ \nu_\mu \ , \qquad \mu^+ \rightarrow \mathrm{e}^+ \ \nu_\mathrm{e} \ \bar{\nu}_\mu \\ \pi^- &\rightarrow \mu^- \ \bar{\nu}_\mu \ , \qquad \mu^- \rightarrow \mathrm{e}^- \ \bar{\nu}_\mathrm{e} \ \nu_\mu \end{aligned} \tag{II.3}$$

Such that the ratio of $\nu_\mu + \bar{\nu}_\mu$ to $\nu_\mathrm{e} + \bar{\nu}_\mathrm{e}$ fluxes is expected to be approximately 2. There are large uncertainties concerning the absolute fluxes of ν_e ($\bar{\nu}_\mathrm{e}$) and ν_μ ($\bar{\nu}_\mu$) to expect from different models. However, all models yield approximately the same values for the ratio of the fluxes of muon (anti-)neutrinos to electron (anti-)neutrinos. The flavour content of atmospheric neutrinos has been measured in six underground experiments, which express their results in terms of a ratio of ratios R_t:

$$R_t = \frac{(\frac{\nu_\mu}{\nu_\mathrm{e}})_{DATA}}{(\frac{\nu_\mu}{\nu_\mathrm{e}})_{MC}} \tag{II.4}$$

This ratio corresponds empirically to the ratio of ratios R of non-showering to showering events:

$$R = \frac{(\frac{\text{non-showering events}}{\text{showering events}})_{DATA}}{(\frac{\text{non-showering events}}{\text{showering events}})_{MC}} \tag{II.5}$$

- Kamiokande [II.30], Super-Kamiokande [II.28] and IMB [II.31] are water Čerenkov detectors; they all measure a ratio of ν_μ to ν_e charged current events lower than what they expect from Monte Carlo calculations. The zenith angle distribution of the double ratio in the Kamiokande detector allowed to interpret this deficit in terms of neutrino oscillations as the neutrinos traverse different distances between their production point and the detector in function of the angle. Their favoured values of ($\Delta \mathrm{m}^2$,$\sin^2(2\theta)$) in terms of $\nu_\mu \rightarrow \nu_\mathrm{e}$ and $\nu_\mu \rightarrow \nu_\tau$ oscillations are (1.8 10^{-2} eV^2,1.0) and (1.6 10^{-2} eV^2,1.0), respectively.
  The ongoing Super-Kamiokande experiment also sees a zenith angle dependence of the μ-like events as shown in figure II.5. The zenith angle dependence of the multi-GeV e-like events is due to the fact that the parent muons do not decay before reaching the Earth. In the mean time, the Chooz reactor based experiment (cf. next section) ruled out the $\nu_\mu \rightarrow \nu_\mathrm{e}$ oscillation possibility such that the only available solutions in terms of oscillations are from ν_μ into a ν_τ or a sterile neutrino. The double ratio Data/MC of neutral current events to e-like events is close to 1 ($0.93 \pm 0.07(\mathrm{stat}) \pm 0.19(\mathrm{syst})$ [II.29]), in good agreement with the $\nu_\mu \rightarrow \nu_\tau$ oscillation hypothesis. The error, however is still too large to exclude the sterile neutrino hypothesis. The neutral current events selected are π^0 production events which are recognized by the 2 e-like Čerenkov rings produced by the 2 photons the π^0 decays into. Figure II.6 shows the invariant mass reconstructed for such events.

- Nusex [II.33], Macro [II.35], Soudan 2 [II.34] and Fréjus [II.32] are tracking iron calorimeters. Their collected statistics is much lower than the statistics collected by

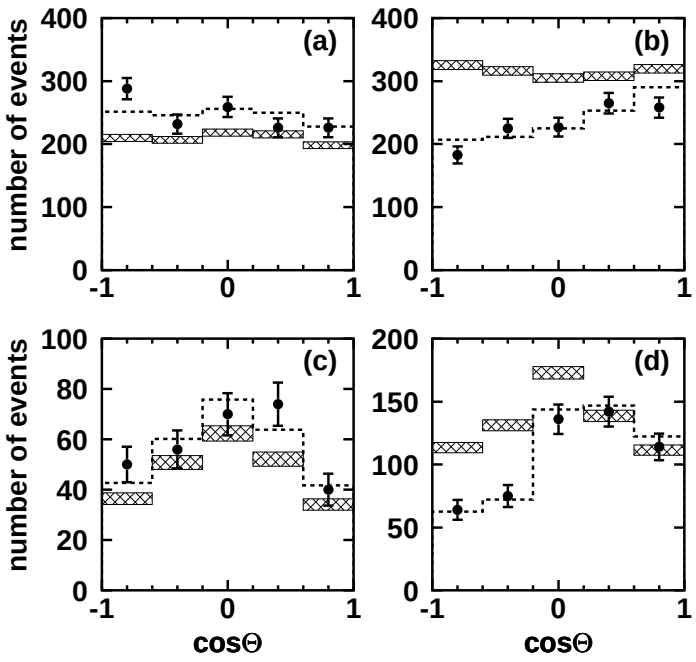

Figure II.5: *Zenith angle distribution of the number of events in the Super-Kamiokande detector (a) sub-GeV e-like (b) sub-GeV μ-like (c) multi-GeV e-like and (d) multi-GeV μ-like. The shaded regions is the Monte Carlo prediction without oscillations. The dotted line represents the best fit to* $\nu_\mu \rightarrow \nu_\tau$ *oscillations with* $\sin^2(2\theta) = 1$ *and* $\Delta m^2 = 2.2\ 10^{-3}$.

the water Čerenkov experiments. Nusex and Fréjus do not find significant disagreement with unity for R, and do not support the oscillation thesis, though they do not contradict it. The Soudan 2 and Macro experiments, however, are compatible with the Čerenkov experiments.

Table 2.3 shows the comparison between data and Monte Carlo for all experiments.

3 Reactor experiments.

Nuclear reactors are an abundant source of $\bar{\nu}_e$ of a few MeV produced in β-decay following the fission of heavy nuclei into unstable lighter nuclei. One can investigate the possibility of neutrino oscillations by searching for a disappearance of $\bar{\nu}_e$ away from the reactor. The main uncertainties are the initial flux and spectrum of the $\bar{\nu}_e$. Experiments place several detectors at different distances from the reactor, looking for the $\bar{\nu}_e + p \rightarrow e^+ + n$ reaction with a threshold of 1.8 MeV. Table 2.4 summarises the results in terms of oscillation $\bar{\nu}_e \rightarrow \bar{\nu}_x$ of the most recent experiments, all compatible with no signal.
The newer Chooz experiment, however, claims to control the $\bar{\nu}_e$ flux with 2% precision, such that with only one detector at 1 km, and no observed $\bar{\nu}_\mu$ signal, they managed to put a limit on the probability of $\bar{\nu}_e \rightarrow \bar{\nu}_\mu$ oscillations an order of magnitude better in $\sin^2(2\theta)$ than the previous experiments. The new Chooz experimental results cover the atmospheric neutrino oscillation region proposed by the (Super-)Kamiokande experiments, such that the explanation of their signal cannot be $\nu_\mu \rightarrow \nu_e$ oscillations.

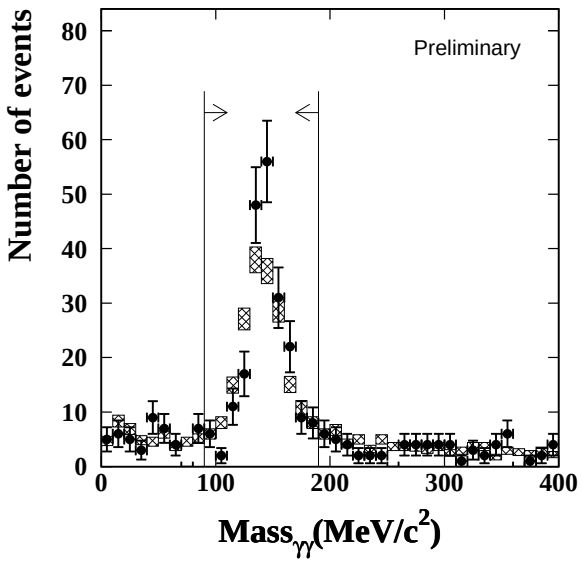

Figure II.6: *Observed invariant mass spectrum (data points) for events with 2 e-like rings and no μ-decay signal, along with the Monte Carlo prediction (shaded histogram). The cut in the π^0 mass region is also shown.*

experiment		exposure (kton.yr)	R
Kamiokande (sub-GeV)	[II.30]	7.7	$0.60^{+0.06}_{-0.05} \pm 0.05$
Kamiokande (multi-GeV)	[II.30]	14.2	$0.57^{+0.08}_{-0.07} \pm 0.07$
Super-Kamiokande	[II.28]	33	$0.65 \pm 0.05 \pm 0.08$
IMB	[II.31]	7.7	$0.54 \pm 0.05 \pm 0.12$
Macro	[II.35]		$0.74 \pm 0.036 \pm 0.046 \pm 0.13$
Soudan 2	[II.34]	2.83	$0.61 \pm 0.14^{+0.05}_{-0.07}$
Fréjus	[II.32]	2.0	$1.00 \pm 0.15 \pm 0.08$
Nusex	[II.33]	0.74	$0.96^{+0.32}_{-0.28}$

Table 2.3: *Experimental results of the atmospheric neutrino flavour content. The errors quoted are either combined or statistical and systematic in that order.*

Experiment	Distance to reactor	Δm^2 (eV^2) $\sin^2(2\theta)=1$	$\sin^2(2\theta)$ $\Delta m^2 \to \infty$
Gösgen [II.37]	36,46,65 m	$1.9\ \ 10^{-2}$	0.21
Krasnojarsk [II.39]	57,230 m	$0.7\ \ 10^{-2}$	0.15
Bugey 3 [II.38]	15,40,95 m	$1.0\ \ 10^{-2}$	0.2
Chooz[II.40]	1 km	$0.9\ \ 10^{-3}$	0.18

Table 2.4: *Upper limits set by the most sensitive $\bar{\nu}_e$ disappearance reactor experiments.*

4 Accelerator experiments

4.1 Low energy beams

Current experimental results

The KARMEN and LSND experiments use 800 MeV proton beams impinging onto a massive target, which mainly produces pions. The pions are stopped within the target and the π^- are captured. The π^+ decaying at rest produces a μ^+ which in turn decays at rest. Figure II.7 shows the spectra of the neutrinos produced in this decay chain.

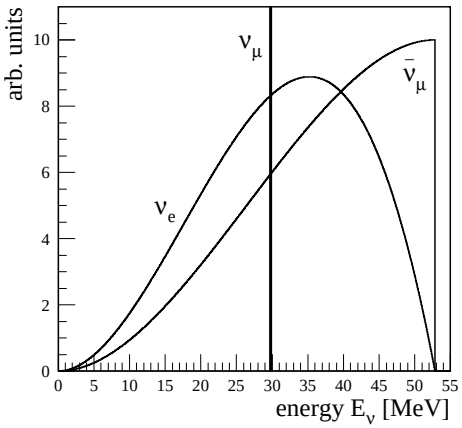

Figure II.7: *Neutrino energy spectra from* $\pi^+ \rightarrow \mu^+ \ \nu_\mu$ *decay at rest followed by* $\mu^+ \rightarrow \bar{\nu}_\mu \ e^+ \ \nu_e$ *decay at rest.*

These experiments are sensitive to $\bar{\nu}_\mu \rightarrow \bar{\nu}_e$ oscillations as the background from prompt $\bar{\nu}_e$ from π^- decay in flight followed by μ^- decay in flight is at the level of 10^{-3} . They look for inverse β-decay in their detector : the signal is the detection of an e^+ of a few tens of MeV in time coincidence with a neutron capture. The LSND collaboration claims an evidence for an excess of $\bar{\nu}_e$ events, resulting in an oscillation probability of $0.31 \pm 0.09 \pm 0.05$ %. They interpret this excess in terms of neutrino oscillations in this channel [II.41] and have confirmed their signal by analysing the $\nu_\mu \rightarrow \nu_e$ channel [II.42]. This analysis is more complicated due to the high prompt ν_e content in the beam, such that the 90% C.L. signal region is wider. KARMEN does not confirm this claim so far [II.43]. The present results of KARMEN2 and LSND are shown in figure II.8, together with limits from other experiments. Although the KARMEN2 seems to exclude the LSND signal, it is only due to the fact that it did not observe the 3 background events it expected, such that as they continue accumulating and analysing their data and eventually observe the expected background events, their limit will become less stringent. Although they upgraded their detector with better shielding, and resumed data taking, they will probably never be able to disprove the LSND claim, their sensitivity being still limited by background.

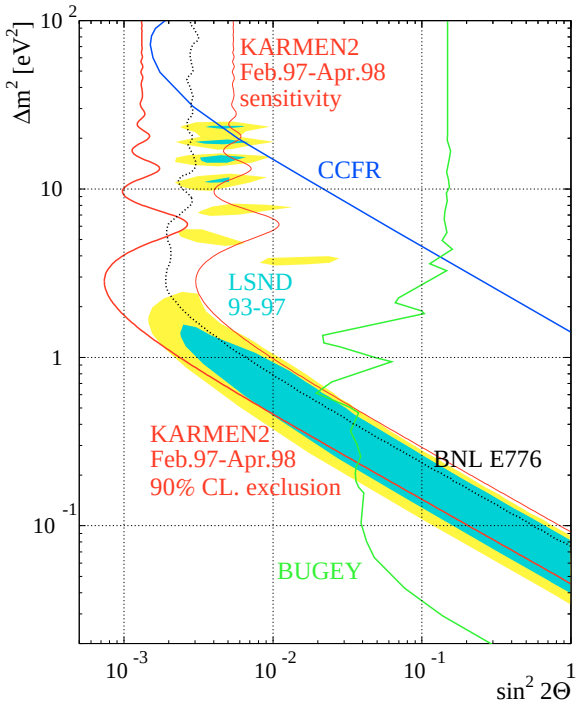

Figure II.8: *Results of the LSND and KARMEN experiments, the shaded area corresponds to the LSND claim (at 90% and 99% C.L.) and the two solid lines surrounding the LSND claim correspond to the region excluded at 90% C.L. by KARMEN and to its sensitivity, the dotted line to the region excluded by E776 and the light-grey line to the region excluded by the Bugey reactor experiment.*

Future medium energy beam experiments

Three medium energy beams are being conceived to clarify the situation of the $\nu_\mu \rightarrow \nu_e$ oscillations in the parameter space claimed by the LSND experiment. They are created by dumping protons of about 10 GeV onto a target, creating pions and kaons the decay of which gives rise mainly to muon (anti)neutrinos with a mean energy of 1-2 GeV. Figure II.9 shows the neutrino beam spectrum expected at the Mini-Boone experiment location site. The three foreseen experiments described in table 2.5 want to detect $\nu_\mu \rightarrow \nu_e$ oscillation by measuring the quasi-elastic ν_e and ν_μ interaction rates and comparing them at a close and a far detector, or with the expectation from the beam simulation. The main background comes from the prompt ν_e content in the beam and from neutral current interactions where a π^0 electromagnetic activity is misidentified as an electron. These experiments will also search for ν_μ disappearance, by looking at the distortion of the energy spectrum of the ν_μ 's. Such a distortion will be detectable for $\Delta m^2 > 0.1 eV^2$.

Experiment	K2K [II.56]	I216[II.57]	MiniBoone [II.58]
Type	water Čerenkov	Tracking calorimeter and μ catcher	Čerenkov +scintillator
Accelerator	KEK PS	CERN PS	FNAL Booster
Proton energy	12 GeV	19 GeV	8 GeV
ν_e /ν_μ	1%	0.6%	0.3%
Distance	300m/250km	130m/885m	500m$^{(*)}$
Timescale	1999-2002	2001-2002	2001-2002

Table 2.5: *Characteristics of the foreseen medium energy neutrino beams. (*): a second detector at another distance will be added after a year of datataking, if a signal is observed.*

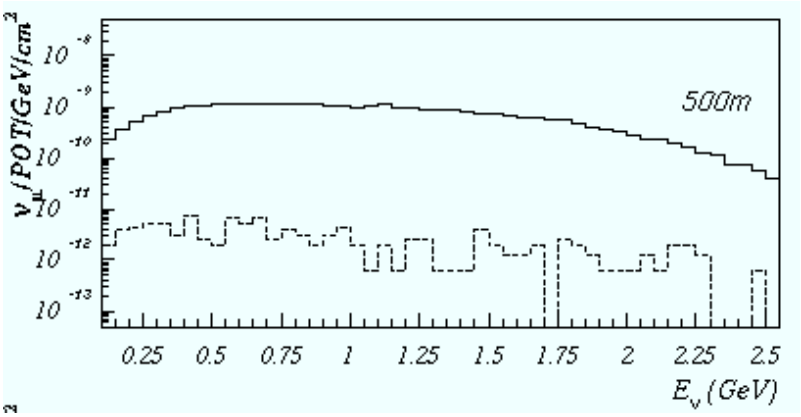

Figure II.9: *FNAL Booster neutrino beam spectrum at 500 m from the source. The solid (dashed) line represents the ν_μ (ν_e) spectrum*

4.2 High Energy beams

Current experimental results

High energy neutrino beams, such as the CERN SPS wide band beam (WBB) described in section III.D and the FNAL WBB, allow to probe oscillation channels involving any two of the three neutrino species :

- The neutrino energy is above threshold for both ν_μ and ν_τ charged current reactions.
- All four flavours ν_μ ,$\bar{\nu}_\mu$,ν_e ,$\bar{\nu}_e$ are contained in the beam in proportions depending on the details of the beam line and the initial proton beam energy. The initial ν_τ and $\bar{\nu}_\tau$ beam content is low ($\sim 3\ \ 10^{-6}\ \nu_\mu$ at the SPS [III.16]). The neutrino spectrum produced at the SPS can be seen in figure III.12.

Neutrino oscillations can be studied by looking for the appearance or the disappearance of a particular neutrino species at a distance from the neutrino production point. The current experimental techniques are described below for the different possible searches :

- ν_e **appearance or disappearance:** Energy deposition patterns (shower shape) or electron identification are used to separate ν_e charged current events from ν_μ neutral current events. The observed ν_e rate is compared with the expectations from beam and detector simulation. This is done for instance by the NOMAD collaboration for the $\nu_\mu \rightarrow \nu_e$ oscillation search.

- ν_τ **appearance:** The signal is the detection of ν_τ CC events followed by the τ^- decay (lifetime=2.91 10^{-13} s [II.63]). It can be detected either by (a) high resolution tracking to resolve the τ decay vertex, or (b) using the transverse momentum unbalance produced by the neutrino(s) escaping in the τ decay . This latter method can be combined with the selection of an exclusive channel as was done in CHARM II were they searched for quasi-elastic production of τ^- followed by the $\tau^- \rightarrow \pi^- \nu_\tau$ one prong decay.

- ν_μ **disappearance:** The ν_μ charged current interaction rate is measured at two distances from the source. The difference in fluxes can be interpreted in terms of $\nu_\mu \rightarrow \nu_e$ or $\nu_\mu \rightarrow \nu_\tau$ oscillation.

- Muon **identification:** The ratio of events with and without muon allows to probe $\nu_\mu \rightarrow \nu_\tau$ and $\nu_\mu \rightarrow \nu_e$ oscillations. Events with a muon come either from ν_μ CC or from ν_τ CC events with the subsequent muonic decay of the τ^- . Events without a muon contain neutral current events, ν_e CC events and ν_τ CC events followed by a non-muonic decay of the τ^- .

Experiment	$< E_\nu >$ GeV	method	$\sin^2(2\theta)$ $\Delta m^2 \rightarrow \infty$	Δm^2 (eV^2) $\sin^2(2\theta) = 1$
		$\nu_e \leftrightarrow \nu_\mu$		
CCFR [II.49]	140	ν_e appearance	0.0018	1.6
NOMAD[II.53]	24	μ identification	0.0018	0.5
E776 [II.44]	1.2	ν_e appearance	0.003	0.075
E734 [II.45]	1.2	ν_e appearance	0.0034	0.43
CHARM II [II.47]	20	ν_e appearance	0.0056	0.85
		$\nu_e \leftrightarrow \nu_\tau$		
BEBC [II.52]	53	ν_e disappearance	0.07	10.
		$\nu_\mu \leftrightarrow \nu_\tau$		
E531 [II.46]	25	ν_τ appearance (a)	0.005	0.9
NOMAD [II.54]	24	ν_τ appearance (b)	0.0015	1
CCFR [II.50]	140	μ identification	0.0081	1.4
CDHS [II.51]	3.	ν_μ disappearance	0.053*	0.26
CHARM II [II.48]	20	ν_τ appearance	0.008	1.5

Table 2.6: *Accelerator results contributing to the present best limits in terms of neutrino oscillation. (*: at $\Delta m^2 = 2.5$ eV^2)*

Table 2.6 shows the results contributing to the best limits so far achieved in terms of the different oscillation channels. The CHORUS and NOMAD experiments took data from 1994 till 1998 at the CERN SPS wide band beam, looking for ν_τ appearance in a beam of ν_μ . The CHORUS experiment is described in detail in chapter III. The NOMAD experiment uses a kinematical method to separate ν_τ from ν_μ -like events [II.55], and a good electron identification identification method to probe $\nu_\mu \rightarrow \nu_e$ oscillations. Figure II.10 shows the present status of exclusion plots and oscillation claims for the $\nu_\mu \rightarrow \nu_\tau$ and $\nu_\mu \rightarrow \nu_e$ oscillation channels in terms of $\sin^2(2\theta)$ and Δm^2 . For clarity, the possible vacuum neutrino oscillation solutions of the solar neutrino problem are not drawn as they lie orders of magnitude lower in Δm^2 than the other experimental results. They can be seen in figure II.3.

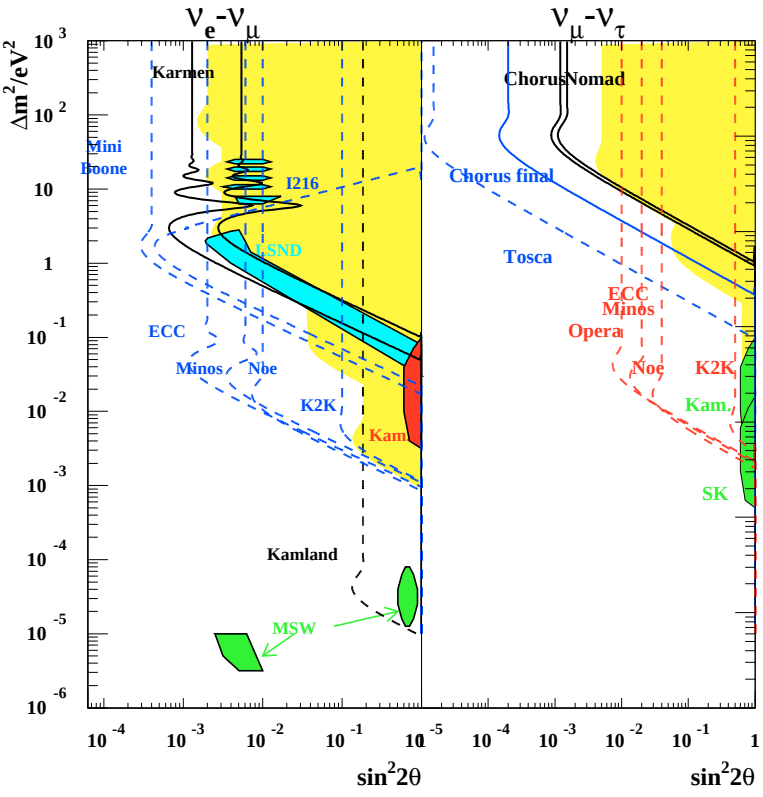

Figure II.10: *Current results of accelerator and reactor neutrino oscillation experiments. The solid lines exclude the areas on their right. The dashed lines represent the sensitivities expected for future experiments. The dark shaded areas represent positive results, the light grey area the excluded region of each plot.*

Future experiments

The next generation of neutrino oscillation searches at accelerators will mainly try and probe the parameter region pointed at by the atmospheric neutrino oscillation claim, by putting neutrino detectors a few hundred kilometres from their production source. The two long-baseline beam projects are :

- Neutrinos to Gran Sasso (NGS) which plan to produce a ≈4-20 GeV neutrino beam at CERN to serve different detectors projects [II.59] to be located 730 km away at Gran Sasso underground laboratory:

  - OPERA: a 700ton emulsion/lead target and tracking system will be used to detect $\nu_\mu \rightarrow \nu_\tau$ oscillations via the observation of the τ decay in a low density gap between emulsion layers. This technique was chosen to minimise the costs of the detector, compared to a full emulsion target. Observing the τ decay in a low density material, however, reduces the background from white star kinks present in the current CHORUS experiment.

  - NOE: a 7kton iron-scintillating fibre calorimeter interleaved with TRD modules. They plan to detect ν_μ disappearance using the CC/NC interaction ratio and to see ν_τ appearance using a kinematic analysis,

  - ICARUS: 4 modules of 600ton liquid argon TPC will be used to detect $\nu_\mu \rightarrow \nu_e$ and $\nu_\mu \rightarrow \nu_\tau$ oscillations in the electron decay channel of the tau, using their very good electron identification capacities.

  - NICE: a 10kton iron calorimeter will detect ν_μ disappearance by measuring the ratio of interaction rates CC/NC. They need a low energy beam (≈4 GeV) and a near detector.

  - AQUA-RICH: a 125 kton water Čerenkov detector to detect ν_μ disappearance using the same techniques as Super-kamiokande. They also hope to detect ν_τ appearance using a kinematic analysis. They also favour a lower energy beam of 7 GeV on average.

  All these experiments but OPERA also plan to detect atmospheric neutrinos and check the Super-Kamiokande signal directly.

- the Main Injector at Fermilab will send neutrinos of about 10 GeV to the Soudan Mine (730 km) where the MINOS [II.60] detector will be located. The MINOS detector is a 10kton magnetised iron target instrumented with streamer tubes. A small near detector will be located at Fermilab. They will use a kinematic analysis to detect ν_τ appearance and will look for ν_μ disappearance by looking at the CC/total interaction ratio and comparing the energy spectra at the close and far detectors. They also plan to add a lead/emulsion sandwich (ECC) detector of several hundred tons as the OPERA detector to the initial MINOS setup.

C Direct neutrino mass measurements.

1 ν_e mass

1.1 β-decay antineutrinos.

The mass of the electron antineutrino has been investigated using the end point of the β-decay of the tritium:

$$^3H \rightarrow {}^3He + e^- + \bar{\nu}_e \qquad (II.6)$$

This reaction has the advantage of a low energy transition Q of 18 keV and that the energy resolution is not degraded by screening effects from other electrons. Limits on the $\bar{\nu}_e$ mass are derived from a fit of the Kurie plot near the end point, looking for departures from linearity of K(E) as a function of E.
Two experiments are currently taking data, trying to accumulate statistics near the end point and face problems with unresolved systematic effects : bump-like structure in the energy spectrum near the end-point [II.62] or dependence of $m^2_{\bar{\nu}_e}$ in function of energy range chosen for the fit [II.61]. The results presented in table 2.7 have not been included in the 1998 Review of Particle Properties [II.5] because of these unknown systematic effects. The Particle Data Group states that an upper limit of m_{ν_e} <10-15 eV is likely as otherwise the two experiments would have seen an effect in spite of their current problems.

Experiment	$m^2_{\bar{\nu}_e}$ (eV^2)	$m_{\bar{\nu}_e}$ (95% C.L.)
Mainz [II.61]	-22 ± 17 ± 14	< 5.6 eV
Troitsk [II.62]	1.5 ± 5.9 ± 3.6	< 3.9 eV

Table 2.7: *Results on the $\bar{\nu}_e$ mass from β-decay .*

1.2 Neutrinos from the SN1987A supernova.

Massive stars (M$\geq 10M_\odot$) have increasing central temperatures and densities as heavier elements are burnt in the fusion process (from H to ^{56}Fe) and settle in the core. When the mass of the core exceeds the Chandrasekar limit ($\approx 1.4M_\odot$), gravitational collapse occurs and the star becomes a neutron star or a black hole. The enormous gravitational energy released in this process is up to 95-99% in the form of neutrinos. The reaction $e^- + p \rightarrow \nu_e + n$ releases an initial neutrino burst which lasts a few hundred milliseconds. As the core collapses, (anti)neutrinos of all species are emitted in a black body fashion by processes such as $e^+ e^- \rightarrow \nu\bar{\nu}$, $n + p \rightarrow n + p + \nu + \bar{\nu}$, etc. Their average energy lies between 10-20 MeV. This second pulse lasts 5-10 seconds. [II.68, II.1]. On February 23rd 1987, a supernova was observed in the Large Magellanic Cloud. Several neutrino detectors which were taking data at the time, collected events from the burst. Results from four experiments claiming to have seen the burst are shown in table 2.8. Anti-neutrinos $\bar{\nu}_e$ are detected via $\bar{\nu}_e + p \rightarrow e^+ + n$ and neutrinos via $\nu_e + e^- \rightarrow \nu_e + e^-$ scattering. The cross section for this latter process is 10 times smaller. The experimental data shown in table 2.8 is either

Experiment		Time of 1st ν event	duration (s)	# of events	E_{thres} (MeV)	$< E_\nu >$ (MeV)
Kamiokande	[II.68]	7:35:35 UT ($\pm$1 min)	12.4	13	7.5	15
IMB	[II.70]	7:35:41 UT ($\pm$ 50 ms)	6	8	$\geq$ 20	32
Baksan	[II.69]	7:36:12 UT ($^{+2}_{-54}$ s)	9.1	5	10	18
		2:52:33 UT ($^{+2}_{-54}$ s)	-	1	10	$\sim$11
LSD	[II.71]	2:52:36 UT ($\pm$2 ms)	7	5	6$\sim$7	11

Table 2.8: *Data from neutrinos observed during the SN1987A stellar collapse.*

inconsistent or two pulses have been observed. This latter option is taken by LSD [II.72], interpreting the first pulse as the collapse into a neutron star, and the second a few hours later from the collapse of the neutron star into a black hole. However, the LSD events are close to their energy threshold, and it is doubted whether these events originate from SN1987A. Using the arrival times of the neutrinos and their energies one could deduce the neutrino mass if the emission time from the supernova had not itself a spread. The results from folding in these theoretical effects with the data from the second pulse yields mass upper limits of [II.1]:

$$m_{\nu_e} \leq \text{5-30 eV}$$

1.3 Double β-decay

Double β-decay can be observed in nuclei for which single β-decay is energetically forbidden. The reaction can be written :

$$^{A}_{Z}X \rightarrow {}^{A}_{Z+2}X + 2e^- + 2\bar{\nu}_e$$

and is a second order process with half-lives of over 10^{20} years. If the neutrino is a Majorana particle ($\nu = \bar{\nu}$ cf. chapter I section D) and is massive, neutrinoless double β-decay becomes possible through the introduction of lepton number violating mass term: $-\frac{m_L}{2}\overline{(\nu_L)}^c \nu_L$+h.c.

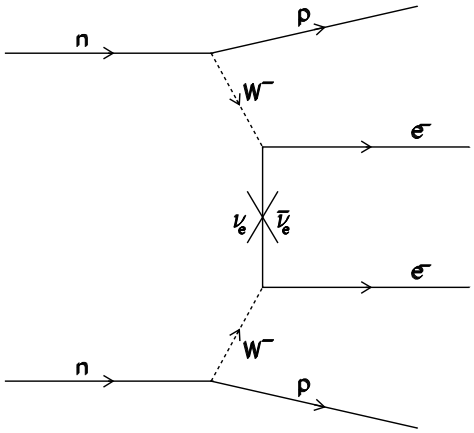

The signature of such an effect is a line in the spectrum of the sum of the energies of the electrons. The non observation of such an effect can therefore translate into a limit on the neutrino mass under the assumption that the neutrino is a Majorana particle. The best limit so far was obtained by the Heidelberg-Moscow experiment [II.64] which uses the double β-decay of ^{76}Ge :

$$m_{\nu_e} \leq 0.65 \text{ eV} \qquad (90\%\text{C.L.})$$

2 ν_μ mass

The best limits for the ν_μ mass are obtained from the decay at rest:

$$\pi^+ \rightarrow \mu^+ + \nu_\mu$$

This is a two-body decay and the sensitivity to the ν_μ mass depends on the precision with which the muon momentum and the pion mass are measured. The current best measurement was done at the PSI and yields :

$$\begin{aligned} m^2_{\nu_\mu} &= -0.016 \pm 0.023 \; MeV^2 \\ \Rightarrow m_{\nu_\mu} &< 170 \text{ keV} \qquad 90\%\text{C.L.} \quad [\text{II.65}] \end{aligned}$$

3 ν_τ mass

The best limits have been obtained by the OPAL [II.67] and ALEPH [II.66] Collaborations studying the decay of the τ^- in 3 or 5 charged pions and neutral particles, using a two-dimensional analysis in the parameter space of missing hadronic mass and energy.

$$\begin{aligned} m_{\nu_\tau} &< 18.2 \text{ MeV/c}^2 \qquad 95\%\text{C.L.} \qquad \text{ALEPH [II.66]} \\ m_{\nu_\tau} &< 29.9 \text{ MeV/c}^2 \qquad 95\%\text{C.L.} \qquad \text{OPAL [II.67]} \end{aligned}$$

References

[II.1] R.D. Peccei, *The physics of neutrinos*, Lectures given at Flavor Symposium, Beijing, PRC, Aug 11-20, 1988.
R.N. Mohapatra and P.B. Pal, *Massive neutrino physics and astrophysics*, World Scientific Publishing,1991.

[II.2] J.R. Primack, *Dark matter and Structure Formation*, astro-ph/9707285 to be published a Chapter 1 of the Proceedings to the Jerusalem Winter School 1996 (Cambridge University Press).

[II.3] P. Chardonnet, *Mystère des neutrinos-mystère de l'univers*,Ecole de Gif-sur-Yvette 24^{th} session 13-18 September 1992, Volume 2, p 69, 1992.

[II.4] S.F. Shandarin, *Massive neutrino and cosmology*, Neutrino physics, p 645, Cambridge University Press, 1991.

[II.5] C. Caso *et al.*,*Eur. Phys. J.* C **3**, 1 (1998), p.124.

[II.6] M. Persic *et al.*, astro-ph/9503051, in Astrophys.Lett.Commun.: Proc. of 3rd Italian Cosmology Meeting.

[II.7] C.L. Bennett *et al.*,*Astrophys. J.* **436**, 423 (1994).

[II.8] J.C. Mather *et al.*,*Astrophys. J.* **420**, 439 (1994).

[II.9] C. Alcock *et al.*(MACHO Coll.),astro-ph/9606165, submitted to *Astrophys. J.*

[II.10] C. Renault *et al.*(EROS Coll.),astro-ph/9612102, submitted to *Astron.Astrophys.*

[II.11] J.N. Bahcall *et al.*,*Rev. Mod. Phys.* **54**, 767 (1982).

[II.12] J.N. Bahcall *et al.*,*Phys. Rev. Lett.* **20**, 1209 (1968).

[II.13] J.N. Bahcall, talk given at the 18^{th} Texas Symposium on Relativistic Astrophysics, Chicago, 1996.

[II.14] J.N. Bahcall *et al.*,*Phys. Lett.* B **433**, 1 (1998).

[II.15] A. Dar, proceedings of the 17^{th} International Conference on neutrino physics and astrophysics (Neutrino 96),p 91 (World Scientific). A. Dar *et al.*, *Astrophys. J.* **468**, 933 (1996).

[II.16] S. Turck-Chièze *et al.*,*Astrophys. J.* **408**, 347 (1993).

[II.17] D. Vignaud *et al.*(GALLEX Coll.), Talk given at the 29th International Conference on High-Energy Physics (ICHEP 98), Vancouver, Canada, 23-29 Jul 1998. talk given at the 18^{th} Texas Symposium on Relativistic Astrophysics, Chicago, 1996.

[II.18] S. Turck-Chièze *et al.*,*Astrophys. J.* **408**, 347 (1993).

[II.19] W. Hampel *et al.*(GALLEX Coll.),*Phys. Lett.* B **388**, 384 (1996).

[II.20] R. Davis Jr. *Nucl. Phys.* B (Proc. Suppl.) **48**, 284 (1996).

[II.21] R. Davis Jr. *et al.*,*Phys. Rev. Lett.* **20**, 1205 (1968).

[II.22] T. Kirsten (GALLEX Coll.),*Nucl. Phys.* B (Proc. Suppl.) **38**, 68 (1995)

[II.23] J.N. Abdurashitov *et al.*(SAGE Coll.), *Phys. Rev. Lett.* **B328**, 234 (1994).

[II.24] Y. Fukuda *et al.*(KAMIOKANDE Coll.),*Phys. Rev. Lett.* **77**, 1683 (1996).

[II.25] Y. Fukuda *et al.*(SUPERKAMIOKANDE Coll.), hep-ex/9812011.

[II.26] Y. Fukuda *et al.*(SUPERKAMIOKANDE Coll.), hep-ex/9812009, submitted to *Phys. Rev. Lett.*.

[II.27] R. Escribano *et al.*, hep-ph/9805238.

[II.28] Y. Fukuda *et al.*(SUPERKAMIOKANDE Coll.),*Phys. Rev. Lett.* **81**, 1562 (1998).

[II.29] T. Kajita *et al.*(SUPERKAMIOKANDE Coll.),hep-ex/98001,talk given at the 18th International Conference on Neutrino Physics and Astrophysics, Takayama, Japan, 4-9 Jun 1998.

[II.30] K.S. Hirata *et al.*(KAMIOKANDE Coll.),*Phys. Lett.* B **280**, 146 (1992). Y. Fukuda *et al.*(KAMIOKANDE Coll.),*Phys. Lett.* B **335**, 237 (1994).

[II.31] D. Casper *et al.*(IMB Coll.),*Phys. Rev. Lett.* **66**, 2561 (1991).
R. Becker-Szendy *et al.*(IMB Coll.),*Phys. Rev.* D **46**, 3720 (1992).

[II.32] K. Daum *et al.*(FREJUS Coll.),*Z. Phys.* C **66**, 417 (1995).

[II.33] M. Aglietta *et al.*,*Europhys. Lett.* **8**, 611 (1989).

[II.34] W.W.M. Allison *et al.*,*Phys. Lett.* B **391**, 491 (1997).

[II.35] T. Montaruli (MACRO Coll.) hep-ex/9810017, to appear in DARK98 Conference proceedings, Heidelberg, July 1998.

[II.36] D. Saltzberg, *Phys. Lett.* B **355**, 499 (1995)

[II.37] G. Zacek *et al.*,*Phys. Rev.* D **34**, 2621 (1986).

[II.38] B. Achkar *et al.*,*Phys. Lett.* B **374**, 243 (1996).

[II.39] M. Apollonio *et al.*,*JETP Lett.* **59**, 364 (1994).

[II.40] G.S. Vidyakin *et al.*,*Phys. Lett.* B **420**, 397 (1998).

[II.41] C. Athanassopoulos *et al.*(LSND Coll.),*Phys. Rev. Lett.* **77**, 3082 (1996) and *Phys. Rev.* C **54**, 2685 (1996)

[II.42] C. Athanassopoulos *et al.*(LSND Coll.),*Phys. Rev. Lett.* **81**, 31774 (1998) and submitted to *Phys. Rev.* C.

[II.43] K. Eitel (KARMEN Coll.),talk given at the XXXIInd Rencontres de Moriond, Les Arcs, March 15-22,1997.

[II.44] L. Borodovsky *et al.*(E776 Coll.),*Phys. Rev. Lett.* **68**, 274 (1992).

[II.45] L.A. Ahrens *et al.*(E574 Coll.),*Phys. Rev.* D **31**, 2732 (1985).

[II.46] N. Ushida *et al.*(E531 Coll.) ,*Phys. Rev. Lett.* **57**, 2897 (1986).

[II.47] P. Vilain *et al.*(CHARM II Coll.),*Z. Phys.* C **64**, 539 (1994).

[II.48] M. Gruwé *et al.*(CHARM II Coll.),*Phys. Lett.* B **309**, 463 (1993).

[II.49] A. Romosan *et al.*(CCFR Coll.),*Phys. Rev. Lett.* **78**, 2912 (1997).

[II.50] K.S. McFarland *et al.*(CCFR Coll.),*Phys. Rev. Lett.* **75**, 3993 (1995).

[II.51] F. Dydak *et al.*(CDHS Coll.),*Phys. Lett.* B **134**, 281 (1984).

[II.52] O. Erriquez *et al.*(BEBC),*Phys. Lett.* B **102**, 73 (1981).

[II.53] A . De Santo (NOMAD Coll.), talk given at the XXXIInd Rencontres de Moriond, Les Arcs, March 15-22,1997.

[II.54] D. Autiero, (NOMAD Coll.),Talk given at 29th International Conference on High-Energy Physics, Vancouver,Canada, 23-29 Jul 1998

[II.55] P.Astier *et al.*(NOMAD Coll.), CERN-SPSLC/91-21 (1991), SPSC/P261.

[II.56] Y. Oyama (K2K Coll.), Talk given at the YITP Workshop on Flavor Physics, Kyoto, Japan, 28-30 Jan 1998. hep-ex/980314.

[II.57] Letter Of Intent: Search for $\nu_\mu \rightarrow \nu_e$ oscillations at the CERN PS, CERN-SPSC/97-21, SPSC/I 216.

[II.58] A Proposal for an Experiment to Measure $\nu_\mu \rightarrow \nu_e$ Oscillations and ν_μ Disappearance at the Fermilab Booster: BooNE,Fermilab-Proposal-898.

[II.59] F.Pietropaolo talk given at the 18th International Conference on Neutrino Physics and Astrophysics, Takayama, Japan, 4-9 Jun 1998.

[II.60] S.Wojcicki, talk given at the 18th International Conference on Neutrino Physics and Astrophysics, Takayama, Japan, 4-9 Jun 1998.

[II.61] J. Bonn, proceedings of the 17^{th} International Conference on neutrino physics and astrophysics (Neutrino 96),p 259, (World Scientific).
C. Weinheimer *et al.*,*Phys. Lett.* B **300**, 210 (1993).

[II.62] V.M. Lobashev, proceedings of the 17^{th} International Conference on neutrino physics and astrophysics (Neutrino 96), p 264, (World Scientific).
A.I Belesev *et al.*,*Phys. Lett.* B **350**, 263 (1995).

[II.63] R.M. Barnett et al.,*Phys. Rev.* D **54**, 1 (1996)

[II.64] H. Klapdor-Kleingrothaus,proceedings of the 17^{th} International Conference on neutrino physics and astrophysics (Neutrino 96),p 317, (World Scientific).
A. Balysh *et al.*,*Phys. Lett.* B **356**, 450 (1995).

[II.65] K. Assamagan *et al.*,*Phys. Rev.* D **53**, 6065 (1996).

[II.66] R. Barate *et al.*(ALEPH Coll.) *Eur. Phys. J.* C **2**, 395 (1998).

[II.67] G. Alexander *et al.*(OPAL Coll.), *Z. Phys.* C **72**, 231 (1996).

[II.68] K.S. Hirata *et al.*(KAMIOKANDE Coll.),*Phys. Rev.* D **38**, 448 (1988).

[II.69] E.N. Alexeyev *et al.*(Baksan Coll.),*Phys. Lett.* B **205**, 209 (1988).

[II.70] R.M. Bionta *et al.*(IMB Coll.),*Phys. Rev. Lett.* **58**, 1494 (1987).

[II.71] M. Aglietta *et al.*(LSD group),*Europhys. Lett.* **3**, 1315 (1987).

[II.72] M. Aglietta *et al.*(LSD group),*Europhys. Lett.* **3**, 1321 (1987).

Chapter III The CHORUS Experiment

The CHORUS experiment searches for $\nu_\mu \rightarrow \nu_\tau$ oscillations using a neutrino beam mainly composed of ν_μ . The detector is placed at 600 m from the average neutrino production point. If oscillations take place, ν_τ neutrinos can be detected through their charged current (CC) interactions in a nuclear emulsion target, followed by the typical topology of the decay of the τ^- lepton. During run I, 120 000 CC ν_μ interactions have been collected in 1994 and 200 000 in 1995 after which the target was removed and developed. Run II started in 1996 with new emulsion and collected about 500 000 CC events.
This chapter describes the expected signal and backgrounds in sections A and B. The detector and the beam are described in sections C and D.

A The signal.

CHORUS wants to detect ν_τ CC interactions using the specific topology of the subsequent decay of the τ^- lepton. The τ^- lifetime is 2.91 10^{-13} s; nuclear emulsion alone is capable of resolving the few hundred μm flight length of the τ^- before its decay. The decay channels considered are the following:

$$\tau^- \rightarrow \begin{cases} \mu^- \bar{\nu}_\mu \nu_\tau & BR = (17.37 \pm 0.09)\% \\ \mathrm{e}^- \bar{\nu}_\mathrm{e} \nu_\tau & BR = (17.81 \pm 0.07)\% \\ \mathrm{h}^- (\mathrm{n}\pi^0) \nu_\tau & BR = (49.52 \pm 0.16)\% \end{cases} \quad \text{[II.5]}$$

For the three decay channels, the invisibility of the final-state neutrino(s) gives rise to a "kink" topology in the emulsion as shown in figure III.2. Figure III.1 shows the diagrams and the topology of ν_μ CC and NC interactions. The undetected neutrino(s) will create an unbalance in the total measured transverse momentum with respect to the neutrino beam direction.

B The background.

If oscillations take place at the level of the present limit set by the E531 experiment [II.46], we are searching for a few, at most 120 ν_τ induced events among $\approx$ 10^6 ν_μ interactions. This section reviews several processes which, by their topology, could fake τ^- candidates.

1 Prompt ν_τ production.

D_s mesons are produced in a small fraction f of the inelastic interactions of protons on beryllium (f=3.2 10^{-4}) and iron (f=5.6 10^{-4}) nuclei in the target and in the dump of the neutrino beam line, respectively [III.16]. Their decay into τ leptons and the subsequent decay of the τ's give rise to an irreducible prompt ν_τ background. The number of ν_τ CC

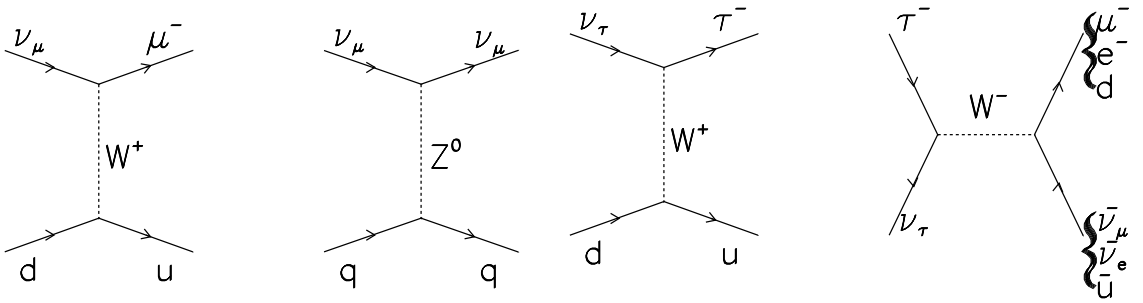

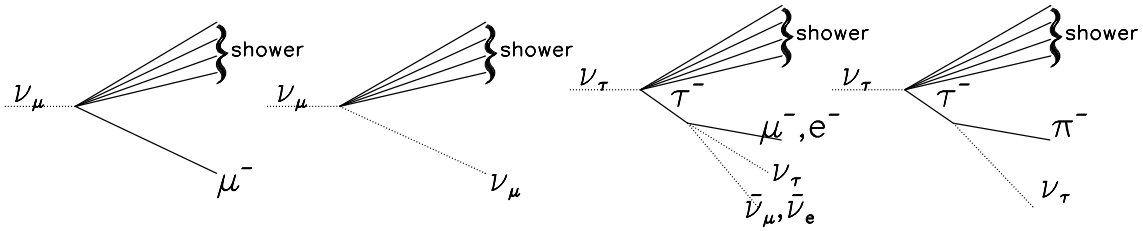

Figure III.1: *Diagrams and topologies of the ν_μ CC and NC interactions.*

Figure III.2: *Diagrams and topologies of the ν_τ CC interaction with the subsequent decay of the τ^- .*

interactions to be expected from this source in the emulsion target was estimated to be $\sim 3.3\ \ 10^{-6}$ per ν_μ CC interactions.

2 Charm decays.

(Anti)charm is produced in $\sim$5 % of the (anti)neutrino CC interactions [III.1] via the processes involving $s, \bar{s}$ sea quarks shown in figure III.3. Similar processes incolving d and $\bar{d}$ quarks also contribte with an extra factor $\sim \sin\theta_C$ at the W quark vertex, θ_C being the Cabbibo angle. About half of the produced charm quarks will give rise to a charged charmed particle. The masses and lifetimes of these particles are similar to that of the τ lepton, so that their one and three prong decays can fake a τ decay. A large fraction of these events can be rejected by the detection of the primary muon or electron coming from the CC interaction. The remaining positive charmed particles decays can be further rejected by the identification of the charge of its decay products. Negative charmed particles are created in antineutrino CC interactions. The small ($\sim$6%) contamination of the SPS beam in antineutrinos, allows to keep low the background due to their decays. Further reduction of this background can be achieved using kinematical cuts: in a ν_τ CC interaction, the transverse momentum (P_t) of the produced τ^- lepton with respect to the beam is back to back to the hadron shower P_t while this is not the case in ν_μ CC as the charmed particle is part of the shower.
Associated charm production in neutrino or antineutrino NC(CC) interactions has been measured to be $< 0.12\%$ ($<3\%$) [III.1]. The background that would arise from their decays is rejected by the same methods as for the single charm events where the primary lepton has not been identified. It can be further suppressed by requiring the absence of a second decay topology near the primary vertex.

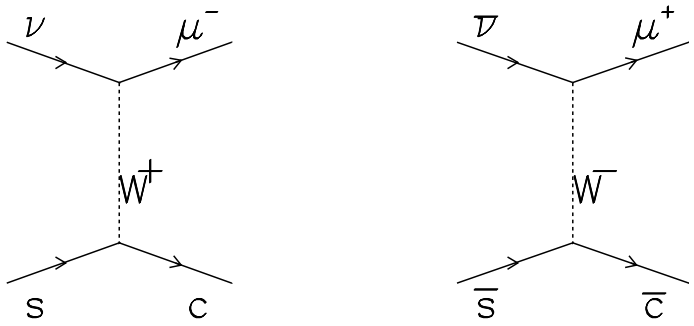

Figure III.3: *Feynman diagrams for charm and anti-charm production in neutrino CC interactions.*

3 Kaon and pion decays.

Charged kaons and pions are created in abundance in neutrino interactions. Their decays can reproduce the one-prong decay topology of a τ. However, as their mean lifetime is five orders of magnitude longer than the τ's, a cut on the decay length efficiently rejects these events. Moreover, the maximum allowed transverse momentum of their decay products with respect to the parent particle is $\simeq$250 MeV/c. A minimum cut on the transverse momentum of the decay products with respect to a τ^- candidate eliminates the rest of these events.

4 White kinks.

Hadrons produced in neutrino interactions can scatter on a nucleus within the allowed decay path without any visible recoil, blob or Auger electron. This process, called "white star kink", leaves in the emulsion a signature identical to that of a single prong hadronic decay of the τ, such that it constitutes background when the scattered pion is negative. The white star kink mean free path for pions (λ_{WK}) is poorly known [III.3] as few experimental results are available. A KEK measurement using 4 GeV/c pions, yields mean free path $\lambda_{WK} \simeq 50$ m for a transverse momentum p_t >200 MeV/c and $\lambda_{WK} \simeq 370$ m for p_t >300 MeV/c. This extrapolates to less than 1 background event for 35000 located ν_μ NC events in 4 years of CHORUS running. Further measurement will be done in the CHORUS emulsion using pion tracks coming from neutrino CC interactions. This will allow to measure the momentum dependence of this process and the p_t distribution of the scattered pions.
The coherent A^1 production reactions π^- N $\rightarrow \pi^- \pi^0 \pi^0$ N* and π^- N $\rightarrow \pi^- \pi^- \pi^+$ N* constitute backgrounds to the $\tau^- \rightarrow \pi^-$ (nπ^0)ν_τ and $\tau^- \rightarrow \pi^- \pi^- \pi^+$ (nπ^0)ν_τ decays respectively. The one-prong decay is indistinguishable from the white star kink and therefore already accounted for in the KEK measurement. From a simulation based on the measured A^1 coherent production cross-sections on different nuclei, the probability P for π^- with momenta in the range 1 to 15 GeV/c to interact coherently and to produce a kink angle >10 mrad with a p_t >300 MeV/c is P$\simeq 5\ 10^{-6}$ [III.3].

C The Detector.

The CHORUS detector is composed of a nuclear emulsion target, instrumented with emulsion and fibre tracking planes, followed by a magnetic spectrometer, a calorimeter and a muon spectrometer as shown in figure III.4. A complete description of the CHORUS detector and of its calibration can be found in [III.4]. The reference frame of the detector is defined in the following way: it is a right-handed coordinate system with its origin at the centre of the target, the X axis is horizontal along the beam direction and the Z axis vertical with the positive direction pointing upwards.

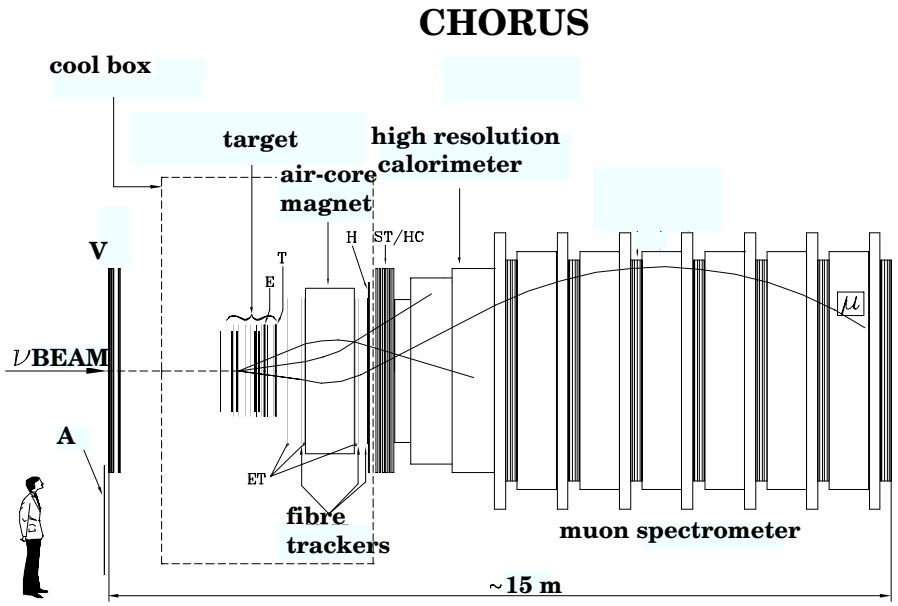

Figure III.4: *Schematic view of the CHORUS detector.*

1 The target area.

The target is made out of 770kg of nuclear emulsion, allowing to see the decay topology of the τ^- with a spatial resolution of 1 μm. The target is divided in 2 modules each composed out of 2 stacks of emulsion separated by a set of 3 interface emulsion tracker sheets and 4 fibre tracking planes, and followed by another set of interface emulsion sheets and 12 fibre tracking planes. Figure III.5 shows one module of the target region.

Each emulsion stack has an area of 1.44×1.44 m^2 and is divided in 8 sectors of 36×71 cm^2. Each sector is composed of 36 plates, which are made of a 90 μm thick tri-acetate cellulose backing on each side of which a 350 μm layer of nuclear emulsion is deposited. The total thickness of a stack is 2.8 cm. The interface sheets have the same lateral dimensions as the target, they are composed of a 0.8 mm thick acrylic plate coated on both sides with a 100 μm thick emulsion layer. They are placed one directly against the target emulsion,

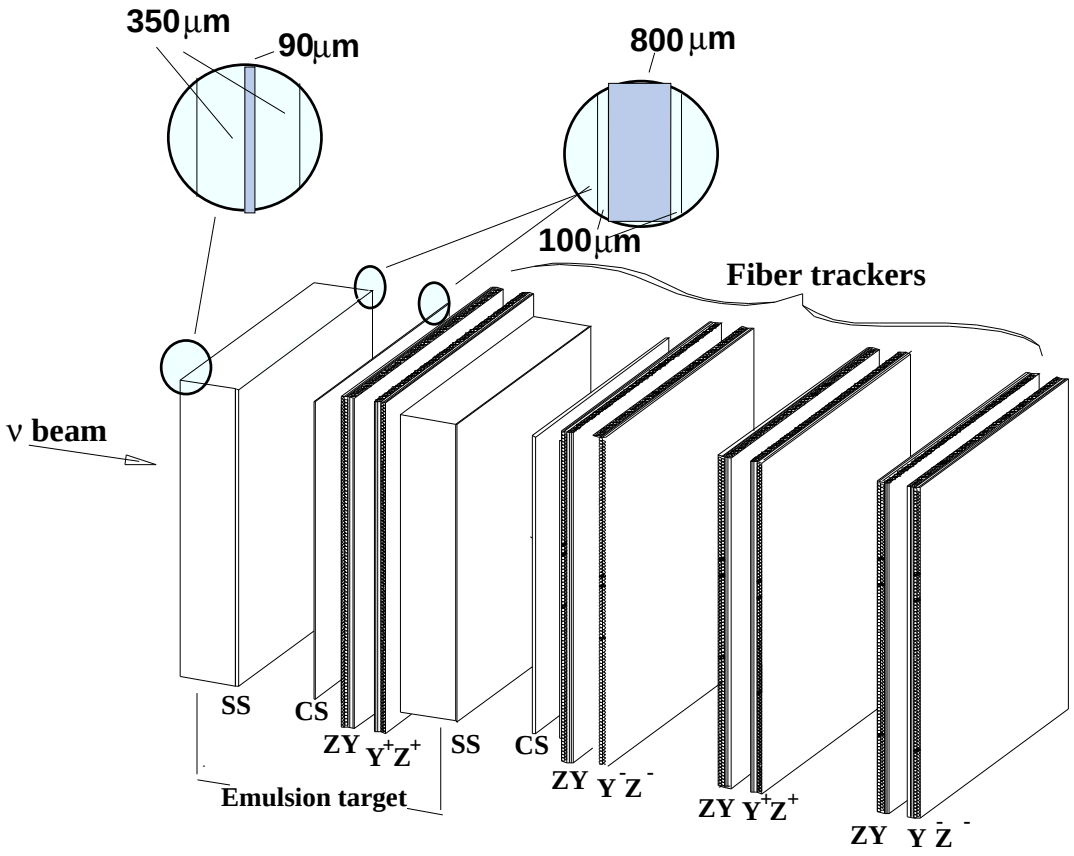

Figure III.5: *Schematics of one module of the target region. The different fibre orientations are marked by Y,Z Y^-,Z^- and Y^+,Z^+. The interface sheets are marked CS and SS.*

called special sheet (SS) and the other two, called changeable sheets (CS) on both sides of a 1 cm thick honeycomb panel in front of the first fibre tracking plane downstream of the emulsion stack *

The role of the target fibre trackers is to reconstruct the neutrino events and to predict the points at which charged particles from a neutrino interaction exit the nearest changeable sheet. They will be described in section IV.B. The target region of the detector as well as the magnetic spectrometer are kept at 5^oC in a refrigerated box (cool-box) to avoid aging of the scintillating fibres and fading of the emulsions.

2 The magnetic spectrometer.

The target region is followed by a magnetic spectrometer composed of 3 fibre tracking modules, streamer tube planes (4 in 1994, 6 in 1995 and replaced in September 1996 by Honeycomb planes) and a toroidal pulsed air-core magnet [III.5] of hexagonal shape. The

*The CS were changed every 3 weeks in 1994 to minimise the background due to muons from the nearby X7 test beam. In later years, the usage of X7 was kept lower and the CS changes less frequent.

fibre tracking modules are called Diamond Trackers (DT) and will be described in detail in section IV.C. One DT module is placed upstream and two downstream of the air-core magnet, followed by the streamer tube planes (TST). The TST planes are identical to the streamer planes used in the muon spectrometer (cf section 4). The purpose of this magnetic spectrometer is to determine the charge and the momentum of charged particles upstream of the calorimeter. The magnet, shown in figure III.6, is divided in 6 triangles, in which a uniform magnetic field of 0.118 Tesla is obtained, orthogonal to the beam direction, and parallel to the outer side of each triangle. There is no radial dependence of the field. The magnet is pulsed according to the accelerator cycle to minimise the heat dissipation in the cool-box from which the warmed up air is evacuated. The width of the magnet varies

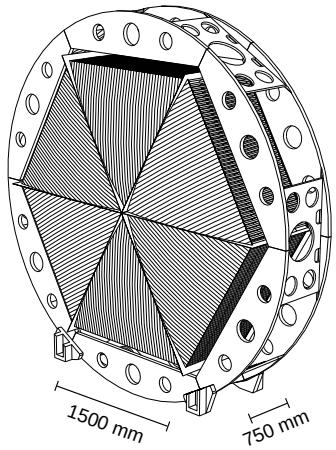

Figure III.6: *Schematic view of the air-core magnet*

between 75 and 85 cm as the front and back sides of each triangle are bulged. This shape was chosen to minimise mechanical stress due to the pulsing of the magnetic field.
In 1996, three emulsion trackers (ET) have been added at the level of the trigger plane T1, DT1 and DT2 as shown in figure IV.6. Using track predictions from the fibre trackers, they will allow a more precise determination of the momentum of hadrons daughters in candidate τ^- decays.

3 The calorimeter.

The main role of the lead-scintillator calorimeter placed downstream of the magnetic spectrometer is the measurement of the energy deposited by pions and electrons, to confirm the momentum measured in the magnetic spectrometer and to differentiate electrons, pions and muons. The calorimeter is composed of 3 parts: an electromagnetic calorimeter (EM) and two hadronic calorimeter parts (HAD1 and HAD2). EM and HAD1 use the so-called "spaghetti" technique [III.6] which consists in embedding 1 mm diameter scintillating fibres in a lead matrix, with a volume ratio 4:1 to achieve compensation. HAD2 is a lead/scintillator-strip sandwich in the same proportions. The total depth corresponds to 144 radiation lengths and 5.2 interaction lengths, such that 99% of the showers produced by a 5 GeV/c pion are contained (about 90% of the hadrons produced in the target

have a momentum less than 5 GeV/c). More details on the construction and tests of the calorimeter can be found in [III.7]. The energy dependence of the response to electrons

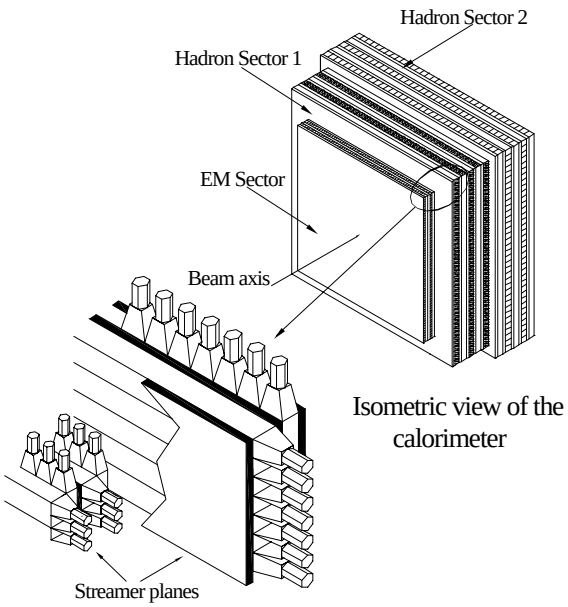

Figure III.7: *Schematic view of the calorimeter.*

and pions in the ranges 2.5 to 10 GeV and 3 to 20 GeV respectively was studied [III.8] using the test beam X7. The electromagnetic response is well fitted by the function :

$$\frac{\sigma(E)}{E} = \frac{(13.8 \pm 0.9)\%}{\sqrt{E(GeV)}} + (-0.2 \pm 0.4)\%$$

The energy dependence of the hadronic resolution was measured to be linear within 2% and can be parametrised as:

$$\frac{\sigma(E)}{E} = \frac{(32.3 \pm 2.4)\%}{\sqrt{E(GeV)}} + (1.4 \pm 0.7)\%$$

These results agree with the Monte Carlo predictions. This test also yielded an estimate on the non-uniformity of the electromagnetic and hadronic responses, found to be of the order of $\pm 5\%$ and $\pm 2\%$ respectively. More details on the performances of the calorimeter can be found in [III.9].
Limited streamer tube planes are located in between the calorimeter planes to allow reconstruction of the muon tracks.

4 The muon spectrometer.

The role of the muon spectrometer is to identify muons and to determine their trajectory, momentum and charge. The spectrometer is located behind the calorimeter the 5.2

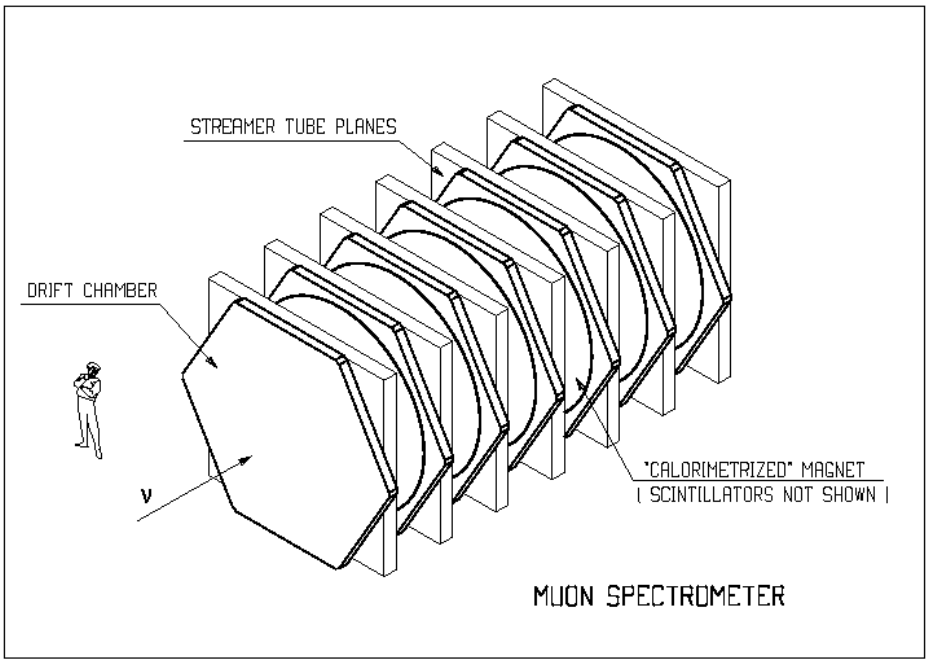

Figure III.8: *Schematic view of muon spectrometer.*

hadronic interaction lengths of which filter nearly all the particles produced by neutrino interactions in the emulsion target, except muons with momentum higher than $\sim$ 1.5 GeV/c. As displayed in figure III.8, the spectrometer is constructed from six magnetised iron toroid modules instrumented with scintillator planes and tracking detectors (drift chambers and limited streamer tubes). The fast signals from the scintillator planes are used for triggering and provide a measurement of the leakage of hadronic showers from the back of the calorimeter. The field in the magnets is nearly symmetric in azimuthal angle and varies by 25% along the radius. The field integral is approximately 0.85 Tesla·m per magnet [III.10]. Tracking detectors are mounted in each of the seven gaps between and around the magnets; one drift chamber [III.12] followed by eight slightly improved limited streamer tube planes of the former CHARM II calorimeter [III.11]. The drift chambers are composed of 3 drift planes oriented at 60° with respect to each other, and are characterised by a hit resolution of about 1 mm and an efficiency better than 99%. The streamer tube planes provide track segments which resolve the 17% left-right ambiguities unresolved by the drift chamber. The hit efficiency and resolution are (80 $\pm$ 2)% and 2.4 mm (rms) per plane, respectively. The momentum resolution of the muon spectrometer is about 19% at 71 GeV/c, as measured with test beam muons. At lower momenta it is determined with the help of a Monte Carlo simulation and the results are shown in figure III.9. Details on the track finding and fitting can be found in [III.13].

5 The trigger system.

The main role of the trigger system is to select neutrino interactions in the emulsion target and to reject background from cosmic rays, beam muons and neutrino interactions outside the target. Scintillator hodoscopes called E, T, H, V and A, as shown in figure

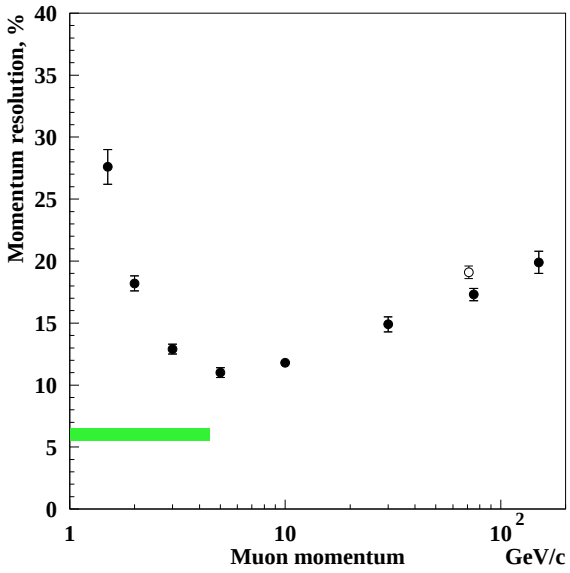

Figure III.9: *Momentum resolution of the muon spectrometer as a function of the incident momentum. Full dots: Monte Carlo events, the open dot at 71 GeV/c: test beam muons. The shaded band corresponds to muons for which the momentum is measured by range as they stop in the spectrometer.*

III.10, are used for this purpose. A neutrino trigger in the target region is defined by a hit coincidence in E (from 1995 onwards), T and H consistent with a particle trajectory with $\tan\theta < 0.25$ with respect to the neutrino beam axis. A veto is formed by any combination of a counter hit in the veto hodoscopes (V and A) and a hit in T, with a 2 ns timing resolution (FWHM). The good timing resolution as well as the large distance of the veto plane to the target allows to avoid vetoes due to backscattering of particles coming from neutrino interactions in the target. The measured neutrino interaction rate in the target area is 0.5 events per 10^{13} protons on the SPS target corresponding to an effective neutrino target mass of 1600 kg (2000 kg in 1994). The fraction of those events originating in the emulsion target is 50% (40% in 1994). A trigger efficiency of 99% ($> 90\%$) was estimated from Monte Carlo simulation for ν_μ CC (NC) events in the emulsion target. Neutrino events also originate in the calorimeter and muon spectrometer. Typically five of these are also selected per neutrino spill for calibration and beam measurement.

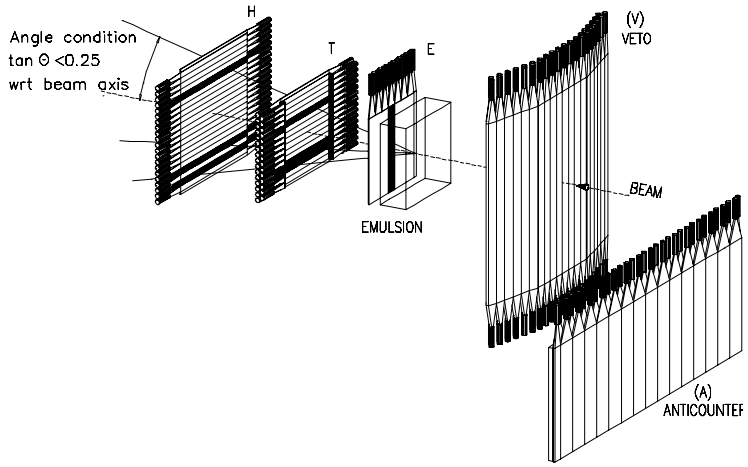

Figure III.10: *Schematic view of the trigger hodoscopes*

D The Beam

The West Area Neutrino Facility (WANF) [III.14] of the CERN SPS provides a beam of ν_μ with energies mostly above threshold for ν_τ CC interactions. Protons are accelerated by the SPS to an energy of 450 GeV with a cycle of 14.4 s. They are extracted in two 6 ms long spills separated in time by 2.7 s, and sent onto a beryllium target, producing mainly pions and kaons. A typical spill contains between 1 to 1.5 10^{13} protons, the intensity improving steadily between 1994 and 1996. Neutrinos originate from the decays in flight of these mesons, mostly in a 290 m long vacuum tunnel. The time structure of the SPS cycle is shown in figure III.11.

Positive (negative) mesons are focused (defocused) by two magnetic lenses: the horn and the reflector which are placed respectively at 20 and 90 m downstream of the target. The space between the horn and the reflector is filled with helium to reduce the absorption of the mesons before they could decay. The neutrino beam has an upward slope of 42 mrad. The detector parts were centred along this slope, however, every part is placed vertically. A full analysis of the beam from flux monitors in the beam line itself and from neutrino events in the CHORUS detector is underway. The coming results of the SPY experiment [III.17] in terms of pion and kaon multiplicities in hadronic interactions will also be implemented in the beam analysis. Preliminary knowledge of the beam can be inferred from the CHARM II measurement [III.15], scaling the results for the CHORUS detector position (60 m more upstream that the CHARM II detector) and width, using a Monte Carlo simulation. Table 3.1 shows the abundances and mean energies of all neutrino species obtained by this method. The estimated event rate in CHORUS is 2.1×10^{-14} CC

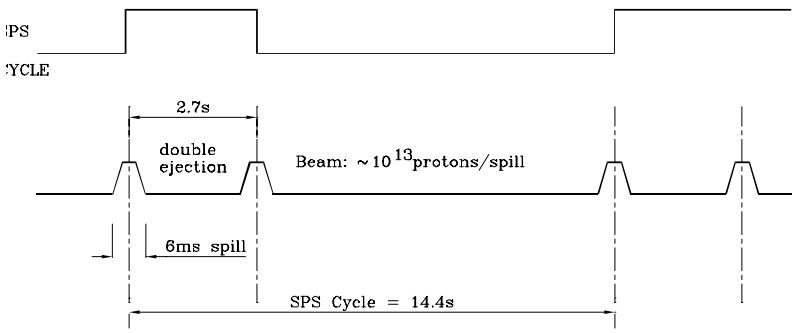

Figure III.11: *The timing structure of the CERN SPS cycle and the Wide-Band Neutrino Beam.*

events per proton. Figure III.12 shows the energy spectra of the different components of the neutrino beam intercepted by the CHORUS emulsions (1.44 $\times$ 1.44 m^2 area).

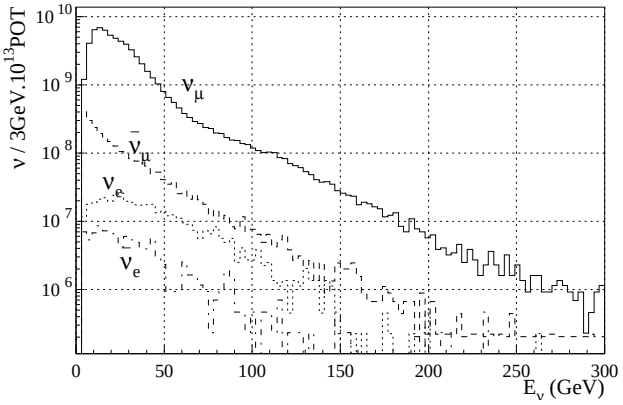

Figure III.12: *Energy spectra of the different neutrino components in the Wide Band neutrino Beam at the location of the CHORUS emulsion target (transverse dimensions 1.44 $\times$ 1.44 m^2), derived from the neutrino beam simulations.*

The ν_τ contamination of the beam, the irreducible background for the $\nu_\mu \rightarrow \nu_\tau$ oscillation search, is expected to be at the (negligible) level of ν_τCC/ν_μCC $\sim 3.3 \times 10^{-6}$ [III.16], corresponding to $\sim$ 0.1 background events for the 4 years of CHORUS data taking.

neutrino species	**relat. abundance**	$<$ E $>$ **(GeV)**
ν_μ	100 %	26.9
$\bar{\nu_\mu}$	5.6 %	21.7
ν_e	0.7 %	47.9
$\bar{\nu_e}$	0.17 %	35.3

Table 3.1: *The relative composition of the CERN Wide Band Neutrino Beam at the CHORUS experiment.*

References

[III.1] N. Ushida *et al.*(E531 Coll.),*Phys. Lett.* B **206**, 375 (1988).

[III.2] M. de Jong *et al.*(CHORUS Coll.), CERN-PPE/93-131.

[III.3] R.Ferreira and H.Wong, CHORUS Internal Report 18/04/96.

[III.4] E.Eskut *et al.*(CHORUS Coll.),*Nucl. Instrum. Methods* A **401**, 7 (1997).

[III.5] F. Bergsma *et al.*, *Nucl. Instrum. Methods* **A357**, 243 (1994).

[III.6] D. Acosta *et al.*, *Nucl. Instrum. Methods* **A308**, 481 (1991).

[III.7] S. Buontempo *et al.*, *Nucl. Instrum. Methods* **A349**, 70 (1994).

[III.8] L. Gatignon, CERN SL/Note 95-72 (EA) (1995).

[III.9] E. Di Capua *et al.*, *Nucl. Instrum. Methods* **A378**, 221 (1996).

[III.10] H. Abramovitz *et al.*(CDHS Coll.), *Nucl. Instrum. Methods* **180**, 429 (1981)
A. Blondel *et al.*(CDHS Coll.), *Z. Phys.* C **45**, 361 (1990).

[III.11] J. P. Dewulf *et al.*(CHARM II Coll.), *Nucl. Instrum. Methods* **A252**, 443 (1986)
J. P. Dewulf *et al.*(CHARM II Coll.), *Nucl. Instrum. Methods* **A263**, 109 (1988)
D. Geiregat *et al.*(CHARM II Coll.), *Nucl. Instrum. Methods* **A325**, 92 (1993)
T. Bauche, Ph. D. Thesis, University of Hamburg (1988).

[III.12] G. Marel *et al.*, *Nucl. Instrum. Methods* **141**, 43 (1977)
M. Holder *et al.*(CDHS Coll.), *Nucl. Instrum. Methods* **148**, 235 (1978).

[III.13] T. Patzak, Ph. D. Dissertation, Humboldt University of Berlin (1995).

[III.14] E. Heijne, CERN Yellow Report 83-06 (1983);
G. Acquistapace *et al.*, CERN Preprint, CERN-ECP/95-14 (1995).

[III.15] D. Geiregat *et al.*(CHARM II Coll.), *Phys. Lett.* B **232**, 539 (1989);
P. Vilain *et al.*(CHARM II Coll.), *Phys. Lett.* B **281**, 159 (1992).

[III.16] B. Van de Vyver,*Nucl. Instrum. Methods* **A385**, 91 (1997)
M. C. Gonzalez-Garcia and J. J. Gomez-Cadenas, *Phys. Rev.* D **55**, 1297 (1997).

[III.17] G. Ambrosini *et al.*(SPY Coll.),CERN-SPSLC-96-01,1996.

Chapter IV The CHORUS fibre trackers

A The readout.

1 Design.

The full CHORUS fibre tracking system [IV.1] contains 1.2 million scintillating plastic fibres of 500 μm diameter, bundled into 8 cm wide staggered 7-layer ribbons [IV.2] as shown in figure IV.1. Each ribbon is sputtered on one end with aluminium insuring a

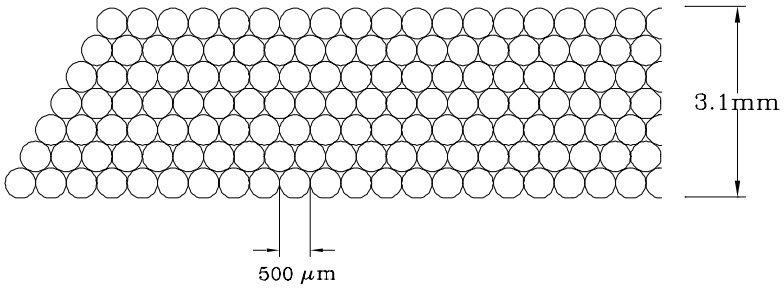

Figure IV.1: *View of the fibre staggering in a ribbon.*

reflectivity of 80%. The other end of the ribbons is coupled as shown in figure IV.3 in groups of 16 to 58 optoelectronic chains such as the one shown in figure IV.2.

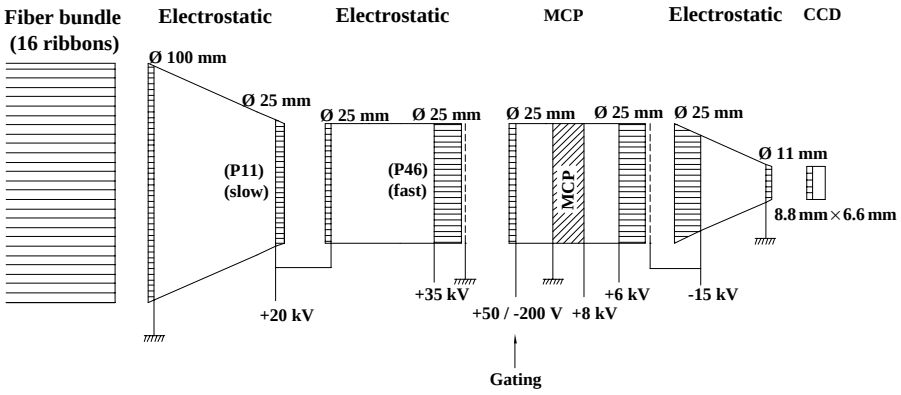

Figure IV.2: *Schematic view of an optoelectronic chain and CCD (charge-coupled device) camera for the CHORUS fibre tracker readout.*

Each chain contains four image intensifiers (II) and is readout by a CCD* camera. The chains and the cameras are shielded from the surrounding magnetic field.
The detection efficiency for a photon entering the optoelectronic chain is 18%, determined by the quantum efficiency of the first demagnifying stage. The purpose of the second stage is to increase the gain before the third stage which is a gateable MCP (micro-channel plate). The length of the gate is 20 μs maximum, to minimise the background. The fourth stage demagnifies the image to the size of the CCD. The total demagnification factor is 0.11 and the net gain for the whole optoelectronic chain is between 10^4 and 10^5 . More details on the optoelectronic chains can be found in [IV.3].

The CCD is equipped with a live and a memory zone. The readout of one image takes 20 ms, much longer than the neutrino spill. However, the presence of the 2 zones allows to take 2 events per 4 ms spill. The first event is transferred from live to memory zone in 125 μs. This configuration is sufficient for our purpose, considering that the neutrino trigger rate is of 0.5 event for a typical spill of 10^{13} protons on the beryllium target. Each CCD zone contains 550$\times$288 pixels. In the detector space, one pixel represents 145 μm in the transverse direction times 209 μm in the beam direction. The CCD signals are digitised and compressed, this operation takes 1 second per event which ensures that the system is ready for the next neutrino spill (at least 2.5 s later). The contribution to the dead-time of the data acquisition is of 6%, equally due to the two event limit and the transfer time. More details on the cameras and their readout can be found in [IV.4].

2 Calibration and performance.

2.1 "Fiducial" data

The electric field in the intensifiers creates a distortion of the image. This distortion is measured to ensure correct mapping of the CCD pixels to the input window of the II. As the field configuration in the chains may take up to a day to stabilise every time they are switched on, the distortion is continuously monitored during data taking. To measure the distortion, spacers have been added around and between groups of four fibre ribbons at the input window. Each of the five spacers contains a row of 9 clear 100 μm diameter fibres (called "fiducials") coupled to a LED pulser module. The intensity and the length of the LED pulse can be regulated via the data acquisition system. Figure IV.4 shows the CCD image of the fiducial fibres along with the approximate ribbon shapes. The exact position and dimensions of the fibre bundles was measured by photographic contact print before assembly with the optoelectronic chains. The parameters used to perform the distortion correction are fitted to the following expression using the contact print data and the measured positions of the image of the fiducial fibres on the CCD :

$$R_{ccd} = A R_{II} \left(1 + B \left(R_{II}/R_0\right)^{\alpha}\right)$$

where R_{ccd} (R_{II}) is the radial position of the fibre from the optical centre of the CCD (II), R_0 (= 5 cm) is the radius of the input window and A,B and α are the fitted parameters: A (~ 0.1) is the demagnification factor of the optoelectronic chain, B (~ 0.25) and α ($\sim$2.7) describe the distortion itself. The position and the orientation of the CCD on the last II

*CCD stands for charged coupled device

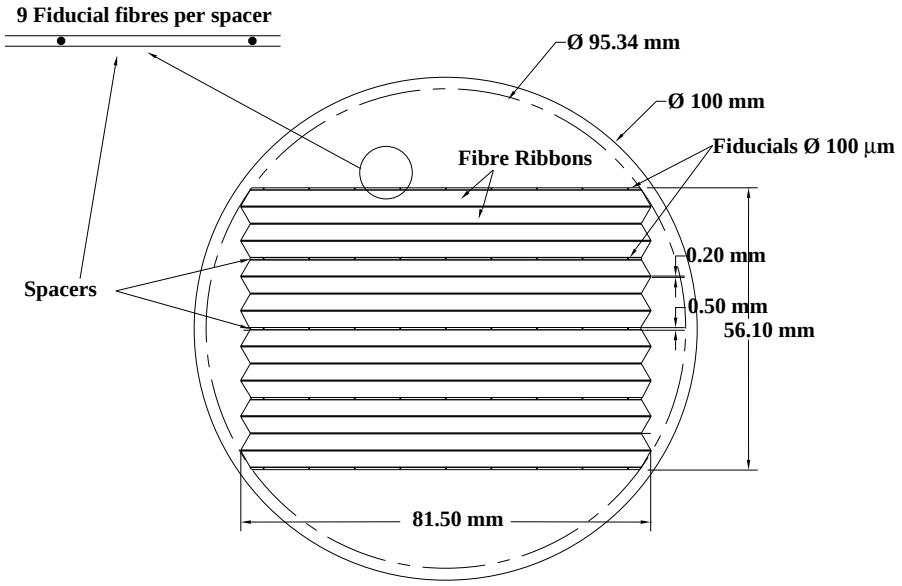

Figure IV.3: *View of the 16 fibre ribbons and the spacers containing fiducial fibres at the input window of the first II.*

output window are additional parameters in the fit. The resolution obtained from the fit at the input window is 110 μm .
Although the resolution obtained from this correction is sufficient for our tracking purposes, some chains have missing fiducials fibres or suffer from larger distortions near the edges than can be accounted for by the fit. This can lead to 200 μm tails, of the same order of magnitude as the expected tracking resolution.
Such calibration events are taken during the 12 s separating two proton ejections of the SPS, once every few minutes during data taking, to monitor the performance of the system. The image intensifier zoom, focus and MCP voltages and gate time are tuned every year using this data with the LED pulser tuned to give one photoelectron per pulse, and studying the response in terms of spot size, spot displacement and efficiency.
The spot size is the width of the charge distribution on the CCD caused by a single incoming photoelectron on the input window of the first II, it depends both on the CCD pixel size and the resolution of the II's. The latter can be optimised by tuning the operating voltages. The spot displacement, or displacement of a cluster representing a fiducial fibre with respect to its average position depends on the voltage focusing the electrons in the first II. After tuning, the standard deviations obtained on the distribution of spot sizes and displacement of the fiducial fibres are 136 μm and 89 μm , respectively.

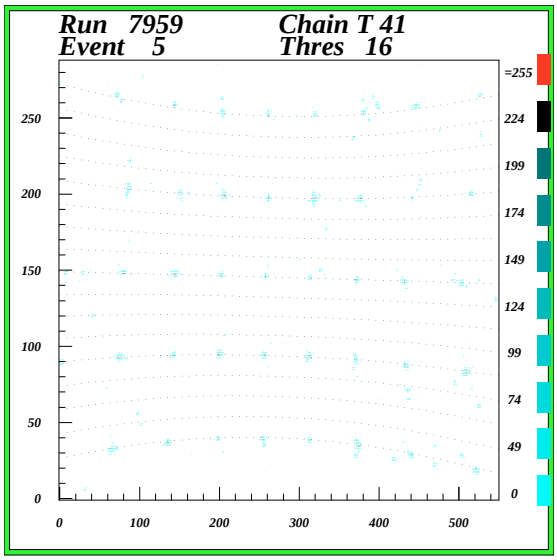

Figure IV.4: *CCD image of the fiducial fibres. The dotted lines are the approximate ribbon shapes. Each cluster of pixel corresponds to the image of a fiducial fibre.*

2.2 Muon data.

Muons associated to the beam or coming from cosmic rays provide a sample of minimum ionising particles (MIP). The signal of a MIP passing through a fibre ribbon is called a **track element**. The pixels forming a track element can be clustered into **hits** corresponding to single photoelectrons, this is done using the pulse height distribution of the CCD pixels [IV.5].
The density of hits (D) can be expressed as a function of the attenuation length ($\lambda \sim$ 220 cm), the distance (x) of the trajectory of the MIP with respect to the readout end of the ribbon and the reflectivity (r$\sim$0.8) of the mirror end of the ribbons as shown in figure IV.5:

$$D = \frac{D_L}{1+r}\left[e^{-\frac{x-L}{\lambda}} + r\, e^{-\frac{L-x}{\lambda}}\right]$$

where L=230 cm is the length of a fibre, D_L (5 hits per ribbon) is the density of hits at x = L. The effective attenuation length is 600 cm.
Monitoring λ and the ratio of the average number of hits far and near the readout as a function of time, one can check for aging of the fibres. No such effect has been observed, after 4 years of exposure.
Spurious hits were found associated to the track elements up to 1 mm away from them. This cross-talk had not been observed during a test using pion beam [IV.6] and an optoelectronic chain identical to the CHORUS chains but for the presence of extra-mural absorber on the input window of the first II stage. This effect is thus attributed to the absence of extra-mural absorber, removed from the final chain design in order to increase the quantum efficiency of the chain. This noise can be eliminated by cutting on the distance of hit to the centre of gravity of the track element it is associated to.

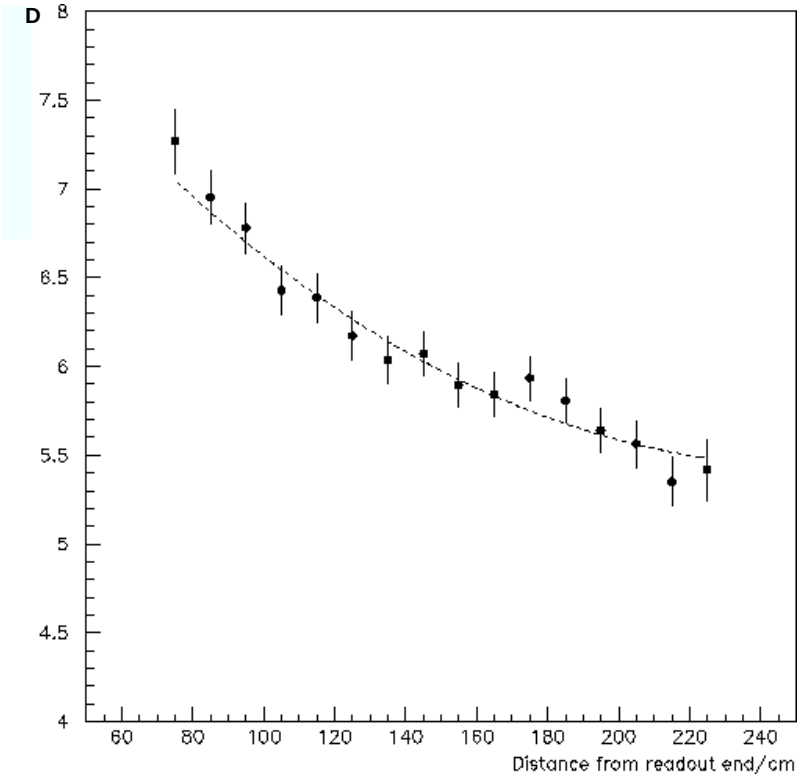

Figure IV.5: *Density of hits from a minimum ionising particle as a function of the distance from the readout end*

B The Target Trackers.

The target area is divided in two identical modules, placed downstream one another. One module is composed of two sets of emulsion stack and interface sheets with a target tracker (TT) hyperplane in between and three others immediately downstream as described in section III.1. Each hyperplane is composed of four fibre planes in four different projections (Y,Z and $Y^{\pm}$,$Z^{\pm}$ inclined by $\pm 8^{o}$ with respect to Y,Z). Each plane is made out of the 7-layer ribbons. The purpose of this assembly is to reconstruct neutrino interaction vertices and to predict the passage points of the charged particles in the interface emulsion sheets as accurately as possible.

1 Alignment.

The position of the fibre ribbons on the planes and their sagging (so-called "banana effect") was measured during the construction. Muons associated to the beam and cosmic muons data are used to perform the relative alignment [IV.7] of the TT planes, using the MINUIT software package [IV.8] to minimise the sum of the squares of the residual distances of the hits to the reconstructed muon tracks over typically 10 000 tracks. The following degrees of freedom are allowed : relative translations and rotations of the planes as well as relative

transverse translation of the fibre ribbons. To perform this procedure, hits due to cross talk are removed from the track elements used.

2 Performance.

After alignment, the resolution per plane has a σ ~185 μm for beam muons, in complete agreement with the test beam results [IV.6] used in the proposal of the experiment.
The two track resolution, coming from the addition in quadrature of the spot size and the hit residual, has a $\sigma \sim 380$ μm , giving a two track separation at 3.5 σ of 1.3 mm for parallel tracks.
The prediction accuracy into the changeable sheets was measured to have a $\sigma \sim 150$ μm in position and 2.5 mrad in angle using muons associated to the beam. Folding in the expected angular resolution for the emulsion measurement of 1.5 mrad, the TT's have an angular accuracy with a $\sigma \sim 2$ mrad.

C The Diamond Trackers.

1 Geometry

The Diamond trackers are made out of 3 modules, one upstream (DT1) of the Hexagonal Magnet and 2 downstream of it (DT2 and DT3) as shown in figure IV.6. Each module is made out of 3 sandwiches of 2 rhombus (diamond) shaped paddles. Each paddle contains sixteen 8 cm wide scintillating fibre ribbons as shown in IV.7. The fibres of one paddle of a sandwich are oriented at an angle of 120 degrees with respect to the fibres of the other paddle of that sandwich. The design is such that in front of each of the 6 triangles of the magnet, there is in each DT a paddle with its fibres along the magnetic field.
The numbering scheme of the paddles is the following : DFS where D is the DT module number, F is the face number (1 for the upstream paddles of a sandwich , 2 for the downstream one), S is the sandwich number (from 1 to 3).

2 Position measurements.

During the construction of the paddles, 11 plastic washers were glued on each of the 16 ribbons, according to a metal jig. The distance between the edge of the washers and the middle of third fibres on each side of the ribbon was measured with a microscope. This measurement yields an accuracy of 50 μm on the transverse position of the ribbons inside the paddles, as well as the knowledge of their exact inclination. The residual distance between the middle point of the two measured fibres and the straight line fit on these measurements for all DT paddles has a $\sigma \sim 30$ μm . Only DT111 for which the RMS is 95 μm does not enter this distribution, the quality of its construction being poorer.

Seven external metal fiducial marks were put on the honeycomb plates on each of the sandwiches, and a last mark was put at the centre of each DT. These marks were placed on the downstream face of DT1 and DT3 and on the upstream face of DT2.

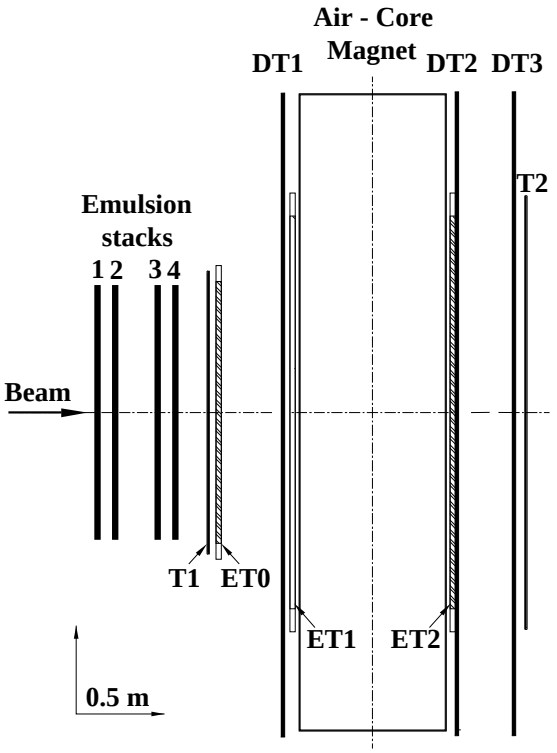

Figure IV.6: *Schematic side-view of the hexagonal magnetic spectrometer. The 3 DT modules are marked DT1, DT2 and DT3. The trigger hodoscopes are marked T1 and T2, the emulsion stacks are marked from 1 to 4. The three emulsion sheets marked ET0, 1 and 2 correspond to a configuration used in 1996 and 1997.*

The position of each of the fiducial marks on the DT's was measured with 2 mm accuracy along the beam and 1 mm accuracy in the transverse direction using an optical geometric survey. This allowed to fit the best plane through the fiducial marks which is the input to the start of the alignment procedure. This first measurement showed that the planarity of DT1 was poor. The geometers then performed a planarity measurement by measuring the X position with 0.5 mm accuracy of a grid of points on the downstream surface of DT1 and on the upstream faces of DT2 and DT3. The displacement in X of a fibre as a function of the track parameters is interpolated in the tracking procedure using that grid of points.

A β ray calibration was done for the paddles 111 and 113. Holes were drilled in the honeycomb at the positions of the plastic washers on each of the 16 ribbons of these paddles. Several runs were taken using 4 β sources per paddle, per run. Taking several runs with the same β ray source positions, the positioning accuracy was measured to be 1.5 pixels in the transverse direction at the level of the CCD ($\simeq$ 300 μm at the ribbon level). The

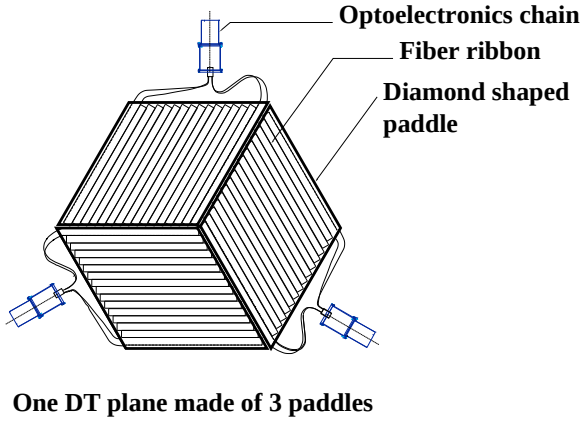

Figure IV.7: *Front view of three paddles forming one DT plane. Each paddle contains 16 7-layers fibre ribbons and is readout by a separate optoelectronic chain.*

asymmetric shape of the β spots and the presence of the washers made it difficult to measure the spot centre more accurately. However, the accuracy achieved was sufficient to check the logic of the detector construction and the geometry used in the database.

In August 1996, an optical alignment system (rasnik) [IV.9] was installed on DT1, to allow monitoring of the position of its centre with respect to its support frame. The measurement showed a displacement of about 1 mm of the centre of DT1 along the beam axis between the measurements with the Hexagonal Magnet on and off. The transition time between the 2 positions being of the order of an hour and a half (see figure IV.8). A combined measurement using the rasnik, temperature probes and geometrical measurement confirmed the hypothesis that the movement was driven by the temperature changes, and showed that the displacement of DT1 along the beam is linear with the distance from the centre (the edges are fixed). This temperature effect, however, only marginally affects the neutrino data :

- the neutrino data are taken with the magnet on, and the only events affected are the events occurring during the rise of the temperature following a few hours beam and magnet stop.

- the standard deviation of the position in X of the impact point in DT1 of particle coming from a neutrino interaction in the target with respect to the position calculated when neglecting DT1 movement is $\sim$120μm , and 28 μm in the transverse direction.

The following effects were also noticed in the beam direction : fast vibrations with a $\sim$ 10 μm RMS due to the ventilation used to cool the air-core magnet and $\sim$ 50 μm movements at every magnet pulsation.

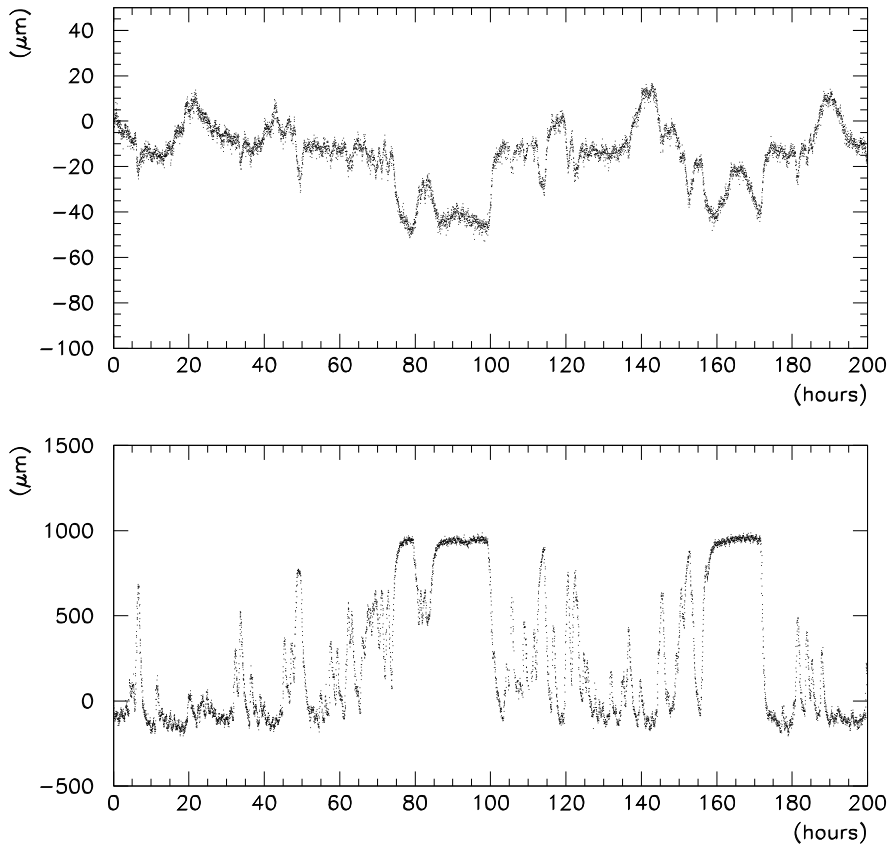

Figure IV.8: *Displacement of the centre of DT1 in one transverse direction (top) and along the beam axis (bottom) as a function of time. The large excursions correspond to periods where the magnet was off.*

3 Alignment.

Muons from cosmic rays and associated to the beam were used for alignment purposes. The beam muon data set was taken in full 2 hours run with the hexagonal magnet switched off. The effect due to the cooling down of the magnet area is therefore present in these data. However, these muons are in the beam direction and therefore have a negligible contribution to the longitudinal alignment of the detector, and the associated excursions in the transverse directions were of the order of 50 μm . The cosmic ray data are taken in between two proton ejections of the SPS: the magnet is at the same temperature as for neutrino events.

The tracks used as reference for alignment were chosen according to the following criteria:

- sample 1:
  - they are reconstructed in the last 12 planes of the TT's,

- they hit at least 5 out of the 6 possible DT planes,
- they do not cross the spokes of the magnet.

This combination of requirements has the advantage to select tracks which are unlikely to be fake combinations of hits, but due to the geometry of the TT and DT planes, no such track goes through the outer 4 ribbons (40 cm) of any DT1 paddle. An additional sample of tracks was added to align DT1 :

- sample 2 :
  - they are reconstructed in the last 12 planes of the TT's,
  - they hit both DT1 planes,
  - they are out of the geometrical acceptance of DT2 and DT3.

Alignment was performed with respect to the last twelve TT planes which are placed downstream of the fourth emulsion stack. The MINUIT minimisation package [IV.8] was used to minimise the sum of the square of the residual distances of the centre of gravity of track elements to the fitted tracks.

The DT's were aligned one after the other starting with DT1, the closest to the target trackers. The aligned position of DT1 was then used to align DT2, and later the new position of DT2 to align DT3. The tracks used for alignment of a specific DT were required not to have more than one candidate track element in the extrapolation road for that DT.

The 1994 data sample had to be subdivided in time periods as the detector seemed to have moved during the year: figure IV.9 shows the average residual distance between the TT-DT1 prediction and the DT hits as a function of the run number before alignment for a DT2 paddle. One can separate two periods around run 1000.

The translations and rotations were let vary for each paddle independently. At the end of the procedure, each ribbon is let vary in the transverse direction. The residual transverse displacement to be applied to the ribbons at the end of the alignment procedure has an RMS of $\sim$40 μm , in agreement with the accuracy expected from construction. Figures IV.10 and IV.11 show the residual distance distributions in the 6 DT1 paddles between the TT track prediction and the hits in the DT before and after alignment. The difference of centring of the distributions in these 2 figures shows the improvement of the alignment of DT1 with respect to to the TT by the procedure. The width of the distributions is dominated by the extrapolation error due to the 50 cm distance between the TT and DT1. Figure IV.12 shows the distribution of the hit residual distances to the track fitted on all TT and DT planes after alignment. The distributions are centred on zero (within the statistical error) in all the DT paddles.These residual distances can also be interpreted in terms of residuals per plane using the fact that a track yields typically 5 or 6 hits per plane.

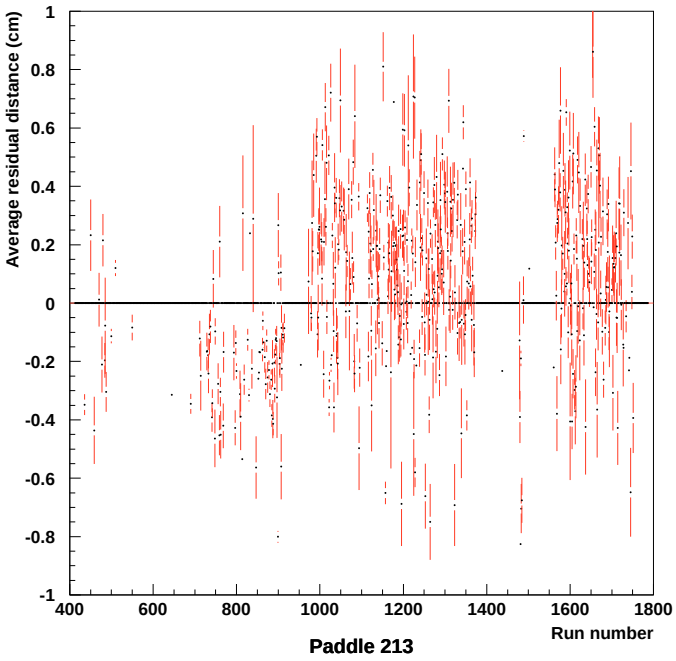

Figure IV.9: *Run dependence of the average residual distance between the TT-DT1 prediction and the DT2 hits in paddle 213, before alignment. The width is dominated by the extrapolation error due to the distance between the centre of gravity of the TT-DT1 fit and DT2*

4 Performance.

After alignment, the residual distances of the track elements to a fitted track coming from a global straight line fit on track elements in the last 12 TT planes and the 6 DT planes have $\sigma_{DT1} \sim 177$ μm , $\sigma_{DT2} \sim 133$ μm and $\sigma_{DT3} \sim 126$ μm . Comparison with Monte Carlo simulated data show that this can be explained by an intrinsic resolution of 180 μm per plane, the positions of the TT and DT planes along the beam direction and multiple scattering.
The results obtained for the DT resolution are compatible with the TT resolution obtained independently. They also agree with the value of 140 μm given for the residuals distance of track elements with respect to pion tracks fitted on the signal in 4 fibre ribbons exposed to a test beam[IV.6]. In the proposal, the optimistic value of 140 μm has been taken as the intrinsic resolution, and used to predict the momentum resolution achievable by the hadron spectrometer.
Although this result is very promising, the sample of tracks used for alignment was a very clean one: tracks with more than one track element in the extrapolation roads were rejected, the number of planes hit was required to be nearly maximal, and the signal associated noise was cut away. However, in neutrino event reconstruction, a maximum number of tracks have to be reconstructed. Such criteria and cleaning procedures cannot be applied anymore due to the high hit density in such events, and the requirement that the comput-

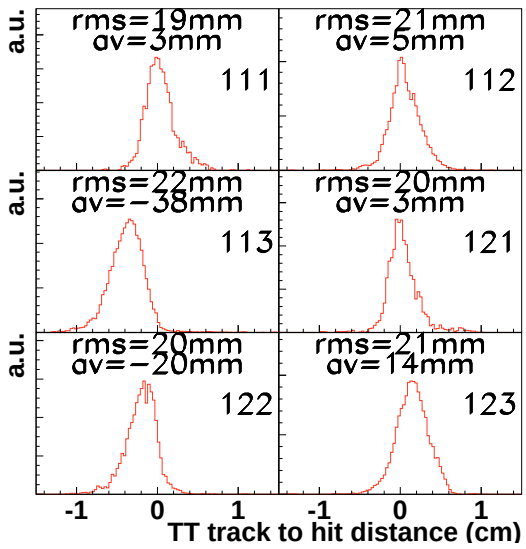

Figure IV.10: *Residual distances in cm between the TT prediction and the DT1 hits, before alignment. Each histogram corresponds to the paddle number indicated on the right of the distribution. The width of the distributions is dominated by the error due to the extrapolation on 50 cm distance between the end of the target tracker and DT1.*

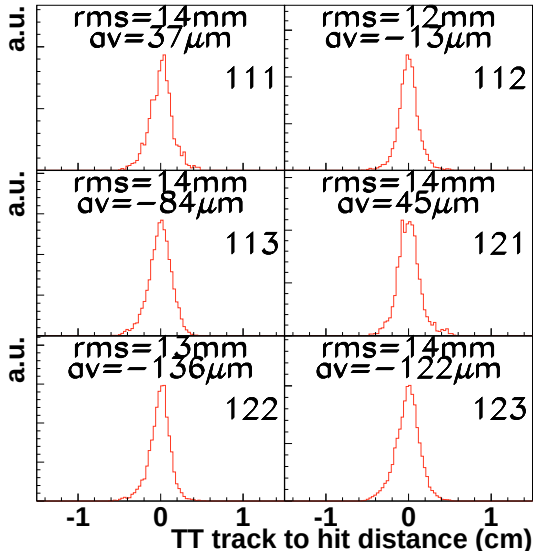

Figure IV.11: *Residual distances in cm between the TT prediction and the DT1 hits, after alignment. Each histogram corresponds to the paddle number indicated on the right of the distribution. The width of the distribution is dominated by the error due to the extrapolation on 50 cm distance between the end of the target tracker and DT1.*

ing time should be kept low. Some of the effects that contribute to the degradation of the resolution have already been mentioned such as the fact that the distortion correction can be insufficient at the edges of the CCD, other sources will be described in the next chapter.

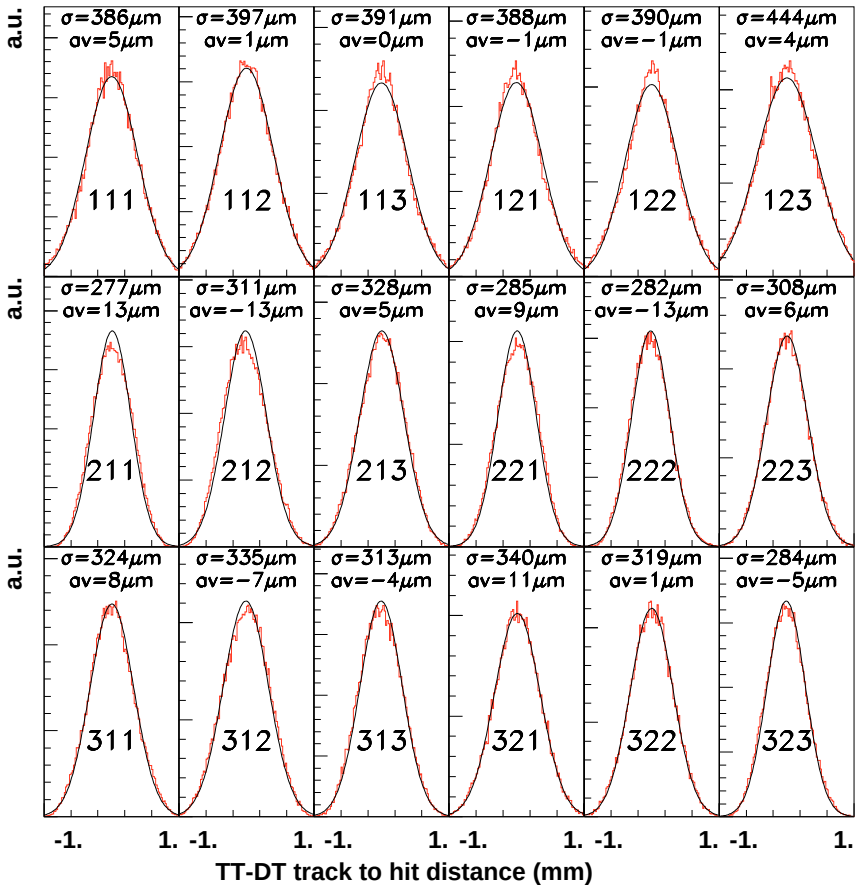

Figure IV.12: *Residual distances in mm of the hits to the tracks fitted on the 12 TT planes, DT1, DT2 and DT3 after alignment. Each histogram corresponds to the paddle number indicated in the distribution. The resolution per plane is obtained using the residuals of the centre of gravity of the (typically 5 or 6) hits in the plane (track elements).*

References

[IV.1] P.Annis *et al.*,*Nucl. Instrum. Methods* A **409**, 629 (1998).

[IV.2] T. Nakano *et al.*,Proceedings of the Workshop on Scintillating Fiber Detectors, Notre Dame, (1993). SCIFI **93**, 525 (1993).
T. Nakano *et al.*,IEEE Trans.Nucl.Sci. **39**, 680 (1992).

[IV.3] M. Gruwé, PhD Thesis, Université Libre de Bruxelles (1994).

[IV.4] C. Mommaert, PhD Thesis, Vrije Universiteit Brussel (1995).

[IV.5] P. Lendermann, PhD Thesis, Humboldt-Universität (1994).

[IV.6] S. Aoki *et al.*,*Nucl. Instrum. Methods* A **344**, 143 (1994).

[IV.7] G. Brooijmans, Chorus Internal Note 96004,1996.

[IV.8] MINUIT : Function minimization and error analysis, Application software group, CN division, CERN.

[IV.9] J. Dupraz *et al.*,*Nucl. Instrum. Methods* A **388**, 173 (1997).

Chapter V
Tracking in the Diamond Trackers.

The role of the air-core magnet and of the Diamond Trackers is to provide a good momentum and charge reconstruction of the charged particles orginating from a neutrino interaction in the target. This is particularly important as it allows not only to identify possible non-muonic τ^- decay candidates but also to reject background coming from the decay of positive charmed particles produced in ν CC interactions where the primary lepton is not identified.
This chapter describes the track finding and fitting methods used as well as the problems which can affect the quality of momentum and charge reconstruction. The efficiencies for the τ^- decays search and its background rejection will be derived in the next chapter from the resolutions obtained here.

A Track element finding.

The passage of a charged particle through a fibre ribbon leaves a signal on the CCD called a track element which is a cluster of pixels over threshold. The position of the image of

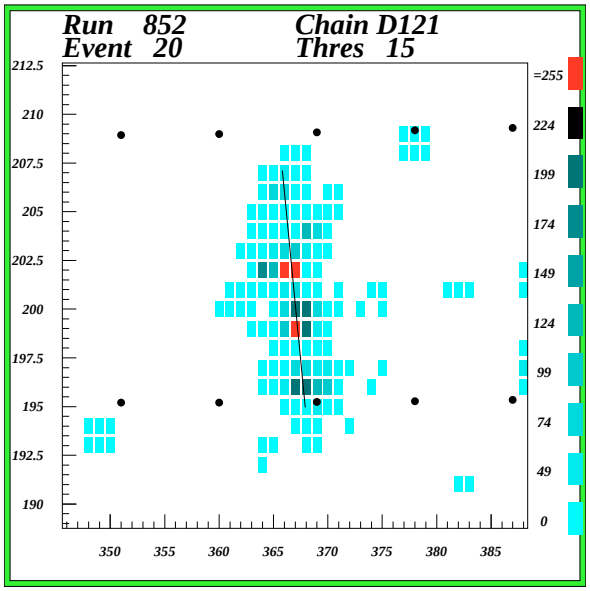

Figure V.1: *Image of the signal left by a muon associated to the beam on a CCD. The black dots show the reconstructed contours of the ribbon and the shaded rectangles the pixels hit. The straight line is the reconstructed track element.*

a ribbon on the CCD is calculated using the distortion correction parameters. The slope

and the barycentre of the track elements are reconstructed on the CCD as shown in figure V.1 by a clustering algorithm. The pixels weigh in the fit according to their pulse height. The pulse height is normalised in such a way that a minimum ionising particle (mip) gives track elements of total pulse height on average equal to 1. In neutrino events the track elements from shower tracks have to be disentangled when their signal is not separated by non-hit pixels. This is done using cuts on the transverse width of track elements and the total pulse height. The track element reconstruction efficiency in the DT chains was computed to be 97 % using beam associated muon tracks. When measuring the efficiency of a specific plane, track elements were required to be found in all 5 other planes traversed by the track, to insure that the track was not a random combination of track elements.
The track element finding procedure also results into artificial splitting of physical track elements (figure V.2) into two software track elements separated by up to 2 mm in CHORUS space. The fraction f_s of split track elements can be measured by counting the number

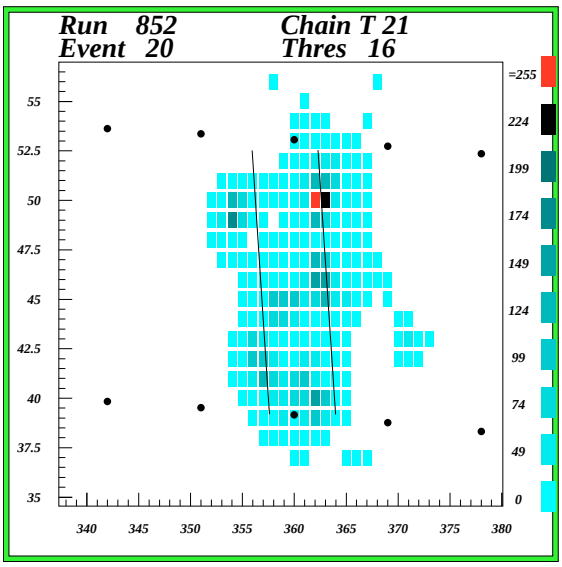

Figure V.2: *The shaded rectangles show the signal of muon on a CCD, the black lines represent the reconstructed barycentres of two software track elements.*

N_2 of track elements for which the closest neighbour is at a distance of less than 2 mm in a sample of N_{tot} reconstructed track elements. A cut of 1.5 pixels on the fitted half-length of the neighbour track elements is made such as not to count signal associated noise as artificial splitting : figure V.3 shows the half length of track elements belonging to tracks and of their closest neighbour for muons simulated using the full detector simulation.

$$f_s = \frac{N_2}{N_{tot} - N_2} = C_{algo} + C_{mult} \qquad \text{(V.1)}$$

The fraction f_s is the sum of two contributions : one from real track multiplicity C_{mult} in the event, and one from artificial splitting of one single physical track element in the reconstruction algorithm : C_{algo}. This last contribution is important to evaluate as it deteriorates the resolution of the detector. Figure V.4 shows the fraction of split track

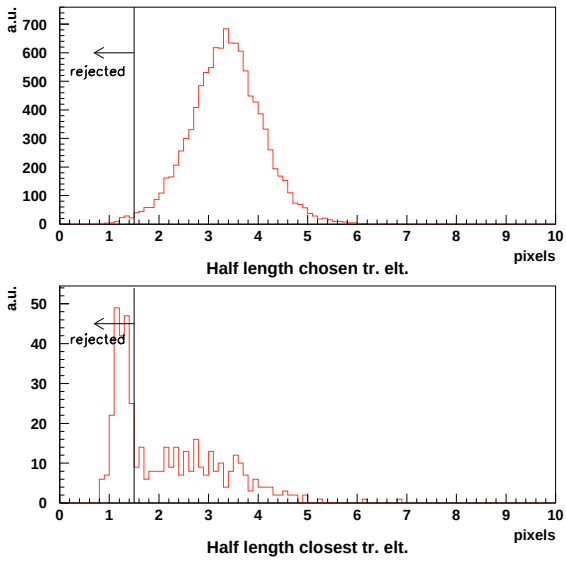

Figure V.3: *Half length of track elements belonging to a (simulated) muon track (top) and their closest neighbour (bottom). The peak in the bottom figure is signal associated noise which is rejected using the shown cut.*

elements on the 18 DT and the module 2 TT chains for cosmic muon events. The cosmic muon data are taken during the 12 seconds separating two neutrino bursts. During this period the CCD cameras are cleared very often, producing more dead time, but yielding less thermal noise for these events than for burst events.

The fraction f_s was measured both using data and the full detector simulation for neutrino events and for single muons. The Monte Carlo simulation allows to measure $C_{algo,MC}$ directly for single tracks by switching off physical effects that give rise to secondary tracks, such as bremsstrahlung, secondary interactions and δ ray production . The other numbers for C_{mult} and C_{algo} in data and Monte Carlo can then be deduced as shown in table 5.1 from the measured f_s values and assuming that the full Monte Carlo simulation reproduces well the track multiplicity of real events, and that the software contribution C_{algo} is the same for all simulated events. These assumptions are reasonable as shown by the fact that the found value of C_{algo}=0.05,0.06 for real events is compatible for single muons data and for neutrino event data. For the data, these numbers are an average on all the chains and a large number of runs. The artificial splitting depends strongly on the calibration and response of the optoelectronic chains, such that the fraction of split track elements will vary from chain to chain and with time as shown in figures V.4 and V.5.
The track elements found on the CCD are corrected for distortion, and mapped to the CHORUS coordinates (cf. Chapter IV, section 2). The centre of gravity of each track element defines a straight line $Z=\alpha \cdot Y + Z_0$ in the CHORUS coordinates and a X position. At that level the alignment translations and rotation of axis X are taken into account.

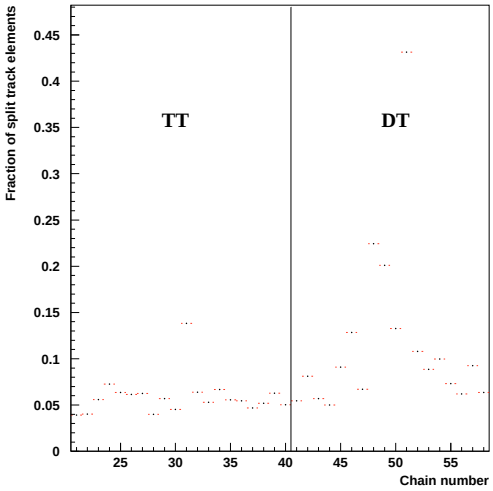

Figure V.4: *Fraction of split track elements per chain for cosmic muon events. Large differences can be seen between the chains.*

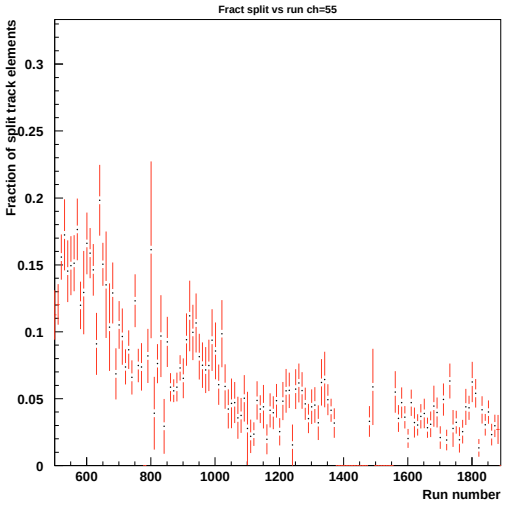

Figure V.5: *Variation of fraction of split track elements as a function of the run number for a DT chain.*

Data	f_s	C_{mult}		C_{algo}	
Monte Carlo μ^- , no physical process	.02	.00	$\rightarrow$	.02	
				$\downarrow$	
Monte Carlo μ^- , all physical processes	.04	.02	$\leftarrow$	.02	$\searrow$
		$\downarrow$			$\downarrow$
Data μ^-	.07	.02	$\rightarrow$	.05	$\downarrow$
Monte Carlo neutrino events	.10	.08	$\leftarrow$	.02	$\hookleftarrow$
		$\downarrow$			
Data neutrino events	.14	.08	$\rightarrow$	.06	

Table 5.1: *Summary table of the measured fraction of split track elements in the DT chains and of the contribution from physical and software effects. The arrows show how one value has been deduced from the other, always using the measured f_s. The statistical error on these numbers is typically .01.*

B Track finding in the DT's.

The track finding in the DT's is done by extrapolating all tracks reconstructed in the TT's up to the last 12 planes. The extrapolation road widths have been chosen to account for the 3 mrad angular resolution of the track fitted on the last 3 TT hyper-planes and the bending due to the magnetic field for particles with momenta down to 1 GeV/c. In the

module	DT1	DT2	DT3	TST
road half width (cm)	0.5	3.5	3.8	5

Table 5.2: *Road half widths for extrapolation in the DT's. For DT2,3 and the target streamer tubes (TST) what is shown is the value for planes where the fibres or wires are parallel to the magnetic field. For the other projections, these values are multiplied by the cosine of the angle between the fibres or wires and the magnetic field, with a minimum at 2.5 cm for the TST's when their wires are perpendicular to the magnetic field.*

2 DT1 planes, the track element closest to the TT track prediction is chosen within the road. A straight line fit is then performed on the last 12 planes of the TT's and DT1 together. The nonorthogonality of the paddles to the beam direction is taken into account before the fit. The new track parameters are extrapolated to DT2,3 and the TST's. All track elements or TST clusters within the road are collected. If 5 out of the 8 planes downstream of the magnet are hit, the track is accepted.
The air-core magnet is composed of 6 triangles. Only the tracks remaining in the same magnet triangle as they go through the magnet are momentum fitted, as the other tracks are subject to large multiple scattering or shower as they cross the spokes of the magnet. The geometrical acceptance of the DT tracking for particles coming from neutrino interactions in the emulsion target is given in table 5.3. The table shows a clear stack and module dependence :

- The average number of reconstructed tracks is lower for odd stacks. The TT tracking is performed in the 3 last hyperplanes of a module and reconstructed tracks are extrapolated to the most upstream hyperplane if possible. As the particles cross one more radiation length than for even stack before reaching the last 3 hyperplanes, less tracks are reconstructed for events happening in odd stacks. Reconstructed tracks are also difficult to extrapolate upstream due to multiple scattering and secondary interactions in the even emulsion stack: less tracks are reconstructed in odd stacks but, also less fake tracks and low energy particles. This configuration of the TT modules also yields an artificial shifting of the reconstructed vertices downstream of their real location.

- As stack 1 reconstructed tracks tend to be of higher quality or more energetic than stack 2 reconstructed tracks, their probability to extrapolate into TT module 2 is higher.

- if a TT module 1 track is successfully extrapolated to TT module 2, it is more likely to fall inside the angular acceptance of the DT's.

Track	stack 1	stack 2	stack 3	stack 4
<number of vertex tracks/event>	3.158	5.099	3.129	4.782
Fraction not in TT module 2	0.399	0.536	—-	—-
Fraction outside of the DT	0.021	0.017	0.067	0.106
Fraction through magnet spokes	0.086	0.071	0.177	0.189
Fraction DT tracking performed	0.493	0.377	0.756	0.705

Table 5.3: *Geometrical distribution of TT tracks from neutrino interactions reconstructed in the emulsion stacks (1994 data). The statistical error on these numbers lies between .001 and .003*

C Muon tagging.

After the track finding in the DT's, the angle and impact points at the calorimeter entrance of the fibre tracker tracks are compared to those of the tracks [V.2] and clusters [V.3] reconstructed in the calorimeter and the muon spectrometer. The maximum angle difference allowed between the fibre tracker tracks and the calorimeter or spectrometer tracks is 140 mrad. Figure V.6 shows the efficiency for keeping the matched muons as a function of the angular cut for simulated ν_μ CC events. Although the cut is clearly very

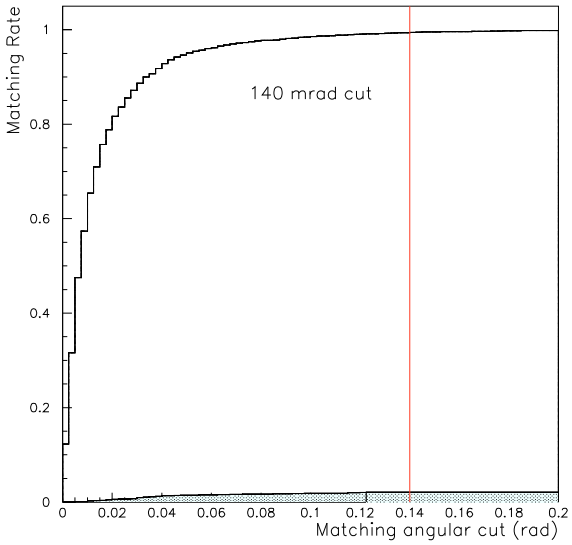

Figure V.6: *white histogram : efficiency for keeping the good matches as a function of the slope difference cut. The used angular cut of 140 mrad for tracks in projection is shown. Hatched histogram: percentage of "fake" matches for ν_μ CC events.*

wide, it does not introduce impurities in the sample. Figure V.6 shows that the probability of matching tracks to fake muons does depend very little on the angular cut. The maximum transverse distance allowed between the fibre tracker track and the calorime-

ter (spectrometer) track at the most upstream point where the latter is reconstructed is 10 (20) cm. All TT tracks satisfying these criteria are associated with the downstream tracks. The vertex finding takes place after this step: TT tracks are associated two by two if their most downstream plane hit do not differ by more than 4 planes and if their point of closest approach is not too far upstream or downstream from their first plane hit. After this step, all tracks with a starting point close to the found vertex candidates are added to each vertex and the vertex position is refitted. Each reconstructed vertex gets a different weight depending on how upstream it is located and on the type of tracks originating from it: the tracks get a higher weight the more detectors they can be found in. The quality of the muon tagging allows to select the correct fibre vertex to search for in the emulsions, by giving it a higher weight. Tracks belonging to several vertices are only assigned to the vertex with the highest weight and the other vertices are refitted without that track, and its weight is recalculated. Only the tracks belonging to the vertex with the highest weight will be considered for scanning in the emulsions.

The track matching allows to recognise muon tracks. A Monte Carlo study shows that 89 % of the CC ν_μ simulated events with a vertex reconstructed in the right emulsion stack have a muon tagged at the vertex and in 99% of the cases the tagged track corresponds to a genuine muon. Only 3 % of the reconstructed NC ν_μ simulated events have a muon tagged at the vertex, 90% of which come for pion or kaon decay. The remaining 10% come from primary hadrons which reach the spectrometer. This method of muon tagging insures purities of 99% and 68% for the CC and NC samples predicted in the emulsion [V.1]. Figure V.7 shows the efficiency of muon matching at the vertex as a function of the muon simulated momentum. The fall off at low energy is expected as muons lose about

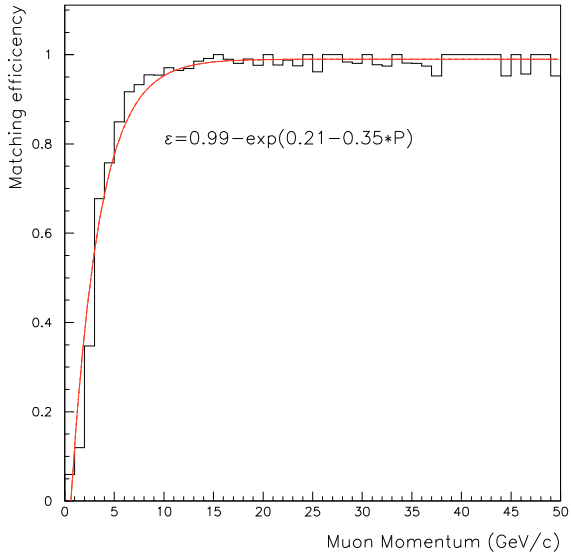

Figure V.7: *Efficiency for matching a muon to the vertex as a function of the simulated muon momentum at the vertex for ν_μ CC events.*

2 GeV in the calorimeter, and only reach the muon spectrometer if they have a higher

energy. For low energy muons, the identification relies on clustering [V.3] and tracking [V.2] algorithms in the calorimeter, which are only efficient for isolated muons. Moreover, low energy muons have on average a larger angle and are therefore more likely to escape the detector to the side.

D Momentum fit.

The momentum fit in the DT's is performed after the vertex finding. Only the tracks associated to the reconstructed primary vertex are momentum fitted. If no vertex has been found, as for instance for special events such as beam associated muons which do not originate in the target, all tracks are momentum fitted. The momentum fit is performed on every combination of track elements in DT2, DT3 and clusters in the TST's, with a maximum of 50 combinations. If more combinations are possible, the planes with the largest amount of possible hits are temporarily removed from the fit. The combination with the best fit probability is chosen to be the right one. The previously withdrawn planes are reintroduced by choosing the track elements closest to the track fitted downstream of the magnet and refitting.

Table 5.4 summarises the behaviour of muon and non muon tracks in terms of number

	muon tracks $N_{combi} \leq 100$	muon tracks $N_{combi} > 100$	other tracks $N_{combi} \leq 100$	other tracks $N_{combi} > 100$
fraction of total	.88	.12	.70	.30
$< N_{fit} >$	4.4	20.8	4.7	14.8
fraction where $N_{fit}=0$	.12	.36	.48	.54
$<N_{fit}>$, $N_{fit} > 0$	4.86	31.1	12.1	29.1
$<N_{same\ sign}/N_{fit}>$	.96	.92	.98	.92

Table 5.4: *Behaviour of tracks in terms of possible hit combinations downstream of the magnet (before withdrawing planes to get down to 50 combinations maximum) for neutrino event data where N_{fit} is the number of combinations with a fit probability greater than 0.5% and $N_{same\ sign}$ is number of combinations giving the same sign of charge as the combination with the best fit probability.*

of combinations of hits downstream of the magnet (before reducing the number of planes to getdown to 50) for neutrino data. The absence of any fit for 50% of the non-muon tracks, shows the difficulty of the tracking in the target area and the presence of random associations of hits to form a target track. Although the mean number of combinations is, on average, rather large, most of them give the same sign of charge for the momentum fit, which gives some confidence in the background rejection power of the momentum reconstruction.

The fit is linear and has 5 parameters : the slope and intercept of the track in the plane parallel to the magnetic field (so-called *non-bending* plane), and the three parameters which describe a parabola in the plane perpendicular to the field (so-called *bending* plane). The following approximations have been made:

- the direction of the track does not vary in the *non-bending* plane as this would introduce non-linear terms. The ratio of the slopes in the non *bending* plane downstream and upstream of the magnet is $\sqrt{\frac{1+tan\theta^2_{down}}{1+tan\theta^2_{up}}}$ where θ is the track angle in the *bending* plane . Figure V.8 shows the relative variation of the slope in the *non-bending* plane as a function of the slope in the *bending* plane and of the momentum. This effect is at most of the order of the effect of multiple Coulomb scattering for slopes greater than 400 mrad and becomes negligible at smaller angles.

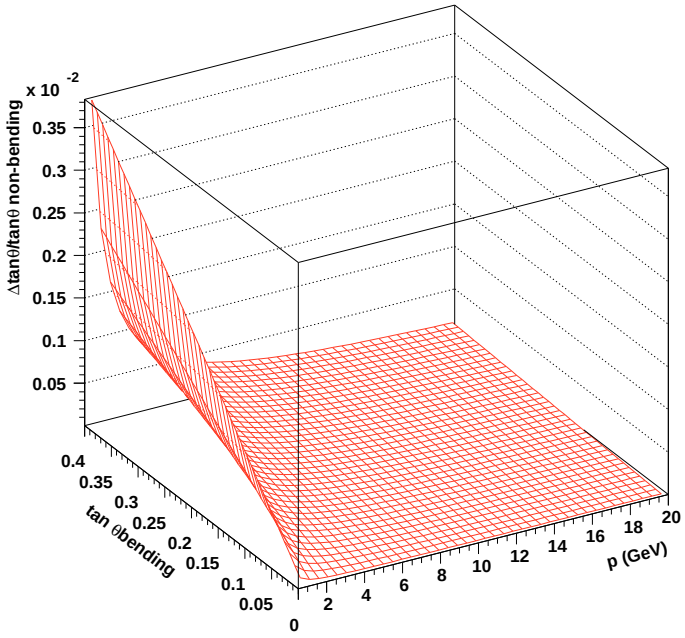

Figure V.8: *Relative variation of the slope in the* non-bending *plane as a function of the slope in the* bending *plane and of the momentum*

- the circular trajectory of the charged particle in the bending plane has been approximated by a parabola such that the constraint equations are linear. The difference in the momentum estimate coming from this approximation is $\left|\frac{P_{parabola}-P}{P}\right| \leq 4\ \ 10^{-5}$ in the momentum and angular ranges considered for analysis.

After a first fit, the multiple scattering error is calculated on the basis of the reconstructed momentum and added quadratically to the setting error on the hits. The knowledge of the impact of the track on both sides of the magnet allows to calculate the width of magnet traversed (between 75 and 85 cm). A second fit is performed and hits at more than 3 σ away are rejected and the track is refitted. Only the combinations with the smallest number of rejected hits are considered.

The following sections give estimates of the obtained momentum resolution $\frac{\sigma(p)}{p}$ for different sets of data. Two effects contribute to the momentum resolution: the multiple

scattering in the detector material which yields a constant term and the resolution of the fibre trackers which gives a term proportional to the momentum. The two contributions being independant, the total resolution is given by the quadratic combination of the two terms.

1 Resolution from single tracks.

1.1 Simulated events.

A first simulation takes into account only the multiple scattering effects. It is referred to as the "simple simulation" hereafter. Several samples of 5000 negative tracks were simulated per momentum between 2 and 20 GeV at various angles (from 0 to 400 mrad). The simulated efficiency per plane was 100 % and the resolutions were 175 μm for the fibre planes and 3 mm for the TST planes.

The obtained resolution is :

$$\frac{\sigma(p)}{p} = 0.21 \oplus 0.026 \times p \tag{V.2}$$

where $\oplus$ represents the quadratic combination of the 2 terms. The mean reconstructed momentum is well centred on the simulated value and independent of the angle of the track.

The deterioration of the momentum resolution was estimated as a function of the percentage of artificially split track elements. A Gaussian distributed displacement of the track elements was introduced in the simulation using the distribution of distances between two reconstructed track elements corresponding to the data. Figure V.9 shows the behaviour of the part of the momentum resolution due to the fibre tracker resolution as a function of the percentage of split track elements introduced. The effect of the splitting is to introduce large tails in the 1/p distributions, as shown by the difference in the estimate of the resolution if one uses the RMS or the sigma of a gaussian fit on the 1/p distributions at simulated momenta from 2 to 20 GeV/c. The fit of the resolutions obtained using the RMS as a function of the software splitting yields a parabola of equation

$$\left(\frac{\sigma(p)}{p^2}\right)_{fibres} = 0.0267 + 0.255 \cdot f_s - 0.127 \cdot f_s^2. \tag{V.3}$$

Fitting the resolution obtained from the gaussian fits to the 1/p distributions yields a parabola of equation

$$\left(\frac{\sigma(p)}{p^2}\right)_{fibres} = 0.0269 + 0.0279 \cdot f_s - 0.425 \cdot f_s^2. \tag{V.4}$$

Samples of μ^- tracks in the same momentum bins were generated and passed through the full GEANT detector simulation. The origin of the tracks was chosen to be downstream of the last emulsion plate to minimise the energy loss before the magnet. The resolution of fibre trackers in the simulation is 175 μm as in the simple simulation. The average fraction

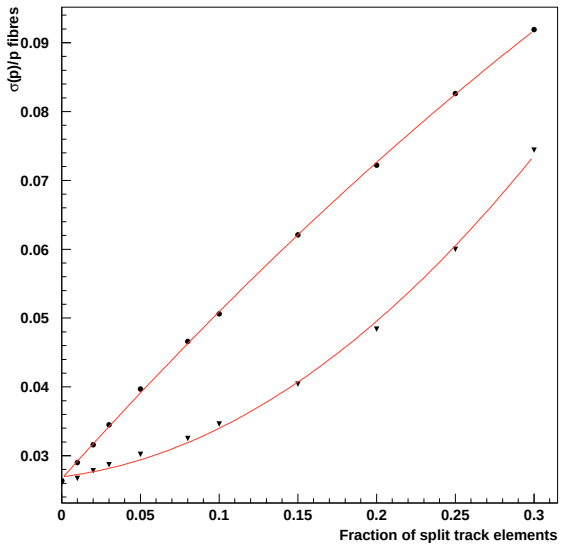

Figure V.9: *Behaviour of the momentum resolution as a function of the fraction of split track elements. Each point corresponds to a sample of 5000 tracks with slopes following a Gaussian distribution centred on zero with a σ=200 mrad. The top curve and data correspond to the resolutions obtained using the RMS of the 1/p distributions, the bottom ones use the sigma of the gaussian fits to the 1/p distributions for momenta simulated between 2 and 20 GeV/c. The equations of the curves are in the text.*

of split track elements in the GEANT simulated data was determined to be about 2 %, the average efficiency per plane is 97 % The momentum resolution obtained is :

$$\frac{\sigma(p)}{p} = (0.216 \pm 0.003) \oplus (0.0333 \pm 0.0003) \times p \qquad \text{(V.5)}$$

and the reconstructed momentum deviates from the simulated value on average by 10 MeV/c. This deviation is compatible with the effect of energy loss processes in the material traversed. Figures V.10 and V.11 show the fraction of particles with wrongly reconstructed sign of the charge as a function of the simulated momentum for the simple simulation with 2% splitting and for the full GEANT simulation. The agreement between the two simulations is good, although the simple simulation yields a slightly better resolution and smaller fraction of wrongly assigned sign. Indeed, there are several degrading effects not taken into account in the simple simulation such as energy loss processes or the non-gaussian tails of the multiple scattering angle distribution.

1.2 Data: beam associated muons.

A sample of beam associated muons was taken while the magnet was being pulsed. This sample is completed by a selection of quasielastic ν_μ CC events. A total of 2000 tracks were measured in the full detector, with a momentum smaller than 20 GeV/c, allowing the comparison between the momentum reconstructed in the fibre trackers and the momentum

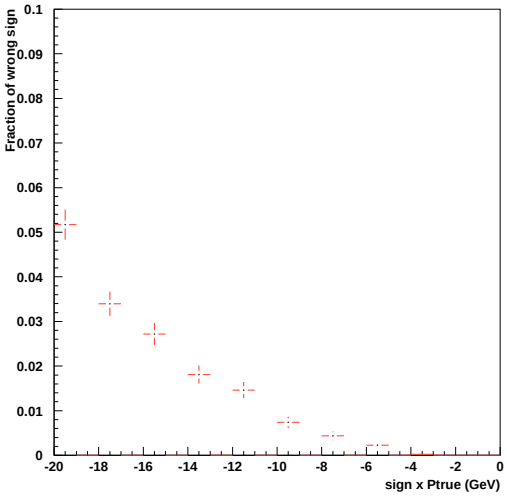

Figure V.10: *Fraction of wrongly reconstructed sign as a function of the true momentum for muons simulated using the simple simulation.*

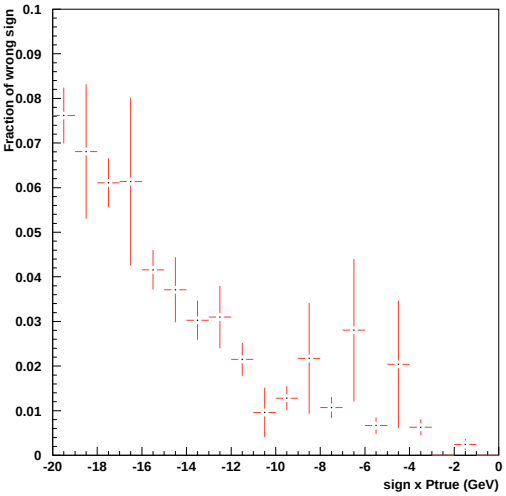

Figure V.11: *Fraction of wrongly reconstructed sign as a function of the true momentum for muons simulated using the full GEANT simulation.*

reconstructed in the muon spectrometer. The comparison cannot be done directly as the muons cross the calorimeter between the two spectrometers. The energy loss in the calorimeter is computed and the momentum from the muon spectrometer corrected for it. The energy loss is on average 1.7 GeV and has an error of 9 %. The momentum resolution in the hexagonal magnet is estimated using tracks which give a signal in all 6 DT planes and for which the probability of the fit is higher than 0.005. Figure V.12 shows the quadratically combined resolution of the two spectrometers as a function of the momentum measured in the muon spectrometer corrected for the energy loss in the calorimeter (P_{spec}). For momenta below 6 GeV/c the momentum estimate is obtained from the range of the muons stopping in the spectrometer as above 6 GeV/c it uses the bending of the muon trajectory in the magnets. The sign is always attributed using the bending information. As in data the reference momentum with which the fibre tracker momentum is compared is spread and the statistics is limited, the comparison is done in bins of 2 GeV/c. The obtained resolution is :

$$\frac{\sigma(p)}{p} = (0.24 \pm 0.05) \oplus (0.037 \pm 0.007) \times p \qquad \text{(V.6)}$$

It is in between the resolution obtained from the RMS and sigma of gaussian fits from the simple simulation using a fibre tracker resolution of 180 μm in the DT's and TT's and a fraction of track element splitting of 8.2 % (as measured in the data sample used), which is reasonable agreement, considering the low number ($\simeq$130) of tracks available per momentum bin in the sample.

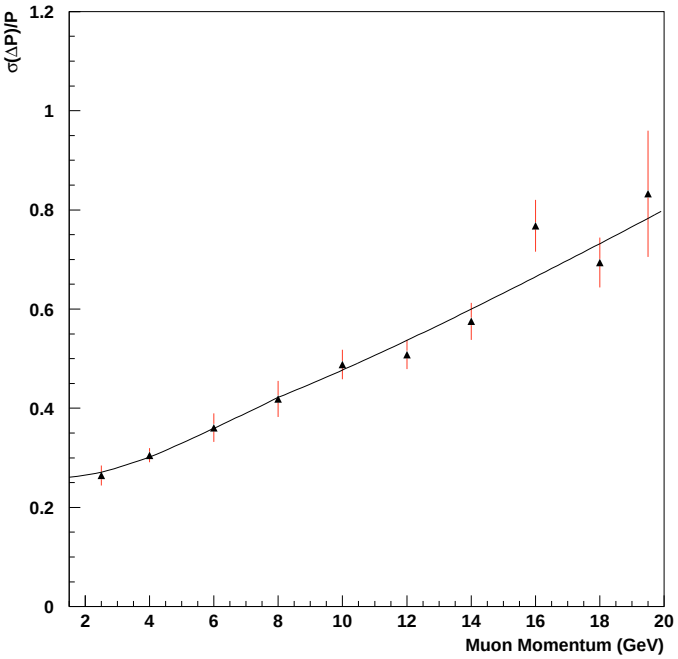

Figure V.12: *Momentum resolution from the fibre tracker measurement. Each dot represents the sigma of gaussian fits to* $\frac{P_{spec}-P_{fibre}}{P_{fibre}}$ *distributions as a function of the average* P_{spec}*. The plain curve shows the fit of to the combined resolutions of the two spectrometers. The vertical error bars are statistical.*

2 Neutrino events.

For neutrino events the same comparison can be done between the muon spectrometer and the fibre tracker momentum for ν_μ CC events data. Although the central parts of distributions of $\frac{P_{measured}-P_{simulated}}{P_{measured}}$ for the muon spectrometer are Gaussian, these distributions also exhibit large non Gaussian tails. Worse resolution is for instance obtained near the edges of the detector and for large angle tracks. The events in the tails are eliminated using a quality classification of the fits discussed in [V.4], taking into account among others of the impact point and the length of the tracks. The tracks chosen in the fibre tracker are such that the fit has a probability greater than .5%, the number of possible combinations of hits downstream of the magnet is low (<20) and that the 2 DT1 paddles and at least 3 out of the DT2 and DT3 paddles are hit.

2.1 Simulated events.

Using simulated events, we can compare the momenta reconstructed by the fibre trackers and the muon spectrometer both to the true (simulated) values and to each other as done for data as shown in figure V.13. The obtained resolution for the fibre tracker momentum is:

$$\frac{\sigma(p)}{p} = (0.20 \pm 0.06) \oplus (0.033 \pm 0.004) \times p \qquad \text{(V.7)}$$

The resolution for the muon spectrometer momentum corrected for the energy loss in the calorimeter is:

$$\begin{aligned} \frac{\sigma(p)}{p} &= 0.08 \pm 0.02 \text{ for the range measurement} \\ \frac{\sigma(p)}{p} &= 0.13 \pm 0.01 \text{ for the bending measurement} \end{aligned} \quad \text{(V.8)}$$

These resolutions are in agreement with what one would expect from the muon-spectrometer [V.4] and the resolution found in the fibre trackers for single muons.

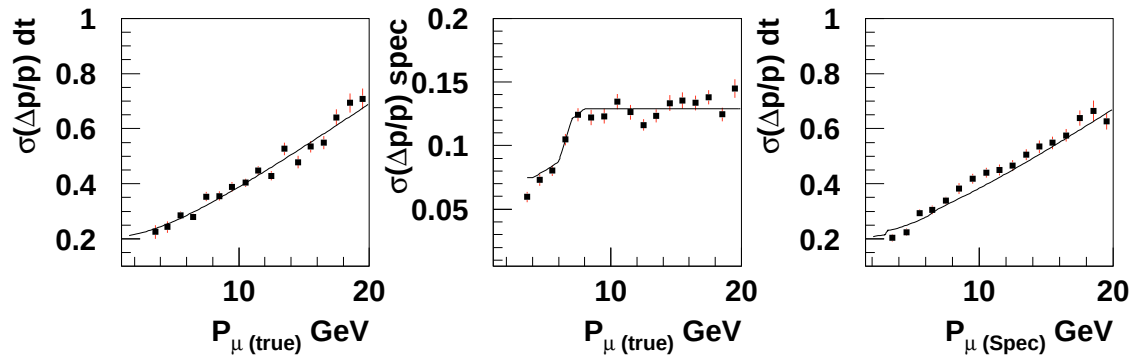

Figure V.13: *Momentum resolution for muons coming from simulated ν_μ interactions. Each dot represents the sigma of the distributions of $\frac{P_{measured}-P_{reference}}{P_{measured}}$ in bins of $P_{reference}$. Left : The momentum measured in the air-core magnet is compared to the true (simulated) momentum. Centre : The muon spectrometer momentum corrected for the energy loss in the calorimeter is compared to the true momentum. Right: The momentum measured in the air-core magnet is compared to the muon spectrometer momentum corrected for the energy loss in the calorimeter. The lines show the result of a fit to the data (left and centre plots), and the quadratic combination of the 2 fits (the right plot).*

The fraction of tracks reconstructed with the wrong sign of the charge as a function of the true momentum is shown in figure V.14 along with the fraction of tracks reconstructed with the opposite sign of the charge with respect to the charge reconstructed in the muon spectrometer.

2.2 Data

The fibre tracker momentum resolution is obtained comparing directly the momentum reconstructed in the muon spectrometer with the momentum reconstructed in the fibre trackers. The fibre tracker resolution is fitted for fixed values of the spectrometer range and bending resolutions 0.07 and 0.16 respectively (values from [V.4]):

$$\frac{\sigma(p)}{p} = (0.26 \pm 0.04) \oplus (0.039 \pm 0.002) \times p \quad \text{(V.9)}$$

The data and the results of the fit are shown in figure V.15. This result is in agreement with what was obtained for the single muon tracks.

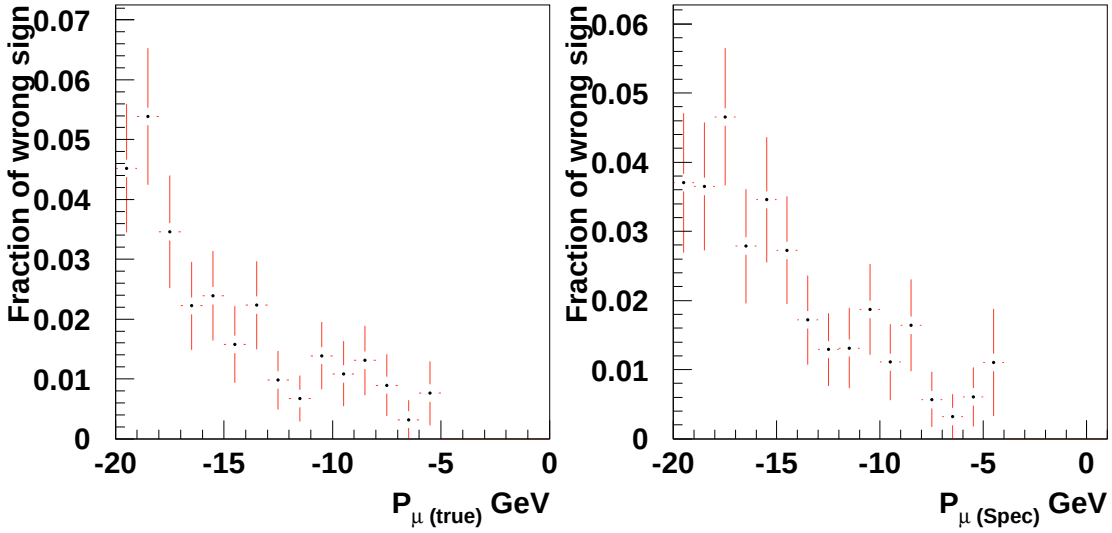

Figure V.14: *Fraction of muon tracks reconstructed with the opposite sign of charge in the diamond tracker with respect to the muon spectrometer reconstructed charge (Right) and the true charge (Left) as a function of the muon momentum multiplied by the charge attributed by the spectrometer (Right) or the true charge (Left).*

Using different muon spectrometer resolutions (from .07 to .10 for the range measurement and from .14 to .19 for the bending measurement) yields fibre momentum resolution fits within .01 for the multiple scattering contribution and within .001 for the fibre tracker resolution of the above values.

Although compatible at the level of one standard deviation with the resolution of .22 obtained for simulated events, the constant term in the fibre tracker momentum resolution is systematically slightly larger in real data. Several effects which could cause such a deviation are listed below:

- There could be more material in the detector than is accounted for in the simulation. The simple simulation shows that one needs to add 8% of a radiation length (e.g.: 7.1 mm of aluminium) to increase the constant term from .22 to .26. It is, however, certain that such a large amount of extra material is not present in the detector.

- A possible misalignment of the detector cannot account for this effect as misalignment would affect high momentum bins more than low momentum bins: the magnetic deflection is larger for low momentum particles.

- Another possibility lies in the fact that the resolution of the muon spectrometer can have tails, part of which might not completely be reproduced by the simulation, such that the track quality choice would not completely reject them for real data. Since such tails would not be taken into account in the assumed muon spectrometer resolution, they would artificially increase the fitted constant term.

The fraction of tracks with a different sign attributed in the fibre trackers and in the

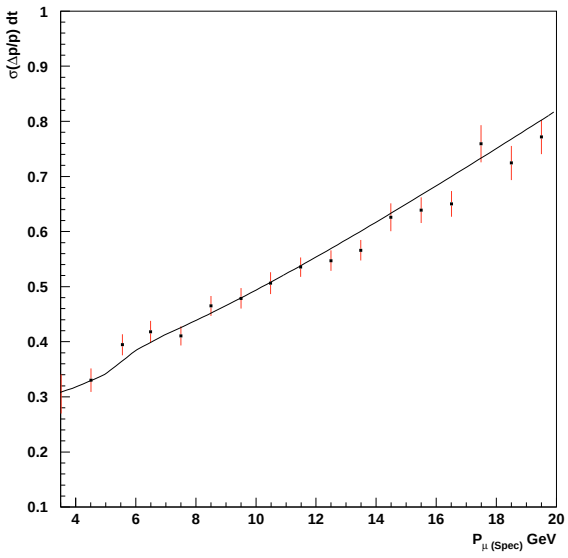

Figure V.15: *Momentum resolution for muons from neutrino CC interactions : the momentum measured in the air-core magnet is compared to the muon spectrometer momentum corrected for the energy loss in the calorimeter. Each dot represents the sigma of the distributions of* $\frac{P_{fibre}-P_{spec}}{P_{fibre}}$ *in bins of* P_{spec}*. The curve shows the combined resolution of the two spectrometers, the errors are statistical.*

muon spectrometer as a function of the muon spectrometer momentum is shown in figure V.16. This plot shows a worse sign of charge reconstruction efficiency for real data muon tracks than for simulated events in agreement with the respective resolutions. Figure V.17 shows that the momentum reconstruction is unbiased, both for the muon spectrometer and for pions of known momentum taken during a testbeam exposure. The data show no momentum dependence and the fit of a constant through the points at different momenta gives :

$$\frac{P_{fibre} - P_{reference}}{P_{reference}} = -0.06 \pm 0.06 \qquad \text{(V.10)}$$

compatible with the absence of bias.

3 Conclusion.

Although the observed momentum resolution is much worse than the one predicted in the proposal:

$$\frac{\sigma(p)}{p} = 0.16 \oplus 0.016 \times p \qquad \text{(V.11)}$$

the discrepency can be understood by the following effects:

- some material was added that had not been foreseen or accounted for at the time of the proposal : this accounts for the increase in the constant term, coming from multiple scattering to 0.21.

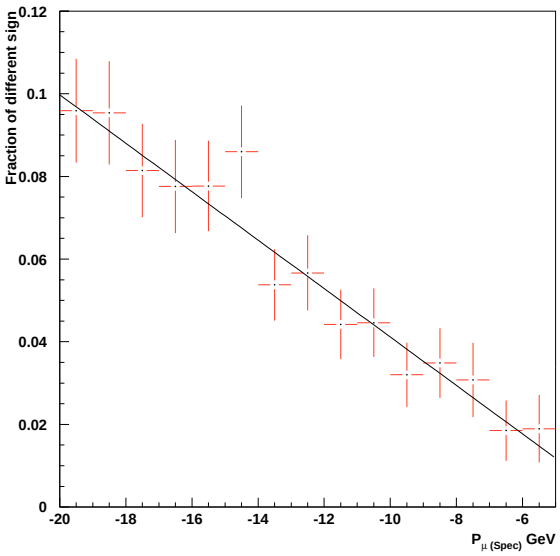

Figure V.16: *Fraction of tracks which get attributed a different charge in the muon spectrometer and in the fibre trackers as a funtion of the muon spectrometer momentum corrected for the energy loss in the calorimeter (the sign is the charge attributed in the muon spectrometer).*

- the intrinsic fibre tracker resolution had been estimated with a resolution per fibre plane of 140 μm rather than the actual 180 μm . Using the correct value, a contribution of $0.027 \times p$ would have been foreseen.
- the artificial splitting of physical track elements further degrades the intrinsic resolution as shown in the previous sections.

The cuts for the selection of the fibre tracker tracks used to estimate the resolution reduces the sample of tracks to about 60% of the initial sample of muon tracks with reconstructed fibre tracker momentum. Without these cuts, the obtained resolution is worse; the extra tracks have less information (planes hit) and are located in a crowded part of the detector, which makes tracking more difficult. The overall obtained resolution without any other cut than on the probability of the fit is given below:

$$\frac{\sigma(p)}{p} = (0.22 \pm 0.06) \oplus (0.035 \pm 0.004) \times p \text{ (for simulated events)} \quad \text{(V.12)}$$

$$\frac{\sigma(p)}{p} = (0.29 \pm 0.05) \oplus (0.044 \pm 0.003) \times p \text{ (for real events)} \quad \text{(V.13)}$$

When calculating efficiencies or background contamination for the oscillation signal, the reconstructed momenta in simulated events will need to be smeared to reproduce the resolution and efficiency for reconstructing the correct charge as observed in the data.

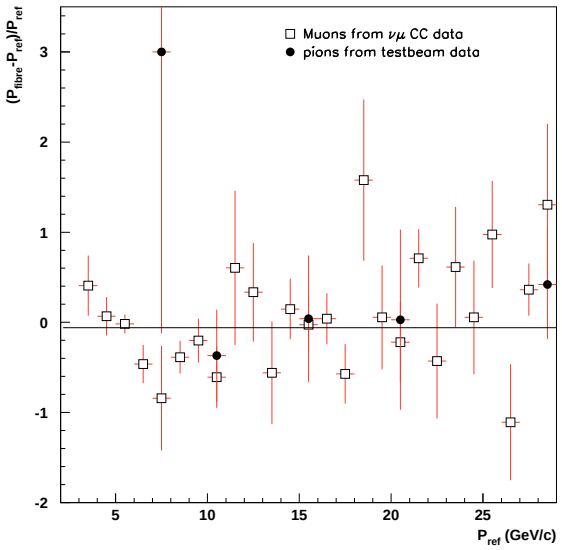

Figure V.17: *Momentum bias as a function of the reference momentum. The empty squares represent ν_μ CC data, the reference momentum P_{ref} is the momentum measured in the muon spectrometer corrected for the energy loss in the calorimeter. The black disks represent pions taken during a testbeam exposure, P_{ref} is the set momentum of the beam. The straight line is the result of the fit of a constant through the data:-0.06$\pm$0.06, compatible with the absence of bias or momentum dependence.*

References

[V.1] M. Vander Donckt, Chorus Internal Note 96021, 1996.

[V.2] G. Piredda and P. Righini, Chorus Internal Note 96020, 1996.

[V.3] P. Zucchelli, PhD. Thesis, Universita degli Studi di Ferrara, 1995.

[V.4] A. Artamonov, P.Gorbounov, Chorus Internal Note 97029, 1998.

Chapter VI Neutrino oscillation search analysis.

A Introduction

This chapter describes the CHORUS analysis procedure to look for τ^- decay candidates, and then extracts a limit on the oscillation parameters as no event has been observed within the data sample analysed.

The CHORUS analysis divides the events in 2 samples : the events with an identified muon (1-μ sample) and the events without a muon (0-μ sample).

The first sample is composed mainly of ν_μ CC events with a small contamination of NC events with a π or K decay. These events are used in the search for τ^- decay into a muon. This sample was chosen to train and improve both on the electronic detector reconstruction algorithms and on the emulsion scanning methods: the muon is the only track which is needed to check whether or not the event is a possible ν_τ interaction candidate. It is easier to reconstruct as it is more isolated than the hadronic shower tracks, and traverses the whole detector.

The 0-μ sample is composed of ν_μ NC interactions, with a contamination from CC events with an unidentified muon. It is analysed in the search for τ^- decay to one or three charged hadrons and to a smaller extent to electrons, but also contributes to the sensitivity to the muonic decay of the τ^- .

The two analyses will be described both using events from the full detector GEANT Monte Carlo simulation and the data from the electronic detector which have been scanned so far.

B The Monte Carlo sample.

The acceptance of the event reconstruction and prediction algorithms in the electronic detector is one of the ingredients necessary to work out a limit on the neutrino oscillations parameters. A full GEANT Monte Carlo simulation of the CHORUS detector is used to get a handle on these numbers. The results are compared to the data whenever possible. The following samples were used : NC ν_μ interactions, CC ν_μ interactions and ν_τ CC interactions. In addition, samples of ν_μ and $\bar{\nu}_\mu$ interactions with production of a charged charm hadron were dedicated to background studies. The quasi-elastic and resonant interactions (QE) and deep inelastic scattering (DIS) interactions are generated using two separate primary event generator programs, the event samples of both types contribute to the overall results according to the flux weighted cross-sections prescribed by S. Ricciardi

in [VI.1], and of the trigger efficiencies for each sample as shown in table 6.1.

$$\begin{aligned} \left\langle \frac{\sigma_{QE}}{\sigma_{DIS}} \right\rangle_{\nu_\mu\ NC} &= 10.1\% \\ \left\langle \frac{\sigma_{QE}}{\sigma_{DIS}} \right\rangle_{\nu_\mu\ CC} &= 8.5\% \\ \left\langle \frac{\sigma_{QE}}{\sigma_{DIS}} \right\rangle_{\nu_\tau\ CC} &= 13.4\% \end{aligned} \qquad \text{(VI.1)}$$

Event type	ν_μ DIS NC	ν_μ QE NC	ν_τ DIS non-muonic decay	ν_τ QE non-muonic decay
Trigger efficiency	90.1±0.3%	19.8±0.4%	99.85 ±0.04%	96.3±0.3%
Event type	ν_μ DIS CC	ν_μ QE CC	ν_τ DIS muonic decay	ν_τ QE muonic decay
Trigger efficiency	99.67±0.05%	99.2±0.2%	99.25±0.08%	92.5 ± 0.3%
Event type	ν_μ DIS CC $\rightarrow \bar{c}$+...		ν_μ DIS CC $\rightarrow c$+...	
Trigger efficiency	99.91±0.02%		99.984±0.005%	

Table 6.1: *Trigger efficiencies for events originating in the emulsion as estimated using simulated events. The errors are statistical.*

C Event reconstruction in the electronic detector.

The first step in the analysis is the reconstruction in the electronic detector. After the track finding has been performed in all subdetectors, and the tracks have been associated between the different subdetectors, the vertex of the event is calculated. If several choices are possible, the vertices are ordered according to weights attached to the tracks belonging to them. The more detectors the track is found in, the higher its weight.
The efficiency of the event reconstruction algorithms, and their ability to predict the vertex position in the emulsion stack where the interaction occurred can be estimated using the full GEANT Monte Carlo simulation of the CHORUS detector. The results of this study are shown in table 6.3(6.5) for NC (CC) ν_μ events and in tables 6.6 (6.4) for CC ν_τ interactions followed by a (non-)muonic decay of the tau. Tables 6.7 and 6.8 give the results obtained for ν_μ and $\bar{\nu}_\mu$ CC events in which a charged charmed hadron is produced and decays. Vertices can sometimes be wrongly attributed to a stack further downstream as shown in the tables 6.3 to 6.6: This effect is due to the complication of the event due to secondary interactions and multiple scattering in the material downstream of the interaction point. It is particularly important for events originating in the odd numbered emulsion stacks due to the geometry of the target region. Indeed, there is another emulsion stack between the most downstream 3 hyperplanes used by the TT track finding algorithm and the one just downstream of the stack of the vertex, which makes the track extrapolation more difficult and sometimes causes the vertex position to be predicted in the stack downstream of the correct one. The effect of the increasing complication of the events as they originate more and more upstream can also be seen as non-muonic events tend to be better reconstructed in module 2 of the TT rather than in module 1.

Table 6.2 shows the fraction of events predicted in an emulsion stack which really originated there. Once more we can see that an event predicted in an upstream stack is more likely to have really originated there, as the reconstruction when failing tends to reconstruct the vertex point more downstream than its correct position.

Event type	Stack 1	Stack 2	Stack 3	Stack 4
ν_μ CC	88.4%	83.4%	79.8%	81.2%
ν_μ NC	90.2%	80.1%	75.0%	69.4%
$\tau^- \rightarrow$ 1-μ	88.3%	84.1%	78.6%	81.0%
$\tau^- \rightarrow$ 0-μ	90.5%	82.5%	76.6%	74.8%

Table 6.2: *Percentage of the events reconstructed in an emulsion stack which were simulated there.*

reconstructed in stack	1	2	3	4	outside	failed
simulated in						
stack 1	61.7 %	5.2 %	1.1 %	2.7 %	16.2 %	13.1 %
stack 2	0.0%	75.8 %	1.5 %	3.2 %	6.6 %	13 %
stack 3	0.0%	0.0%	61.3 %	7.4 %	11.3 %	19.9 %
stack 4	0.0%	0.0%	0.0%	79 %	3.1 %	17.9 %
Outside	1.2 %	3.1 %	4.7 %	5.9 %	35.8 %	49.3 %
Events reconstructed in the correct stack						
Classified as 0-μ	97.6 %	97.6 %	97 %	97.1 %	-	-
Classified as 1-μ	2.4 %	2.4 %	3 %	2.9 %	-	-

Table 6.3: *Percentages of ν_μ events NC reconstructed in and outside the emulsion stacks as a function of where they were simulated. The 'outside' column (row) represents events simulated (reconstructed) in the fibres and support structures of the target area. Also shown is the percentage of events reconstructed in the correct emulsion stack which are classified as events with and without muon. The statistical error on these values is typically .5%*

reconstructed in stack	1	2	3	4	outside	failed
simulated in						
stack 1	64.8 %	6.2 %	1.3 %	1.2 %	22.8 %	3.7 %
stack 2	0.0%	81.6 %	1.4 %	4.2 %	9.2 %	3.6 %
stack 3	0.0%	0.0%	68.7 %	7.7 %	15.7 %	7.9 %
stack 4	0.1 %	0.0%	0.0%	89.3 %	3.8 %	6.8 %
Outside	1.1 %	3.3 %	5.4 %	6.7 %	40.2 %	43.2 %
Events reconstructed in the correct stack						
Classified as 0-μ	97.0 %	96.8 %	97.4 %	96.9 %	-	-
Classified as 1-μ	3.0 %	3.2 %	2.6 %	3.1 %	-	-

Table 6.4: *Percentages of ν_τ CC events with a non muonic decay of the τ^- reconstructed in and outside the emulsion stacks as a function of where they were simulated. The 'outside' column (row) represents events simulated (reconstructed) in the fibres and support structures of the target area. Also shown is the percentage of events reconstructed in the correct emulsion stack which are classified as events with and without muon. The statistical error on these values is typically .5%*

reconstructed in stack	1	2	3	4	outside	failed
simulated in						
stack 1	95.6 %	0.3 %	0.0%	0.0%	3.8 %	0.2 %
stack 2	0.0%	98.9 %	0.0%	0.1 %	0.9 %	0.1 %
stack 3	0.0%	0.0%	95.6 %	0.5 %	2.7 %	1.2 %
stack 4	0.0%	0.0%	0.0%	97.8 %	0.8 %	1.4 %
Outside	3.1 %	5 %	6.1 %	5.3 %	44.3 %	36.2 %
Events reconstructed in the correct stack						
Classified as 0-μ	5.6 %	5.4 %	5.8 %	5.1 %	-	-
Classified as 1-μ	94.4 %	94.6 %	94.2 %	94.9 %	-	-

Table 6.5: *Percentages of ν_μ CC events reconstructed in and outside the emulsion stacks as a function of where they were simulated. The 'outside' column (row) represents events simulated (reconstructed) in the fibres and support structures of the target area. Also shown is the percentage of events reconstructed in the correct emulsion stack which are classified as events with and without muon. The statistical error on these values is typically .5%*

reconstructed in stack	1	2	3	4	outside	failed
simulated in						
stack 1	94 %	0.6 %	0.2 %	0.1 %	4.1 %	1.1 %
stack 2	0.0%	97.7 %	0.2 %	0.3 %	0.9 %	0.9 %
stack 3	0.0%	0.0%	92.1 %	1 %	3.3 %	3.6 %
stack 4	0.0%	0.0%	0.0%	96.3 %	1.1 %	2.5 %
Outside	2.8 %	4.6 %	5.9 %	5.3 %	43.7 %	37.6 %
Events reconstructed in the correct stack						
Classified as 0-μ	11.6 %	12.1 %	11.9 %	11.5 %	-	-
Classified as 1-μ	88.4 %	87.9 %	88.1 %	88.5 %	-	-

Table 6.6: *Percentages of ν_τ CC events with a muonic decay of the τ^- reconstructed in and outside the emulsion stacks as a function of where they were simulated. The 'outside' column (row) represents events simulated (reconstructed) in the fibres and support structures of the target area. Also shown is the percentage of events reconstructed in the correct emulsion stack which are classified as events with and without muon. The statistical error on these values is typically .5%*

reconstructed in stack	1	2	3	4	outside	failed
simulated in						
stack 1	91.7 %	0.6 %	0.0%	0.0%	7.5 %	0.2 %
stack 2	0.1 %	98.4 %	0.0%	0.0%	1.4 %	0.1 %
stack 3	0.0%	0.0%	92.4 %	0.9 %	6.1 %	0.6 %
stack 4	0.0%	0.0%	0.1 %	98.1 %	1.5 %	0.4 %
Outside	1.4 %	3.2 %	4.8 %	3.8 %	48.7 %	38 %
Events reconstructed in the correct stack						
Classified as 0-μ	10.4 %	9.4 %	11 %	9.2 %	-	-
Classified as $\geq$ 1-μ	89.6 %	90.6 %	89 %	90.8 %	-	-

Table 6.7: *Percentages of ν_μ DIS CC events with charged charmed hadron production reconstructed in and outside the emulsion stacks as a function of where they were simulated. The 'outside' column (row) represents events simulated (reconstructed) in the fibres and support structures of the target area. Also shown is the percentage of events reconstructed in the correct emulsion stack which are classified as events with and without muon. The statistical error on these values is typically .5%*

reconstructed in stack	1	2	3	4	outside	failed
simulated in						
stack 1	87.6 %	0.7 %	0.0%	0.0%	11.4 %	0.2 %
stack 2	0.0%	97.5 %	0.0%	0.0%	2.3 %	0.1 %
stack 3	0.0%	0.0%	89.4 %	1.2 %	9.1 %	0.4 %
stack 4	0.0%	0.0%	0.1 %	96.9 %	2.8 %	0.3 %
Outside	4.2 %	4 %	11.1 %	10.4 %	55.3 %	15 %
Events reconstructed in the correct stack						
Classified as 0-μ	6.0 %	5.2 %	6.5 %	5.1 %	-	-
Classified as $\geq$ 1-μ	94.0 %	94.8 %	93.5 %	94.9 %	-	-

Table 6.8: *Percentages of $\bar{\nu}_\mu$ DIS CC events with charged charmed hadron production reconstructed in and outside the emulsion stacks as a function of where they were simulated. The 'outside' column (row) represents events simulated (reconstructed) in the fibres and support structures of the target area. Also shown is the percentage of events reconstructed in the correct emulsion stack which are classified as events with and without muon. The statistical error on these values is typically .5%*

D Event selection.

The negatively charged tracks from the predicted events are selected for automatic scanning if their momentum is lower than 30 GeV/c* and they are identified as a muon or if their momentum is between 1 and 20 GeV/c for hadrons and electrons.
In addition, muon tracks from events containing 2 muons are scanned to cross-check with charm decays the efficiency to find τ^- -decay topologies.
The momentum resolution for non-muon tracks in simulated events was checked to be consistent with the resolution obtained for muons, both in the ν_μ and ν_τ induced events samples. The percentage of events reconstructed in the right stack which are selected for scanning according to the criteria described above is shown in table 6.9. For the ν_τ induced events, the numbers only refer to the fraction of events in which the τ^- daughter is selected as possible scan back track. For ν_μ ($\bar{\nu}_\mu$) charm production, the numbers only refer to the fraction of events in which the charmed hadron daughter is selected as possible scan back track, and the primary μ^- (μ^+) is not identified. Even if a few percent of 0-μ and 1-μ events are classified in the wrong category, they can also be chosen for scanning if they satisfy the selection criterion of the other category. The Monte Carlo momentum resolution was degraded to reproduce the resolution measured in the data, as discussed in the previous chapter. A difference larger than 1σ could only be observed in the selection efficiency of events classified as 0-μ as could be expected from the fact that most muons are reconstructed in the muon spectrometer. This study shows that to reproduce the momentum reconstruction observed in the data, the reconstruction acceptances will have

*Muons reconstructed in the muon spectrometer are selected if their measured momentum is less than 28 GeV/c, as they lose slightly less than 2 GeV/c when they traverse the calorimeter.

Monte Carlo	standard	smeared	standard and smeared
Event type	selected as 0-μ		selected as 1-μ
ν_μ CC	44±1%	50±1 %	66.0±0.3%
ν_μ NC	40 ±1%		34±6%
$\nu_\tau \rightarrow$ 1-μ	24±1%		74.3±0.6%
$\nu_\tau \rightarrow$ 0-μ	40.5±0.5%	44.1±0.5%	33±2%
ν_μ c production	21±1%		0.34±0.07%
$\bar{\nu}_\mu$ $\bar{c}$ production	34±2%		0.54±0.06%

Table 6.9: *Percentage of events reconstructed in the stack where they were simulated and classified as 0 or 1-μ (in the proportions given in the tables 6.3 to 6.8) which satisfy the momentum criteria to be sent to the scanning, with or without smearing the Monte Carlo to reproduce the momentum resolution observed in the data. The columns are distinct only if the difference is larger than the 3σ error.*

to be multiplied by the factors below :

$$A^{smeared}_{\tau \rightarrow\ 0-\mu} = 1.09 \times A^{standard}_{\tau \rightarrow\ 0-\mu} \quad \text{(VI.2)}$$

$$A^{\nu_\mu\ CC\ smeared}_{0-\mu} = 1.14 \times A^{\nu_\mu\ CC\ standard}_{0-\mu} \quad \text{(VI.3)}$$

E Scanning.

Within this total sample of tracks, only the tracks with an angle less that 400 mrad from the beam direction and greater than 50 mrad with respect to the X7 calibration beam directions are selected. The first angular cut is due to the limitations of the scanning hardware. The second angular cut is to avoid picking up in the emulsion background track candidates coming from the X7 test beam.
Table 6.10 gives the acceptances for the different event categories to be sent to the scanning procedure. One can notice that the only effect of the momentum smearing is to increase slightly the number of predicted signal events.

The predicted tracks from a full data-taking period are ordered by half emulsion modules, corresponding to the physical unit of emulsion scanned set on a microscope. A data-taking period can be as short as 3 weeks when scanning the first interface sheet, the CS, to 2 years when scanning the target emulsion. Figure VI.1 shows the division of an emulsion plate into modules. Although each half-module has transverse dimensions of $36 \times 36 cm^2$, only the central $34 \times 34 cm^2$ area defines the scanning fiducial volume.

1 The Track Selector.

The automatic scanning is done using a system called the Track Selector(TS) [VI.2], continuously developed in Nagoya. The speed of this system has improved by a factor 10 since the proposal of the experiment reaching an analysis speed of 100 events per day per system, and another factor of 30 is expected from the new prototypes currently being

Event type / Stack	1	2	3	4
ν_μ CC	0.58	0.61	0.59	0.62
ν_μ NC	0.21	0.27	0.31	0.37
$\nu_\tau \rightarrow$ 1-μ	0.58	0.60	0.56	0.60
$\nu_\tau \rightarrow$ 0-μ	0.21 (0.24)	0.29 (0.34)	0.28 (0.31)	0.40 (0.42)

Table 6.10: *Global reconstruction acceptances for events simulated in the 4 emulsion stacks. These numbers represent the fraction of events simulated in each stack which contain at least one track satisfying the momentum and angular cuts. The numbers between brackets are the ones obtained with the smeared Monte Carlo - only quoted when they are different from the standard Monte Carlo .*

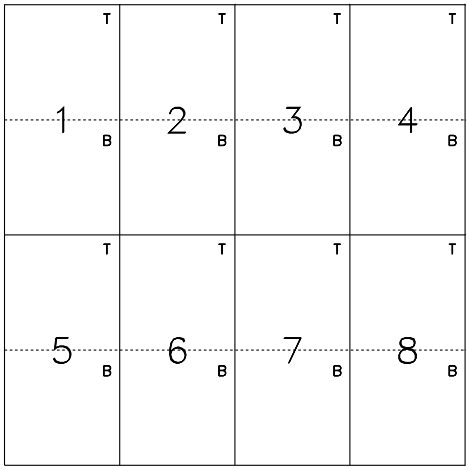

Figure VI.1: *Numbering scheme of the emulsion modules. Each module is 36 cm wide and 72 cm high.*

designed. For each predicted track, the TS focuses at 16 different depths in the emulsion sheet for a total depth of 100 μm and collects and digitises the image using a CCD camera and a video processor as shown in figure VI.2. The images are then shifted according to the track angle and added. The signal of the predicted track can then be seen as a peak in the pulseheight distribution as depicted in figure VI.3. A track is considered found if a pulseheight corresponding to 12 grains is collected in the 16 layers. The TS finding efficiency drops as the angle increases as shown in figure VI.4.

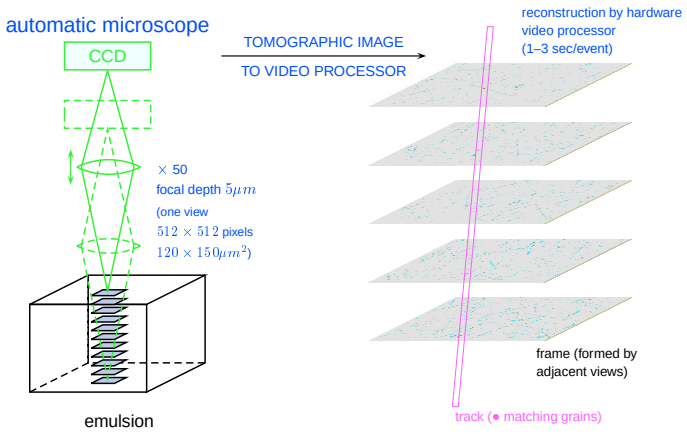

Figure VI.2: *Schematic representation of the automatic microscope data-taking system in Nagoya.*

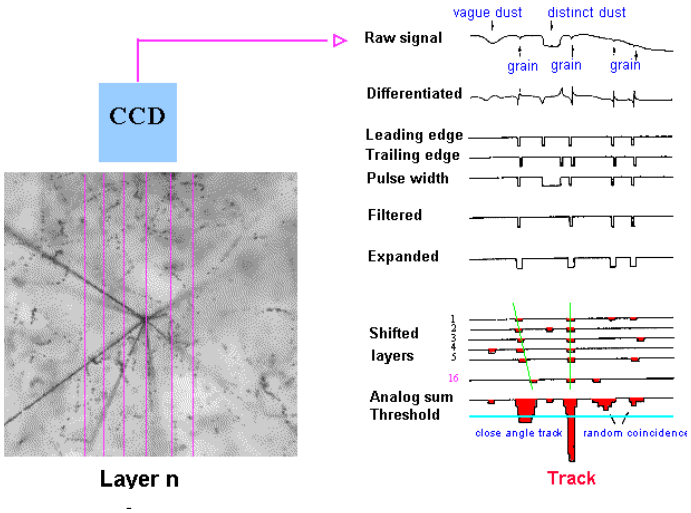

Figure VI.3: *Schematic representation of the image processing done by the Track Selector to find the signal associated to predicted tracks.*

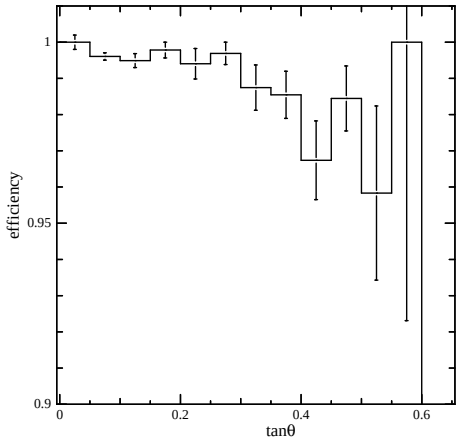

Figure VI.4: *Track Selector Track finding efficiency as a function of the track slope with respect to the beam direction.*

2 The Strategy.

Event location

The predictions are searched for automatically in the CS plate. A track found in the CS plate is said to match a prediction if if its angle in the emulsion differs by less than 15 mrad from the predicted angle and its position is within 9×9 microscope views[†] (or 11×11 for data after 94, but then the scanning is done by spiralling around the predicted position and stopping as soon as a candidate makes an angle difference of less than 6 mrad with the prediction. If no such match is found, all candidates in the area scanned with $\Delta\theta$ <15 mrad are considered.)
A track found in the CS is then followed in the SS, using the position found in the CS. It will be found if it is within the 7×7 microscope views centred on the prediction and if its angle differs by less than 15 mrad from the predicted angle. Th e scanning is done spiralling outwards as described for the CS for data after 1994. The SS angle becomes the reference for the scanning of the target emulsion.
The efficiencies for CS and SS scanning have been estimated using the data themselves [VI.3], the GEANT Monte Carlo [VI.4] with no background such as X7 tracks, Compton electrons, cosmic rays, etc..), and a method to retrieve the background free efficiency from the efficiency observed in the data and the number of candidates found per track in the scanned area[VI.8]. The tracks are separated into 7 priority categories designed by O. Sato and described in table 6.11.

The results obtained by various methods range from 50 to 85 % for the CS track finding efficiency depending on the event type, the track category, the stack number and on the scanning strategy. The efficiencies found by the different methods vary for a same track category by about 10%, such that it will be one of the main contributions to the systematic error in the final result. The finding efficiency in the SS is more stable as the efficiency does

[†]1 view=120μm ×90μm at the magnification 50 used.

Category	Description	angle with respect to the X axis
1	muon tracked through the whole detector	$\theta < 0.2$ rad
2	muon tracked through the whole detector	$0.2 < \theta < 0.4$ rad
3	track measured in TT and one of the spectrometers	$\theta < 0.2$ rad
4	track measured in TT and one of the spectrometers	$0.2 < \theta < 0.4$ rad
5	track measured in TT only	$\theta < 0.2$ rad
6	track measured in TT only	$0.2 < \theta < 0.4$ rad
7	track from 1$\rightarrow$ 6 badly isolated in TT, with a bad χ^2 for the TT fit, with $\theta > 0.4$ rad or an angle with respect to X7 <80 mrad.	

Table 6.11: *Priority classification of tracks for scanning. The smaller the number, the better the track quality and the chance the track will be found, such that in scanning periods when not all the selected tracks were scanned, the track(s) scanned where the ones with the lowest category number.*

not depend on the quality of TT prediction (which can be better for Monte Carlo than for the data) but only on the scanning strategy as the prediction is based on a genuine CS emulsion track. The various estimates give values around 90($\pm$3)%

A track which has been found in the interface sheets is then followed upstream plate by plate in the target emulsion, using only the most upstream 100μm of each plate until the track selector looses the track for 2 successive plates as shown in figure VI.5. The prediction of the track position from plate n to plate n+1 is done using the found position in plate n and the angle found in the SS. The region around the predicted point in which the track will be found in the plate n+1 has a radius of $15 + 50 \times \Delta\theta_{X7}$(rad) μm in position and the angular tolerance is of $25 + 50 \times \Delta\theta_{X7}$(rad) mrad, where $\Delta\theta_{X7}$ is the angle difference with the X7 test beam direction. The plate to plate finding efficiency is 98% , most of the inefficiency being due to local surface defects of the emulsion plate.

The first plate in which the track was not found is called the vertex plate n_{vx} as it is supposed to contain the neutrino interaction vertex, or a decay (or secondary interaction) vertex if there was a large angle between the parent and daughter particle. The three most downstream plates are only used to validate the track found in the SS, and are not considered for vertex analysis.

The efficiency of the complete vertex scan-back procedure is of 32% and 42% for hadron and muon tracks respectively, including the CS (main difference) and SS finding efficiencies. This reflects the worse reconstruction quality of shower particles with respect to the muons, as they have on average a lower momentum and a worse isolation from other tracks.

Vertex analysis and kink finding

Once the vertex plate is defined, various methods have been tried and used to analyse automatically the decay topology and reject non-interesting events while keeping potential candidates for further checks, this time done manually.

The emulsion plate in which a τ^- decays can either be the plate where the primary

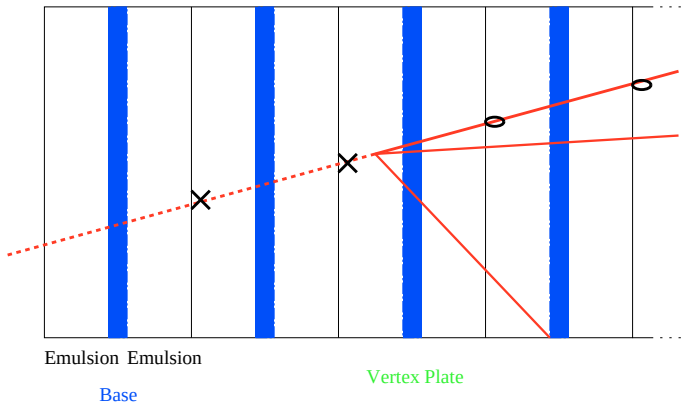

Figure VI.5: *Illustration of the scan-back procedure. The track is followed from the most downstream plate (right), looking only at the most upstream 100 μm , until it is missed in two successive plates.*

interaction took place (it is then called a short decay) or a plate further downstream (so-called long decay). For all events these two possibilities have to be checked.

The long decay possibility is further divided into two possibilities for which two different search methods are adopted: either the angle of the decay was within the angular acceptance of the scan-back procedure and the vertex plate is the primary interaction plate, or the angle was larger and the vertex plate is in fact the decay plate. The three searches applied to each event are described below:

1. Short decays:(34% of the simulated τ^- decays) If an event contains more than one track, the other predicted tracks are searched for in the upstream surface of the plate n-1. The impact parameter (IP) between the scan-back track and t he vertex made by the other tracks of the event is calculated. A cut on the maximum distance depending on the depth of the vertex in the emulsion was chosen to select τ^- decay candidates in the vertex plate and to reject ν_μ events. It is defined in equation VI.4, where X_d and X_{vx} are the positions along the beam of the downstream surface of the emulsion plate and of the reconstructed vertex. This method is illustrated in figure VI.6.

$$IP > 2 + 0.006 \times (X_d - X_{vx})\mu\text{m} \qquad \text{(VI.4)}$$

Events satisfying equation VI.4, are checked manually for an actual decay kink. Upon finding, the transverse momentum associated to the decay angle and the measured daughter momentum would have been checked to be in excess of 250 MeV/c to reject pion and kaon decays.
Events where the vertex cannot be reconstructed are analysed using the video image analysis described in 3.

2. Long, small angle decays:(6% of the simulated τ^- decays) If the τ^- decayed in a plate downstream of the vertex plate, making a small angle with its daughter particle such

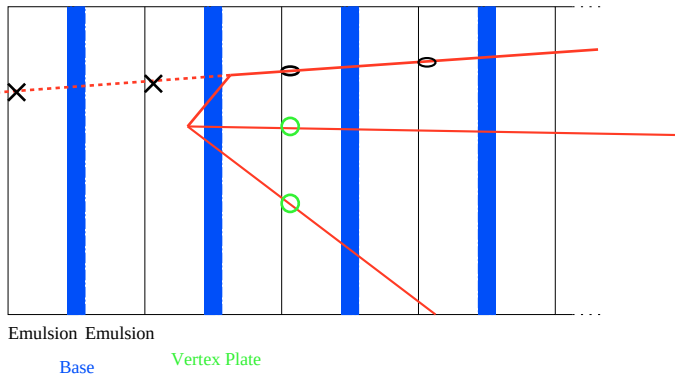

Figure VI.6: *Illustration of the search for a τ^- decay in the same plate as the primary ν_τ interaction vertex.*

that it was followed down within the tolerance of the TS to the primary interaction plate n-1 as shown in figure VI.7. To test this hypothesis, the angle between the scan-back track and another track of the event is calculated at the vertex plate θ_{vx} and in TT θ_{TT} or at the SS (for the tracks used for scan-back). If the corresponding transverse momentum :$(|\theta_{vx} - \theta_{TT}|) \times p_{scan-back}$ is larger than 250 MeV/c, the scan-back track is manually followed downstream for 5 plates (3 for hadrons), to detect the presence of a decay kink.

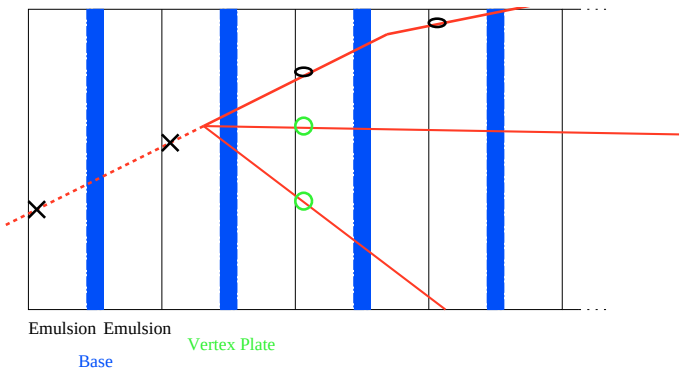

Figure VI.7: *Illustration of the search for a τ^- decay in a plate further downstream of the vertex plate, if the τ^- daughter particle has a small angle with respect to the τ^- .*

3. Long, large angle decays: (60% of the simulated τ^- decays) In this case the angle between the τ^- and its daughter is large enough for the T.S. not to find the τ^- track in the next plates. Since the vertex plate is not the primary interaction plate, the other predicted TT tracks will not be found in the plate as illustrated in figure VI.8.
   Two different methods have been applied to search for this class of decays : the Video Image analysis and the Parent Track search.

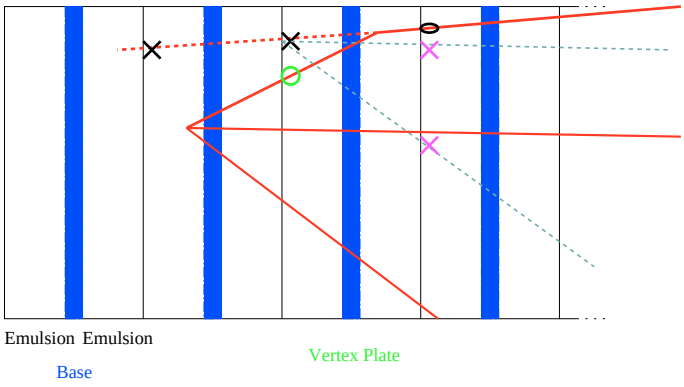

Figure VI.8: *Illustration of the search for a τ^- decay in the vertex plate, if the τ^- daughter particle makes a large enough angle with respect to the τ^- , for the scanning to stop in the decay plate.*

- **The Video Image analysis**: it consists in digitising the vertex plate, by taking 48 CCD images at 7μm spaced depths on each surface, centring the microscope view on the scan-back track impact point in the base of the emulsion. The images are then analysed offline by software. This method was only used for the 1994 data sample. Its main drawback is that decays occurring within 50 μm of the plastic base or of the downstream emulsion surface are not detected, and that the algorithm has a very low efficiency for kink angles larger than 150 mrad. The tracking efficiency of the V.I. algorithm itself is estimated to be 92% [VI.7]. A manual check is done if a kink is observed with a transverse momentum larger than 250 MeV/c, or if the track stops within the image with no visible nuclear breakup fragment.

- **The Parent Track search**: it consists in looking for a parent track in the upstream surface of the vertex plate, with closest approach distance to the scan-back track of $\leq 15\mu$m . The parent candidates are extrapolated and looked for in plate n-1. The candidates found in plate n-1 are rejected as background tracks. If a candidate remains the event is checked manually and the 250 MeV/c decay transverse momentum cut is applied if a kink topology is observed.

The overall kink finding efficiency varied as a function of the scanning strategy. Such that it will be different for 1994 data where video analysis was applied and all possible decays were searched for. For the next years, the parent track search was applied, and only long decays with large angles were searched for, so far as they represent the largest fraction of the decays. The values estimated by Monte Carlo simulation (see table 6.12 were experimentally checked using ν_μ N$\rightarrow$ μ^- D^+ X with a subsequent muonic decay of the D^+. Assuming a charm yield of about 5%, one expected 22.8$\pm$3.9 events in the 1994 and 1995 data sample and 25 were found.

F Background Estimates.

The possible sources of background were already discussed qualitatively in section III.B. The quantitative estimates are given below in terms of the number of events we would expect to see at this stage of the analysis.

1. Anticharm production: The anti-neutrino contamination (~5%) in the beam can give rise to negative charm meson production where

$$\frac{\langle\sigma_{\bar{\nu}CC}(D^-)\rangle}{\langle\sigma_{\nu CC}\rangle} = \frac{\langle\sigma_{\bar{\nu}CC}(D^-)\rangle}{\langle\sigma_{\bar{\nu}CC}(\bar{c})\rangle} \cdot \frac{\langle\sigma_{\bar{\nu}CC}(\bar{c})\rangle}{\langle\sigma_{\bar{\nu}CC}\rangle} \cdot \frac{\langle\sigma_{\bar{\nu}CC}\rangle}{\langle\sigma_{\nu CC}\rangle} = 0.30 \cdot 0.03 \cdot 0.44 = 0.4\% \quad \text{(VI.5)}$$

   which can fake a τ^- decay (BR($D^- \rightarrow h^-$) ~0.31, BR($D^- \rightarrow \mu^-$ or e^-) ~8%) if the primary lepton (e^+, μ^+) escapes identification (5.5%), and the decay kink is detected (21%). Such that we expect about 0.02 events in the present sample for the non-muonic decay channels and <0.1 events for the muonic decay channel.

2. Charm production: Positive charmed mesons created in ν_μ CC interaction

$$\frac{\langle\sigma_{\nu CC}(D^+)\rangle}{\langle\sigma_{\nu CC}\rangle} = \frac{\langle\sigma_{\nu CC}(D^+)\rangle}{\langle\sigma_{\nu CC}(c)\rangle} \frac{\langle\sigma_{\nu CC}(c)\rangle}{\langle\sigma_{\nu CC}\rangle} = 0.38 \cdot 0.05 = 0.019 \quad \text{(VI.6)}$$

   decay (BR($D^+ \rightarrow h^+$) ~0.31, BR($D^+ \rightarrow \mu^+$ or e^+) ~8%) and their daughter particle can be wrongly reconstructed as negative (10%). If the primary μ^- is not identified (11%), it can fake a τ^- decay. The fact that the D^+ daughter charge is wrong is strongly correlated with the cut on the decay transverse momentum P_t >250MeV/c, such that for these events, the kink finding efficiency is only 0.05, a factor of about 4 lower than for D^+ with correctly reconstructed charge. Approximately 0.03 events are expected from this source of background.

3. Associated charm production in neutral (0.13% [III.1]) and charged current events (<0.12%[III.1]), where the primary μ^- was missed and one of the charm particles is not detected. This source of background represents less than 0.01 events with the current statistics.

4. White star kink: this is the main source of potential background for the non-muonic decay channels of the τ^- . Indeed, a negative hadron can scatter off a nucleus and change direction, without leaving any trace of recoil, or Auger electron in the emulsion. An analysis of the existing KEK [VI.5] data has been performed in [VI.6]. The result is in agreement with the observation of 4 events with p_T >250 MeV/c at large distance from the primary vertex in the present CHORUS data sample, along the ≈92 m of hadronic scan back track, corresponding to a background of about 0.5 event within 3 plates from the primary.

G Limit on $\nu_\mu \rightarrow \nu_\tau$ oscillations

As no τ^- decay candidate event has been found up to now, one can set a limit in the (Δm^2 ,$\sin^2(2\theta)$) parameter space. Indeed the relation between the oscillation probability

P_{osc}, the efficiencies and the number of observed events can be written as :

$$\frac{N_\tau}{N_\mu} = \frac{Br(\tau \rightarrow x) \int\int \Phi_\mu \sigma_\tau A_\tau \eta_k P_{osc} dE dL}{\int\int \Phi_\mu \sigma_\mu A_\mu dE dL} \tag{VI.7}$$

Where the acceptances A, the kink finding efficiencies η_k, the neutrino CC cross-section σ,the fluxes Φ, and the oscillation probability P_{osc} depend on the neutrino energy E and all but Φ depend on the distance between the crea

tion and interaction point of the neutrinos L.
In the limit of large Δm^2 , $P_{osc} = \frac{1}{2}\sin^2 2\theta_\infty$, such that :

$$\frac{N_\tau}{N_\mu} = \frac{1}{2}\sin^2 2\theta_\infty \frac{Br(\tau \rightarrow x) \int\int \Phi_\mu \sigma_\tau A_\tau \eta_k dE dL}{\int\int \Phi_\mu \sigma_\mu A_\mu dE dL} \tag{VI.8}$$

Which can be rewritten as :

$$\frac{N_\tau}{N_\mu} = \frac{1}{2}\sin^2 2\theta_\infty Br(\tau \rightarrow x) \frac{\langle\sigma_\tau\rangle}{\langle\sigma_\mu\rangle} \frac{\langle A_\tau\rangle}{\langle A_\mu\rangle} \langle\eta_k\rangle \tag{VI.9}$$

Where the $\langle\sigma\rangle$'s are the flux-weighted CC cross-sections with $\frac{\langle\sigma_\tau\rangle}{\langle\sigma_\mu\rangle} = 0.53$, the $\langle A\rangle$'s are the flux and cross-section weighted acceptances and $\langle\eta_k\rangle$ is flux, cross-section and acceptance weighted kink finding efficiency. The boundary of the complete excluded region can be parametrised [VI.9] as:

$$\sin^2 2\theta(\Delta m^2) = \frac{1}{2}\sin^2 2\theta_\infty \frac{\int\int \Phi_\mu \sigma_\tau A_\tau \eta_k dE dL}{\int\int \Phi_\mu \sigma_\tau A_\tau \eta_k \sin^2(1.27 L/E\Delta m^2) dE dL} \tag{VI.10}$$

Such that the knowledge of $\sin^2 2\theta_\infty$ and the energy dependence of $\Phi_\mu \sigma_\tau A_\tau \eta_k$ are sufficient to determine the entire excluded region. The number of expected τ^- decays $N_{\tau i}$, where i represent the decay product (a (mis)identified muon, a hadron, an electron), can be expressed as :

$$N_{\tau i} = BR(\tau \rightarrow i) n_i P_{osc} \frac{\langle\sigma_\tau\rangle}{\langle\sigma_\mu\rangle} \frac{\langle A_{\tau i}\rangle}{\langle A_{\tau\mu}\rangle} \eta_{\tau i} \tag{VI.11}$$

Where the branching ratios are [II.5] :

$$\begin{aligned} BR(\tau^- \rightarrow \nu_\tau\ \bar{\nu}_\mu\ \mu^-) &= 17.37 \pm 0.09\% \\ BR(\tau^- \rightarrow \nu_\tau\ \bar{\nu}_e\ e^-) &= 17.81 \pm 0.07\% \\ BR(\tau^- \rightarrow \nu_\tau\ h^- n h^0) &= 49.52 \pm 0.16\% \end{aligned} \tag{VI.12}$$

Where n_i is the number of located CC ν_μ events N_μ for i=μ and N_μ times the relative fraction of the data for which 0-μ event analysis has been completed for the e^- ,h^-, and misidentified μ^- channel. The number of ν_τ events we can observe is divided into 2 samples from the start of the analysis : the CC events with a τ^- decay into an identified muon and the sample with other τ^- decay channels. The results of the events with and without muon

can be combined easily if we define a number of muon events equivalent to the 0-μ sample:

$$N_\mu^{eq} = N_{0-\mu} \sum_{i=h,e,\mu^{mis}} \frac{\langle A_{\tau i}\rangle}{\langle A_{\tau\mu}\rangle} \frac{\langle\eta_{\tau i}\rangle}{\langle\eta_{\tau\mu}\rangle} \frac{BR(\tau \rightarrow i)}{BR(\tau \rightarrow \mu)} \tag{VI.13}$$

Such that the 90% confidence level limit on the oscillation probability can be expressed as:

$$P_{osc} \leq \frac{2.38 \frac{\langle \sigma_\tau \rangle}{\langle \sigma_\mu \rangle} \frac{\langle A_{\tau\mu} \rangle}{\langle A_{\nu_\mu CC} \rangle}}{BR(\tau \rightarrow \mu) \eta_{\tau\mu} [N_\mu + N_\mu^{eq}]} \quad \text{(VI.14)}$$

The factor 2.38 takes into account the global 17% systematic error following the prescription given in [VI.11]. The sources of systematic as evaluated in [VI.8] :

- The Monte Carlo statistics ($\pm$1%) and reliability ($\pm$5%).
- The ratio of cross-sections ($\pm$7%)
- The momentum measurement by either spectrometers ($\sim \pm$5%).
- The track selector pulseheight cut (+5,-10%)
- The error on the impact parameter measurement (+19,-10% for the non-muonic decay channels, +9,-6% for the muonic decay channel)

The values of the acceptances and efficiencies are listed in table 6.12 along with the number of analysed events. No statistical errors are quoted as the overall systematic error is larger by an order of magnitude.

Data taking year	1994	1995	1996
Emulsion triggers	422 000	547 000	617 000
1-μ sample to be scanned	66 911	110 916	129 669
0-μ sample to be scanned	17 731	27 841	32 548
1-μ sample scanned up to now	42 154	49 912	129 669
0-μ sample scanned up to now	8 908	12 635	-
1-μ vertex located	18 286	20 642	30 128
0-μ vertex located	3 401	3 805	-
$\langle A_{\tau\mu} \rangle / \langle A_{\nu_\mu CC} \rangle$	0.93	0.93	0.93
$\langle A_{\tau\mu} \rangle$	0.39	0.39	0.39
$\langle A_{\tau h} \rangle$	0.18*	0.18*	-
$\langle A_{\tau e} \rangle$	0.010*	0.010*	-
$\left\langle A_{\tau\mu^{mis}} \right\rangle$	0.028*	0.028*	-
$\langle \eta_{\tau\mu} \rangle$	0.53	0.35	0.37
$\langle \eta_{\tau h} \rangle$	0.24	0.25	-
$\langle \eta_{\tau e} \rangle$	0.12	0.13	-
$\left\langle \eta_{\tau\mu^{mis}} \right\rangle$	0.22	0.23	-
N_μ^{equiv}	13 066*	13 890*	-

Table 6.12: *Status of the analysis as of July 1998 [VI.10], values of the acceptances and the kink finding efficiencies for the different event types. The numbers marked with a * are modified with respect to the published values to include the effect of the momentum resolution smearing.*

The overall result is thus given by:

$$P_{osc} \leq 5.8 \cdot \ 10^{-4} \quad \text{at 90 \% C.L.} \tag{VI.15}$$

Such that the 90% C.L. excluded region is shown in figure VI.9

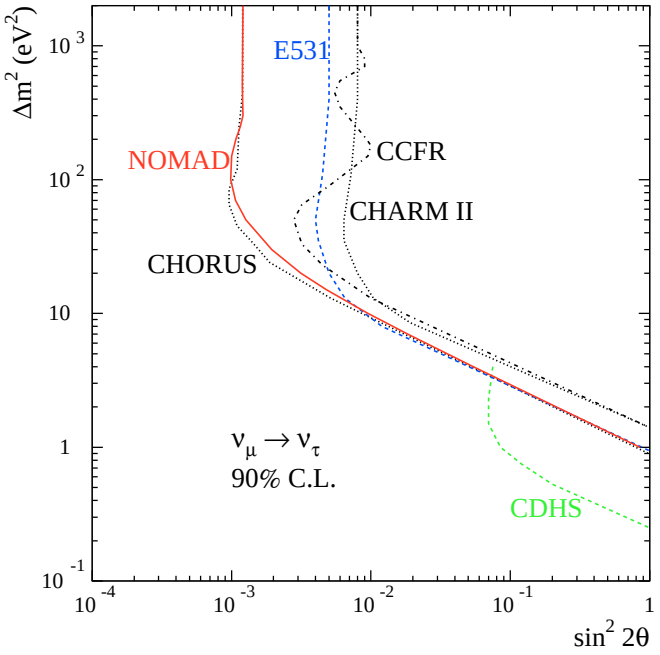

Figure VI.9: *Exclusion plot for the CHORUS experiment, using the data scanned up to July 1998. Also shown are the results from NOMAD[II.54] and previous experiments.*

The CHORUS experiment will achieve its goal and cover the $\sin^2(2\theta)$ sensitivity down to 2 10^{-4} using the remaining data to be analysed. Along with improvements in the CCD clustering code going on at the moment, the improvement in momentum reconstruction for the 1997 data due to the addition of 18 honeycomb planes downstream of the magnet, the automatic scanning apparatus itself is being replaced by faster models. More and more labs are getting equipped with scanning devices. This global improvement in scanning speed is such that less and less cuts will be done prior to scanning and more and more elaborate vertex analysis will be used, leading to a sensible increase of efficiency and sensitivity.

References

[VI.1] S. Ricciardi, Chorus Internal Note 97001, 1997.

[VI.2] S. Aoki *et al.*,*Nucl. Instrum. Methods* B **51**, 446 (1990).

[VI.3] P. Migliozzi, Chorus Internal Note 97008, 1997.

[VI.4] G. De Lellis and P. Migliozzi, Chorus Internal Note 97021, 1997.

[VI.5] K. Kodama *et al.*, FNAL P803 proposal, 1993.

[VI.6] F. Cassol, Chorus Internal Note 98002,1998.

[VI.7] Y. Obayashi, Chorus Internal Note 97012, 1997.

[VI.8] G. Brooijmans, PhD Thesis, Université Catholique de Louvain, 1998.

[VI.9] J. Brunner, Chorus Internal Note 97017, 1997.

[VI.10] P. Migliozzi, (CHORUS Coll.)hep-ex/9807024, Talk given at 29th International Conference on High-Energy Physics (ICHEP 98), Vancouver, Canada, 23-29 Jul 1998.

[VI.11] R.D.Cousins and V.L. Highland,*Nucl. Instrum. Methods* A **320**, 331 (1992).

Conclusion

The still unanswered questions : 'do neutrinos have a mass ?', 'do they oscillate ?' have led to the realisation of the CHORUS experiment. After 4 years of data taking in the CERN SPS Wide Band neutrino beam, the scanning and the analysis of the events is still going on.

The high precision fibre tracking system allowed an accurate and fast location of the events in the emulsion target, along with the development of the emulsion scanning techniques.

A program for track finding in the fibre trackers of the hadron spectrometer was designed. The loss of resolution due to the distortion of the signal of the fibres in the image intensifiers, the imperfections in the calibration of the read-out charged coupled devices (CCD's) or in the algorithms used to cluster the CCD signals into track elements, as well as the problens due to the high occupancy of the detector due to particles showering in the magnet have been understood corrected as far as possible.

This program was then used to align the fibre trackers of the hadron spectrometer with respect to the target fibre trackers, using cosmic ray and beam associated muons. Several sources of misalignment and movement of the detector where discovered in this process.

A momentum fitting algorithm was written and tested both on simulated and experimental data. It is currently used in the analysis to select tracks of the negative hadrons, the potential τ^- decay candidates, to be scanned in the emulsion target.

The resolution of the hadron spectrometer achieved by the current momentum reconstruction algorithm contributed to the determination of the efficiency of the CHORUS experiment to detect τ^- decays, particularly in the non-muonic modes and to reject background events.

The detector was upgraded at the end of 1996 to include more tracking planes downstream of the magnet to tackle the multiplicity problem uncovered. New signal analysis methods are currently being designed to improve the clustering on the CCD's.

The CHORUS experiment has not, so far, found any τ^- decay candidates. However, the event scanning is continuing and the prediction and scanning methods are being improved, such that CHORUS will cover its foreseen sensitivity region in the parameter plane, down to oscillation probabilities of 10^{-4} .

Other experiments have recently claimed to have observed neutrino oscillations, such as Super-Kamiokande in a region of Δm^2 around 10^{-3} eV^2, unreachable by CHORUS - if their signal is confirmed to be $\nu_\mu \rightarrow \nu_\tau$ oscillations. Indeed, the fact that they would

observe $\nu_\mu \rightarrow \nu_e$ oscillations is ruled out by the Chooz reactor experiment. The dark matter in the universe, is currently rather believed to be essentially cold, such that neutrinos are not needed to contribute with masses as high as 1 eV^2. These recent results tend to predict that CHORUS will not detect an oscillation signal in the low $\sin^2(2\theta)$, high mass region. However, to be able to test the signal seen by Super-Kamikande, long baseline experiments such as OPERA are being designed. This new experiment could run by 2005 in a new CERN neutrino beam pointing towards the underground Gran Sasso laboratory 730 km further. It will take advantage of the high sensitivity emulsion techniques and the experience gained in ν_τ search in CHORUS.

List of Tables

List of Figures

Errata

- p. 23: Particles remain in equilibrium with the radiation as long as the temperature of the radiation is high enough for its energy kT to be as large as their mass.
  Should read:
  Particles remain in equilibrium with the radiation as long as their creation and annihilation rates are larger than the expansion rate of the universe.
- p. 24: $92h^2$ should read $92h_0^2$
- p. 71: In the proposal, th optimistic of...
  should read:
  The optimistic value of ...
- p. 79: The road in DT3 is 3.5 rather than 3.8 cm.
- p. 111: In table 6.12 the number of 1-μ sample scanned up to now in 1996 is 72615 and not 129669.